

Subject-specific computational fluid dynamics modelling and measurement of cerebrospinal fluid motion in the cervical spine

THÈSE N° 6293 (2014)

PRÉSENTÉE LE 15 SEPTEMBRE 2014

À LA FACULTÉ DES SCIENCES ET TECHNIQUES DE L'INGÉNIEUR
LABORATOIRE D'HÉMODYNAMIQUE ET DE TECHNOLOGIE CARDIOVASCULAIRE
PROGRAMME DOCTORAL EN BIOTECHNOLOGIE ET GÉNIE BIOLOGIQUE

ÉCOLE POLYTECHNIQUE FÉDÉRALE DE LAUSANNE

POUR L'OBTENTION DU GRADE DE DOCTEUR ÈS SCIENCES

PAR

Thiresia GIALLOUROU

acceptée sur proposition du jury:

Prof. A. Radenovic, présidente du jury
Prof. N. Stergiopoulos, Dr B. A. Martin, directeurs de thèse
Prof. L. Hirt, rapporteur
Prof. V. Kurtcuoglu, rapporteur
Prof. Y. Ventikos, rapporteur



ÉCOLE POLYTECHNIQUE
FÉDÉRALE DE LAUSANNE

Suisse
2014

Στους γονείς μου,
για την αγάπη τους και την προσφορά τους

Table of Contents

Acknowledgements	8
Abstract	9
Résumé	12
Nomenclature	15
Motivation and objectives	16
Thesis outline	18
1. Introduction	19
1.1 Intracranial space	19
1.1.1 Brain	19
1.1.2 Cerebrospinal fluid circulation	20
1.1.3 Cranial blood flow	22
1.2 Continuous positive airway pressure	23
1.3 Chiari I malformation	24
1.4 Non invasive measurement of the craniospinal dynamics	25
1.4.1 Magnetic resonance imaging	25
1.4.2 Duplex Doppler Ultrasound measurements	27
1.5 Computational fluid dynamics simulations of the CSF flow movement	27
2. Comparison of 4D phase-contrast MRI flow measurements to computational fluid dynamics simulations of cerebrospinal fluid motion in the cervical spine	31
2.1 Abstract	32
2.2 Introduction	33
2.3 Materials and Methods	35
2.3.1 In vivo 4D PC MR measurements	35
2.3.2 CFD simulation	36
2.3.3 Data processing and analysis	38
2.4 Results	39
2.4.1 Peak velocities	39
2.4.2 Velocity profiles	40
2.4.3 Motion of cerebellar tonsils	41
2.4.4 Independence studies	43
2.5 Discussion	43
3. Inter-Operator Dependence of Magnetic Resonance Image-Based Computational Fluid Dynamics Prediction of Cerebrospinal Fluid Motion in the Cervical Spine	49
3.1 Abstract	50
3.2 Introduction	51
3.3 Materials and Methods	52
3.3.1 4D PC MRI data acquisition	52
3.3.2 Three-dimensional reconstruction and mesh generation	52
3.3.2 CFD simulations	53
3.3.3 Data processing	54
3.3.4 Statistical analysis	55

3.4 Results	55
3.4.1 Geometric parameters	55
3.4.2 Hydrodynamics parameters	57
3.5 Discussion.....	59
4. The effect of continuous positive airway pressure on total cerebral blood flow in healthy awake volunteers.....	64
4.1 Abstract	65
4.2 Introduction	66
4.3 Materials and Methods.....	66
4.3.1 Ultrasound measurements	66
4.3.2 CBF calculations.....	67
4.3.3 Statistical analysis	69
4.4 Results	69
4.5 Discussion.....	71
5. Continuous positive airway pressure alters cranial blood flow and cerebrospinal fluid dynamics at the craniovertebral junction.....	76
5.1 Abstract	77
5.2 Introduction	78
5.3 Materials and Methods.....	79
5.3.1 In vivo 2D PC MR measurements	79
5.3.2 Physiological monitoring.....	80
5.3.3 Data processing and analysis	80
5.3.4 Statistical analysis	81
5.4 Results	82
5.4.1 Physiological metrics.....	82
5.4.2 MR-based area and flow metrics	83
5.4.3 Waveform characteristics	84
5.5 Discussion.....	86
6. Conclusions.....	90
6.1 Main findings.....	90
6.2 Future perspectives.....	91
References.....	95
Curriculum Vitae.....	106

Acknowledgements

This work contributed to the project "Development of a coupled hydrodynamic model of the cardiovascular and cerebrospinal fluid system" that was funded by the Swiss National Science Foundation 205321_132695 / 1.

I would like with this opportunity to profoundly thank all people that helped, encouraged, supported, shared, and in several ways made the completion of this thesis possible.

Foremost, I would like to express my sincere gratitude to my thesis director, Professor Nikos Stergiopoulos who gave me the opportunity to undertake the amazing pathway of a doctoral thesis at his laboratory and he offered me the necessary support to accomplish it in a successful way. His valuable insights and encouragement have had an indisputable impact on completing my doctoral studies.

Furthermore, I would like to deeply thank my thesis co-director, Dr. Bryn A. Martin of the University of Akron and director of the Conquer Chiari Research Center who has wisely and patiently guided me through the complex field of the cerebrospinal fluid with the numerous fruitful discussions and meetings. His inexhaustible enthusiasm was a constant source of motivation and inspiration for me and contributed in an invaluable way to the accomplishment of my thesis.

I would also like to thank Professor Vartan Kurtcuoglu of the University of Zurich for his valuable help and feedback for various projects and for being my thesis internal examiner. I am also very grateful to Professor Yiannis Ventikos of the University College London and Professor Lorenz Hirt of the University hospital of Lausanne who were both the external examiners of my thesis. Special thanks go to Professor Lorenz Hirt and Dr. Céline Odier for the great collaboration we had and useful discussions concerning cerebral blood flow dynamics.

Dr. Raphael Heinzer and Dr. José Haba-Rubio from the Research centre for investigation of sleep disorders at the University hospital of Lausanne deserve my thanks for my knowledge around sleep disorders. I would also like to thank Dr. Alexander Bunck and Dr. Jan-Robert Kroeger from the University hospital of Cologne for the very nice collaboration we had and intensive discussions concerning craniospinal disorders and new *in vivo* MR non measurements. Great thanks go to Dr. Eleonora Fornari from the Center of Biomedical Imaging, Nicolas Chevrey from the University hospital of Lausanne, Dr. Francesco Santino from the University of Basel and Dr. Marianne Schmid Daners from the ETH Zurich for their precious discussions related to MRI. Special thanks should go to Professor Frank Loth from the University of Akron for the very useful discussions and Dr. Daniel Sheffer from the same university for his assistance related to statistical analysis. My thanks should also extend to the doctoral students of the Conquer Chiari Research Center from the University of Akron, Nick Shaffer and Soroush Heidari Pahlavian for the collaboration, exchange of ideas and problem solving spirit.

I would like from this position to thank all the former and new members of the LHTC laboratory for maintaining a very friendly working environment. Special thanks should go to Dr. Dimitrios Kontaxakis for his contribution to my knowledge around computational fluid dynamics. Many thanks should go to Fabiana Fraga and her husband Dr. Rodrigo Araujo Fraga da Silva whose friendship and support made easier the returning to the lab in the dark days. I should also mention my students I supervised during my doctoral studies: Isabelle Pitteloud, Farine Emilie, Chiki Anass, Benedict Danny, Leonie Asboth, Christian Meuli, and Serge Metrailler whose work and dedication made my personal work better.

Last but not least, I would like to express my sincere gratitude to my parents, my sister and my brother with all my heart for their incessant support and for the strength they gave me to succeed in life. Endless thanks to all my friends with whom I shared really special moments along these years. Their dedication to distract me from work and to keep my spirit and soul happy was a job that they accomplished in a remarkable way. Finally, I would like to thank Costas for his love and for the fact that he has always supported me with greatest patience, critical remarks and excellent ideas during the years of my doctoral studies and who made my days prettier.

Abstract

The intracranial space is comprised of the brain, blood and cerebrospinal fluid (CSF), all of which co-exist and preserve a constant volume. CSF is formed and secreted primarily by the choroid plexus of the lateral ventricles. It then moves within the rest of ventricular spaces of the cranial cavity and in the spinal subarachnoid space (SSS) to be absorbed at the end by the venous circulation mainly through the arachnoid granulations at the superior sagittal sinus. The role of CSF is essential as it protects the brain from injury and delivers nutrients to and from the brain along with the removal of waste products.

The fluid dynamics of the CSF fluctuation are complex as it moves inside the craniospinal cavities in a pulsatile manner that principally results from the systolic expansion and contraction of cerebral blood vessels. More precisely, systolic arterial expansion causes a pulsatile enlargement of the brain, resulting in a piston-like action that compresses the ventricular spaces and propels CSF into the SSS of the spinal canal. Thus, the SSS allows for pulsatile decompression of the cranium with each systolic expansion. On the contrary, during diastole decreased arterial blood volume causes a reduction in overall brain volume. At that time, the posterior part of the brain that connects it with the spinal cord (SC), the brainstem, retreats cephalad and as a result CSF flow reverses.

Abnormalities in the intracranial equilibrium and CSF dynamics are associated with the pathogenesis of various craniospinal disorders such as hydrocephalus, Chiari I malformation (CMI) and syringomyelia. Detailed measurement and characterization of CSF dynamics is an important factor to help diagnose and assess disease states for patients with those disorders. However, current simple anatomical and two-dimensional phase-contrast MRI (2D PC MRI) measurements of CSF dynamics have limited ability to quantify complex CSF flow patterns that maybe related to these disorders. Recent advances in MRI technology have enabled time-resolved three-directional velocity encoded phase contrast MRI (4D PC MRI) measurements of the CSF flow field that can be regarded as the method that offers the best and most comprehensive insight into CSF hydrodynamics.

Apart from the systolic pulse wave, there is evidence that the respiratory rhythm also plays a significant role in the impetus of the CSF fluctuation. In particular, the respiratory cycle drives a low frequency oscillation of the brainstem, in which caudal brain displacement corresponds to expiration and cephalad rebound corresponds to inspiration. This respiratory phase pulse, superimposed upon the higher frequency cardiovascular pulse, appears to influence CSF pulsations. Modified respiratory efforts affect CSF fluctuation in peculiar ways. For instance, coughing causes a cephalad impulse in CSF flow and Valsalva manoeuvre, the attempt to exhale with the mouth and nose closed, quickly causes caudal and then cephalad brainstem movement. Continuous positive airway pressure (CPAP), the main treatment of obstructive sleep apnea syndrome (OSAS), has been shown to alter the cerebral and CSF dynamics in multiple ways as well. These changes are explained due to the fact that the rise of the intrathoracic pressure that CPAP induces increases the jugular venous pressure. This in turn could have an effect on cerebral blood flow (CBF) by reducing the cerebral perfusion pressure, the net pressure gradient causing CBF to the brain. Concomitantly, changes in the CBF volume due to the increased intrathoracic pressure may hinder cerebral venous drainage via the jugular veins (JV). In addition, CPAP breathing has been found to increase lumbar CSF pressure and reduce CSF peak velocity in humans.

The present thesis addresses the need to assess and explain in detail the CSF flow dynamics in health and diseased conditions so as to understand the pathophysiology of the craniospinal disorders and aid if possible in their diagnosis. In order to accomplish that, the first part of the thesis is focused on the computational fluid dynamics (CFD) modelling of the CSF motion in the SSS and its comparison to novel *in vivo* 4D PCMRI CSF flow measurements. The second part of the thesis is focused on the experimental assessment of CSF and CBF dynamics in normal conditions and under the presence of CPAP that was chosen as a method to non-invasively alter the intrathoracic pressure and observe the impact this would have on the intracranial dynamics.

A number of different MRI-based dynamic tools are available for characterizing the CSF system and evaluating the craniospinal disorders, though none of these have yet been translated to standard clinical use. 2D PCMRI has been the mainstay for the *in vivo* analysis of the CSF system. However, the 1D

velocity encoding of 2D PC MRI does not allow evaluating the complexities of the CSF flow patterns that appear in health and diseased conditions such as CMI. Hence, 4D PC MRI can be regarded as the method that offers the best and most comprehensive insight into CSF hydrodynamics. For that reason it is most suitable for a comparison to CFD models.

The aforementioned goal was met by obtaining 4D PC MRI CSF velocity measurements in the cervical spine of three healthy volunteers and four patients with Chiari I malformation. The CFD simulations of the CSF in the SSS considered the geometries to be rigid-walled and did not include small anatomical structures such as nerve roots, denticulate ligaments and arachnoid trabeculae. Comparison was performed for the first time between 4D PC MRI measurements and CFD simulations in terms of peak CSF flow velocities and velocity flow patterns at nine axial locations (from foramen magnum (FM) to C7) along the cervical spine. Results showed that 4D PC MRI peak CSF velocities were consistently greater than the CFD peak velocities and these differences were more pronounced in CMI patients than in healthy subjects.

The differences observed between the 4D PC MRI and CFD simulations could be attributed to various reasons such as the lack of anatomical fine structures within the CFD models, the brain tissue motion and/or the geometric misrepresentation of the true SSS cross-sectional area due to manual segmentation of the MR image by a single operator. Hence, on a second stage, the inter-operator dependence of MRI-based CFD simulations of CSF dynamics in the cervical spine was evaluated for the first time. The 3D anatomy of the cervical SSS of a single healthy volunteer was reconstructed by manual segmentation by seven independent operators and was then simulated by a single operator using 3D CFD with the same methods as the previous study described. Results were compared in terms of several hydrodynamic and geometric parameters at nine axial locations along the spinal canal (from FM to C7). The findings showed a high degree of reliability for using MRI-based CFD simulations to quantify CSF hydrodynamic and geometric-based parameters in the cervical spine of a control. As a whole, the computational modelling of the CSF motion that was performed in the present thesis highlights the utility of 4D PC MRI in conjunction with CFD for detailed analysis of CSF flow dynamics that could help distinguish physiological from complex pathological flow patterns at the cervical SSS.

Regarding the experimental assessment of the CSF and CBF dynamics, first the influence of CPAP on total CBF was investigated in 23 healthy awake subjects. This served as a primary research study that would help us understand the mechanism of the CPAP device and how it acts on the CBF system. Duplex colour Doppler Ultrasound (US) measurements of flow velocity and lumen diameter of the left and right proximal internal carotid arteries (ICA), vertebral arteries (VA), and middle cerebral arteries (MCA) were obtained with and without CPAP at 15 cm H₂O. Transcutaneous carbon dioxide (PtcCO₂) level, heart rate (HR), blood pressure and oxygen saturation (SaO₂) were monitored during the measurements. The results of this study showed that CPAP provoked a decrease of 12.5% at the CBF that was mediated predominately through the hypocapnic vasoconstriction coinciding with PCO₂ level reduction.

The arm of this study was extended on a second stage in order to examine the effect of CPAP at 15 cm H₂O on CSF dynamics, CFD and jugular venous flow on healthy awake volunteers with a use of a specific 2D phase contrast MRI (2D PC MRI) protocol with the same physiological monitoring with the previous research. The results indicated that CPAP decreased the pulse amplitude of CSF and jugular venous flow as well as the stroke volume of CSF. Spectral analysis of the overall flow waveforms showed some significant changes with the presence of CPAP as well. The difference between the first research study that involved examining the effect of CPAP on CBF dynamics with the use of US measurements and research study that used 2D PC MRI to estimate the impact of CPAP on CSF and CBF dynamics is that in the MRI study the alterations observed in the CSF and jugular venous flow were mainly attributed to the direct influence of CPAP usage on the intrathoracic pressure. As a whole, the experimental measurements that are described in the present thesis under normal conditions and with the use of the CPAP device, revealed that CPAP should be used in caution in patients with unstable cerebral hydrodynamics

Overall, the research described in the thesis at hand could be useful for providing better information of the CSF dynamics in health and disease that could be crucial to understand the pathogenesis of craniospinal and disorders.

Key words

Cerebrospinal fluid dynamics, computational fluid dynamics, modelling, subject-specific, cervical spine, Chiari I malformation, *in vivo* measurements, magnetic resonance imaging, ultrasound measurements, cerebral blood flow, continuous positive airway pressure

Résumé

L'espace intracrânien est occupé par le cerveau, le sang et le liquide céphalo-rachidien (LCR), qui interagissent pour maintenir un volume constant. Le LCR est formé et sécrété principalement par les plexus choroïdes des ventricules latéraux. Il se distribue ensuite dans le reste des espaces ventriculaires du cerveau et dans l'espace sous-arachnoïdien (SSS) pour être absorbé à la fin par la circulation veineuse, principalement par les granulations arachnoïdiennes du sinus sagittal supérieur. Le rôle du LCR est très important car il protège le cerveau contre les traumatismes, fournit des nutriments au cerveau et permet l'élimination des produits de déchet.

La dynamique de la fluctuation du LCR est complexe car il se déplace à l'intérieur des cavités craniospinales d'une manière pulsatile, en raison principalement des variations de volume des vaisseaux sanguins cérébraux. Plus précisément, la dilatation artérielle systolique provoque un élargissement pulsatile du cerveau, ce qui entraîne une action analogue à un piston qui comprime les espaces ventriculaires et propulse le LCR dans les SSS du canal rachidien. Ainsi, les SSS permettent une décompression pulsatile avec chaque dilatation systolique. Au contraire, pendant la diastole, la diminution du volume sanguin artériel provoque une réduction du volume global du cerveau. À ce moment, la partie postérieure du cerveau qui est reliée à la moelle épinière (ME) et le tronc cérébral se déplacent, et le flux du LCR s'inverse.

Des anomalies dans l'équilibre et la dynamique du LCR intracrânien sont associés à la pathogenèse de divers troubles craniospinaux tels que l'hydrocéphalie, la malformation de Chiari I (MCI) et la syringomyélie. La mesure détaillée et la caractérisation de la dynamique du LCR deviennent des facteurs importants pour aider à diagnostiquer et évaluer les patients atteints de ces troubles. Cependant, les techniques actuelles bidimensionnelles de phase-contraste en IRM (2D PC MRI) pour la mesure de la dynamique du LCR ont une capacité limitée de quantifier des schémas de flux du LCR complexes. Les progrès récents dans la technologie d'IRM, comme 4D PC MRI permettent une évaluation plus précise de la dynamique du LCR.

En dehors de l'onde de pulsation artérielle, il est prouvé que le rythme respiratoire joue également un rôle important dans l'amplitude des fluctuations du LCR. En particulier, le cycle respiratoire entraîne une oscillation de basse fréquence du tronc cérébral, dans laquelle l'expiration entraîne un déplacement caudal du cerveau et l'inspiration un déplacement rostral. Cette variabilité induite par le cycle respiratoire, superposée à celle plus élevée induite par le pouls cardiovasculaire, influence la pulsatilité du LCR. La modulation des efforts respiratoires affecte la fluctuation du LCR de différentes façons. Par exemple, la toux provoque un déplacement rostral du LCR, et la manœuvre de Valsalva (la tentative d'expirer avec la bouche et le nez fermé) provoque rapidement un mouvement en direction caudale, puis un déplacement rostral du tronc cérébral. La Pression Positive Continue (PPC), le principal traitement du syndrome d'apnées obstructives du sommeil (SAOS), semble aussi pouvoir modifier la dynamique cérébrale et du LCR dans de multiples façons. Ces modifications sont expliquées par le fait que l'augmentation de la pression intrathoracique induite par la PPC augmente la pression au niveau de la veine jugulaire. Cela pourrait à son tour avoir un effet sur le débit sanguin cérébral (DSC) en réduisant la pression de perfusion cérébrale, en raison du gradient induit. Parallèlement, les changements du DSC en raison de la pression intra-thoracique accrue peuvent entraver le drainage veineux du cerveau à travers les veines jugulaires. En plus de cela, il a été démontré que la PPC augmente la pression du LCR à niveau lombaire et qu'elle peut réduire la vitesse de pointe du LCR chez l'homme.

La présente thèse traite de la nécessité d'évaluer en détail la dynamique du flux du LCR et la dynamique de l'espace intracrânien chez des sujets normaux et chez des sujets présentant des pathologies, afin de mieux comprendre la physiopathologie de certains troubles craniospinaux. Pour accomplir cela, la première partie de la thèse est axée sur la modélisation computationnelle et dynamique des fluides (CFD) appliquée au mouvement du LCR dans les SSS, et sa comparaison à de 4D PCMRI de mesure *in vivo* des flux du LCR. La deuxième partie de la thèse est axée sur l'évaluation

expérimentale des dynamiques du LCR et du DSC dans des conditions normales et sous PPC, qui a été choisie comme méthode non invasive pour modifier la pression intra-thoracique et observer l'impact que cela aurait sur la dynamique intracrânienne.

La PC MRI 2D a été la référence pour l'analyse *in vivo* du LCR. En tout cas, PC MRI 2D ne permet pas d'évaluer la complexité du pattern d'écoulement du LCR qui apparaît dans des conditions normales et lors de maladies telle que le MCI. Ainsi, la PC MRI 4D peut être considérée comme la méthode qui offre le meilleur aperçu *in vivo* de l'hydrodynamique du LCR. Pour cette raison, elle est plus appropriée pour une comparaison avec des modèles de DSC.

L'objectif précité a été atteint par l'obtention de mesures PC IRM 4D de vitesse d'écoulement du LCR dans le rachis cervical de volontaires sains et de patients. Une IRM de haute résolution a permis de définir l'anatomie de la colonne cervicale, qui a été par la suite segmentée manuellement pour construire un modèle 3D. Les simulations CFD considèrent la géométrie comme étant à paroi rigide, et ne comprennent pas les petites structures anatomiques telles que les racines nerveuses, les ligaments denticulés et l'*arachnoid trabeculae*. Les données ont été évaluées en termes de vitesse maximale d'écoulement du LCR et de flux, dans neuf emplacements axiaux le long de la colonne cervicale. Les vitesses maximales du LCR obtenues par PC IRM 4D étaient systématiquement plus élevées que les vitesses maximales CFD, et ces différences étaient plus prononcées chez les patients MCI que chez les sujets sains. Cette étude constitue la première comparaison des mesures 4D PC IRM et de simulations CFD de l'écoulement du LCR dans le SSS cervical.

Les auteurs ont postulé l'hypothèse que les différences entre la PC MRI 4D et les simulations CFD peuvent être attribués à diverses raisons telles que : le manque de structures fines anatomiques dans les modèles CFD, le mouvement du tissu cérébral et / ou une inexacte géométrie des SSS en raison de la segmentation manuelle de des images MRI par un seul opérateur. Ainsi, dans une deuxième étape, l'influence de l'opérateur sur les simulations CFD de la dynamique du LCR dans le rachis cervical basées sur la MRI a été évaluée pour la première fois. Une reconstruction anatomie 3D des SSS d'un seul volontaire sain a été effectuée par segmentation manuelle par sept opérateurs indépendants, et a ensuite été simulé par un seul opérateur utilisant CFD 3D, avec les mêmes méthodes que l'étude précédente. Les résultats ont été comparés en fonction de plusieurs paramètres hydrodynamiques et géométriques dans neuf emplacements axiaux le long du canal rachidien. Ces résultats ont montré un degré élevé de fiabilité pour l'utilisation de simulations CFD sur la base de la MRI, pour quantifier les paramètres hydrodynamiques et géométriques du LCR dans le rachis cervical. La modélisation théorique du mouvement du LCR qui a été effectuée en cette thèse met en évidence l'utilité de la CFD en conjonction avec la PC MRI 4D pour une analyse détaillée de la dynamique des flux de CSF, qui pourrait aider à distinguer les flux physiologiques des flux pathologiques au niveau des SSS du rachis cervical.

En ce qui concerne l'évaluation expérimentale de la dynamique du DSC et du LCR, l'influence de la PPC sur le DSC total chez 23 sujets sains éveillés a été examinée. Des mesures par écho-Doppler duplex couleur de la vitesse du flux et du diamètre des artères carotides internes (ACI) droite et gauche, des artères vertébrales (AV), et les artères cérébrales moyennes (ACM) ont été obtenues, avec et sans PPC (à un niveau de pression de 15 cm H₂O). Des mesures du dioxyde de carbone transcutanée (PtcCO₂), de la fréquence cardiaque (FC), de la pression artérielle et de la saturation en oxygène (SaO₂) ont été effectuées en continu pendant les enregistrements. Les résultats de cette étude ont montré que la PPC induit une baisse de 12,5% du DSC, qui a été provoqué principalement par la vasoconstriction induite par la réduction du niveau de PCO₂.

L'extension de cette étude a permis d'examiner l'effet de la PPC à 15 cm H₂O sur le DSC ainsi que sur la dynamique du LCR chez des volontaires éveillés en bonne santé, en utilisant un protocole spécifique de MRI 2D (PC IRM 2D). A nouveau, la FC, la PtcCO₂ transcutanée et la SaO₂ ont été monitorées en continu. Les résultats indiquent que la PPC diminue l'amplitude de l'onde de pouls et le

volume systolique du LCR. En plus de cela, la pulsation au niveau de VJ a diminué, tandis qu'il n'y avait pas de modifications significatives au niveau du DSC artériel. L'analyse spectrale des signaux globaux de flux a montré des changements importants avec PPC. La différence entre la première étude avec les mesures avec écho-doppler et cette étude est que dans l'étude MRI avec PPC les modifications ont été principalement attribuées à l'influence directe de la PPC via l'augmentation de la pression intrathoracique. Les deux études ont révélé que la PPC doit être utilisée avec prudence chez les patients instables d'un point de vue de l'hydrodynamique cérébrale, mais certainement des nouveaux travaux sont nécessaires pour établir avec précision l'impact de la PPC sur la dynamique intracrânienne.

Dans l'ensemble, la recherche décrite dans cette thèse pourrait être utile pour une meilleure connaissance de la dynamique de l'ensemble qui pourraient être cruciales pour comprendre la pathogenèse de troubles craniospinaux et cérébro-vasculaires.

Mots clés

Dynamique du liquide céphalo-rachidien, Modélisation computationnelle et dynamique des fluides, modélisation, sujet spécifique, rachis cervicale, malformation de Chiari I, mesures in vivo, imagerie par résonance magnétique, mesures échographiques, débit sanguin cérébral, pression positive continue

Nomenclature

2D PC MRI	Two dimensional phase-contrast MRI
4D PC MRI	Three dimensional velocity encoded phase contrast MRI
BMI	Body mass index
BP	Blood pressure
C1	First cervical vertebrae
C2M	Middle of the second cervical vertebrae
C2P	Posterior of the second cervical vertebrae
C3	Third cervical vertebrae
C4	Fourth cervical vertebrae
C5	Fifth cervical vertebrae
C6	Sixth cervical vertebrae
C7	Seventh cervical vertebrae
CBF	Cerebral blood flow
CC	Craniospinal compliance
CFD	Computational fluid dynamics
Chiari I Malformation	CMI
CNS	Central nervous system
CPAP	Continuous positive airway pressure
CSF	Cerebrospinal fluid system
FM	Foramen magnum
FSI	Fluid structure interaction
HR	Heart rate
ICA	Internal carotid artery
ICP	Intracranial pressure
JV	Jugular vein
MCA	Middle cerebral artery
MRI	Magnetic resonance imaging
N.S	Statistically non-significant
OSAS	Obstructive sleep apnea syndrome
p	p-value
PCO ₂	Partial pressure of carbon dioxide
PtcCO ₂	Transcutaneous pressure of carbon dioxide
PtPPA	Peak to peak pulse amplitude
ROI	Region of interest
S	Statistically significant
SaO ₂	Oxygen saturation
SC	Spinal cord
SD	Standard deviation
SSS	Spinal subarachnoid space
SV	Stroke volume
tCBF	Total cerebral blood flow
TCD	Transcranial Doppler Ultrasound
TE	Echo time
tJVF	Total jugular venous flow
TR	Repetition time
US	Ultrasound
VA	Vertebral artery
VENC	Encoded velocity

Motivation and objectives

Alterations in the intracranial equilibrium and CSF flow patterns in the craniovertebral junction have been suspect to play a crucial role in the pathogenesis and diagnosis of craniospinal disorders such as hydrocephalus, CMI and syringomyelia that affect on an average 1 in 4000 births¹⁻⁶. Despite the fact that these disorders have been explained almost 100 years ago, their pathophysiology still remains unclear. In patients with these disorders, analysis of morphology alone has proved to be insufficient in explaining the absence or presence of symptoms⁷. Thus, researchers have been investigating the connection between CSF dynamics and disease states in terms of the detection of objective geometric and flow parameters such as CSF velocities⁸ and bi-directional flow jets^{9, 10}. The integration of medical imaging and subject-specific CFD modeling is a dynamic tool to gain detailed insight into the CSF dynamics in health and disease¹¹. However, to this day, because of the practical difficulties associated with the *in vivo* measurement of CSF quantities, the complete physiological understanding of the CSF dynamics and its importance related to the craniospinal disorders still remains enigmatic.

Significant work has been done to measure non-invasively CSF and brain tissue motion within the spine and cranium using MRI¹²⁻¹⁵. 2D PC MRI is the cornerstone for the *in vivo* analysis of CSF dynamics in healthy and pathologic conditions, such as CMI. As a single slice technique, 2D PC MR imaging is limited by its restricted spatial coverage. Thus, it does not reflect the temporal and spatial heterogeneity of CSF dynamics that are found to be associated with lesions¹⁶. Conversely, 4D PC MRI flow imaging has been increasingly appreciated for its potential in providing a comprehensive comprehension of complex flow phenomena that may occur in the CSF space^{17, 18}. 4D PC MRI could allow for improvements in the clinical diagnosis of CMI and syringomyelia by identifying CSF flow abnormalities present in CMI patients who are likely to benefit from decompressive surgery^{19, 20}.

Until recently, various studies in the literature have used CFD simulations mainly based on 2D PC MRI flow measurements and anatomical data in order to represent the 3D flow and pressure field within the CSF²¹⁻²³. An extended review of literature on the CFD modelling of the CSF movement in the SSS is provided in Chapter 2 of the present thesis. The advantage of CFD is that it provides a global understanding of CSF dynamics and the importance of individual anatomical aspects of the CSF system that should be incorporated in the CFD modeling such as the spinal cord nerve roots, trabeculae or tonsillar descent that occurs in CMI. However, the CFD-based prediction of CSF flow lacks validation and its clinical application is still limited. This is because at best, CFD predictions in most of the studies are based on *in vivo* 2D PC MRI measurements for the boundary conditions. With the aforementioned modern improvement of high resolution 4D PC MRI, the convergence of medical imaging and powerful desktop workstations would make it possible to validate and reliably simulate the pulsatile CSF flow in anatomically realistic geometries of the cervical spine. The contribution of 4D PC MRI technique lies on the fact that it could optimize the boundary conditions used in CFD simulations of the CSF flow region. Thus, the objectives of Chapter 2 were 1) to use 4D PC MRI to measure the CSF flow field in the upper cervical spine in healthy volunteers and Chiari patients of different ages and 2) compare for the first time the results with subject-specific CFD simulations based on the same boundary conditions. As part of eliminating the limitations of Chapter 2, we further examined in Chapter 3 the inter-operator dependence of MRI-based CFD simulations of the CSF motion in the cervical spine of a control. As a result, one of the healthy geometries used in Chapter 2 was segmented by seven independent operators in Chapter 3 so as to compare the results in terms of several geometric and hydrodynamic CSF parameters. The objectives of Chapter 3 were 1) to assess for the first time the reliability of the MRI-based CFD methodology to quantify the CSF hydrodynamic environment and 2) identify the parameters that would help provide a link to disease states.

Chapters 4 and 5 of the present thesis aimed at 1) obtaining baseline measurements of the CSF and cranial blood flow in healthy individuals and 2) measuring the CSF and CBF system with the presence of CPAP, the most widely accepted treatment for obstructive sleep apnea. These research studies would help to improve understanding of the influence of CPAP on both the CBF and CSF dynamics. The motivation behind these studies was driven by the fact that there is little information in the literature

about how acute alterations in chest pressure can alter intracranial dynamics. Patients with CMI have reported symptoms associated with coughing and sneezing and have occurrence of sleep apneas^{24, 25}. While CPAP usage has become routine, the full physiological impact of its use on cranial blood flow and CSF dynamics is not yet fully understood. Studies have shown that CPAP affects cerebral hemodynamics in multiple ways²⁶⁻²⁸. Considering that a rise of the intrathoracic pressure increases the jugular venous pressure, CPAP could have an effect on CBF by reducing the cerebral perfusion pressure and blocking the cerebral venous drainage via the jugular veins^{29 30}. There is evidence in the literature that CPAP breathing increases lumbar CSF pressure³¹ and reduces CSF peak velocity in the aqueduct of Sylvius³². Hence, we chose the device of CPAP as a method to non-invasively alter intrathoracic pressure and investigate the response of both the CBF and CSF systems to its mechanism. A detailed understanding of how CPAP affects the intracranial hydrodynamics could help potentially provide new treatment possibilities for patients with CMI and sleep apnea.

To this end, Chapter 4 aimed at developing a non-invasive bedside protocol using duplex color Doppler ultrasound to evaluate total CBF in 23 healthy awake subjects under normal conditions and with CPAP. This method included the measurement of flow velocity and lumen diameter obtained at the left and right ICA, VA, and MCA. This research study acted as a basis that would help us understand the physiological mechanism of CPAP and its impact on the CBF system. On a later stage, in Chapter 5, the objective was to investigate the influence of CPAP on the arterial, venous and CSF flow dynamics in the upper cervical spine of 23 healthy male awake volunteers with the use of 2D PC MRI protocol. Thus, we simultaneously measured the flow in the left and right ICA, VA, JV and the CSF flow at the C2-C3 level of the cervical spinal canal with and without CPAP applied.

Altogether, the thesis at hand has both a computational and an experimental aspect:

- We simulated the subject-specific CSF flow field in the cervical spine using 3D rigid-wall CFD modelling.
- We assessed for the first time the inter-operator dependence of MRI-based CFD modelling of CSF motion in the cervical-medullary junction
- We experimentally assessed the CSF flow in the upper cervical spine of controls and CMI patients with the use of 2D PC MRI and 4D PC MRI
- We compared for the first time 4D PC MRI measurements to CFD simulations based on the same boundary conditions
- We measured the cranial blood flow in healthy volunteers with the use of US measurements and 2D PC MRI
- We used CPAP as a way to alter intrathoracic pressure and examined the effect on both CBF and the CSF system by developing specific non-invasive flow measurement protocols.

The outcomes of the present thesis could support together with other ongoing projects in the literature, the attempt of building new diagnostic/detection tools for CSF dynamics related to craniospinal disorders. The CSF dynamics can be altered by the craniospinal diseases and, in turn, CSF dynamics can be analyzed to aid in the diagnosis of these. Thus, the studies described in the present thesis provide detailed information about the CSF flow environment in health and patients with CMI that together with novel medical imaging modalities, such as 4D PC MRI bring the medical doctors and engineers closer to clinical usage of this important information.

Thesis outline

The organization of the present thesis is the following:

- Chapter 1 is the introductory chapter
- Chapters 2 and 3 refer to the computational modeling of the cerebrospinal fluid motion in the cervical spine. In particular Chapters 2 and 3 are based on the manuscript of the following scientific publications, respectively*:

Yiallourou (Giallourou) TI, Kröger JR, Stergiopoulos N. et al. (2012) Comparison of 4D Phase-Contrast MRI Flow Measurements to Computational Fluid Dynamics Simulations of Cerebrospinal Fluid Motion in the Cervical Spine. PLoS ONE 7: e52284.

Yiallourou (Giallourou) TI, Shaffer et al. Inter-operator dependence of subject-specific CFD modeling of cerebrospinal fluid dynamics at the craniocervical junction (under review)

- Chapters 4 and 5 refer to experimental assessment of the cerebrospinal fluid system and cranial blood flow in normal conditions and under the presence of CPAP. In particular Chapter 4 and 5 are based on the following scientific publications*:

Yiallourou (Giallourou) TI, Odier C, Heinzer R, et al. The effect of continuous positive airway pressure on total cerebral blood flow in healthy awake volunteers, Sleep Breath. 2012, 1-8

Yiallourou (Giallourou) TI, Schmid Daners M, Kurtcuoglu V. et al. (2014) Continuous positive airway pressure alters cerebral blood flow and cerebrospinal fluid dynamics at the craniovertebral junction (under review)

- Chapter 6 summarizes the main findings of the dissertation and provides an outlook for future perspectives

Other publications produced during this thesis project include:

1. Pahlavian SH, **Yiallourou (Giallourou) TI** et al. et al., "The impact of spinal cord nerve roots and denticulate ligaments on cerebrospinal fluid dynamics in the cervical spine," PLoS One, vol. 9, p. e91888, 2014.
2. Pahlavian SH, Bunck AC, **Yiallourou (Giallourou) TI** et al. Hydrodynamic characterization of cervical cerebrospinal fluid motion by 4D phase-contrast MRI and comparison to anatomically detailed 3D computational fluid dynamics simulation (under review in American Journal of Neuroradiology).
3. R. Heinzer, NJ. Petitpierre, **Yiallourou (Giallourou) TI** et al., Oscillating positive airway pressure (O-PAP) compared to CPAP in obstructive sleep apnea patients: a pilot study (under review in Sleep journal).

*All corresponding co-authors gave their kind permission for the manuscripts' reprint.

Permission was granted to reproduce the figures used in the present thesis when necessary from the scientific journals

1. Introduction

1.1 Intracranial space

Understanding of the normal pathophysiology of intracranial space and intracranial pressure (ICP) is essential to effectively manage patients with craniospinal disorders such as Chiari I malformation, syringomyelia and hydrocephalus. The basis for our understanding of changes in ICP is the Monro- Kellie doctrine³³ that explains how expansion of the brain drives the CSF circulation. According to the Monro-Kellie hypothesis, the cranial cavity is a rigid sphere filled with the following non compressible contents: the brain tissue, the arterial and venous blood volume and CSF, each of which has a distribution shown in Figure 1.1.

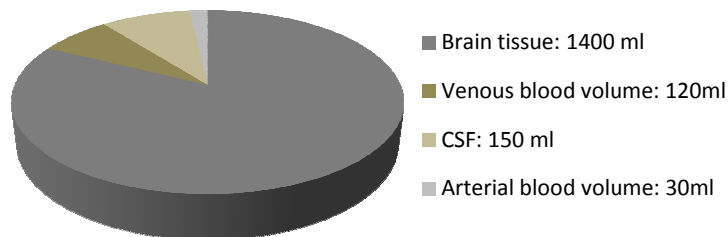


Figure 1.1 The relative volumes of intracranial contents ³⁴

These three components of the cranium must co-exist in a state of dynamic equilibrium, wherein a change in the volume in one component requires a change in volume in either one or both of the other two. Otherwise, an increase in the total volume of the cranial constituents will result in alterations in ICP beyond the normal values, which for a healthy adult in the supine position are in the range of 7-15mmHg³⁵. Evidently, analysis of the intracranial neurohydrodynamics is ultimately associated with the comprehension of its anatomical compartments.

1.1.1 Brain

The brain, an ~1400 ml soft mass of nervous tissue (Figure 1.2)., is contained in the cavity of the skull and together with the spinal cord (SC) comprises the central nervous system (CNS). It can be considered as the most critical organ to protect from trauma and acts on the rest of the body both by generating patterns of muscle activity and by driving the secretion of hormones.



Figure 1.2 T1- weighted MRI image of the human brain.

The brain is surrounded by the meninges, membranes that protect it and together with the SC isolate it from the surrounding bones. The meninges consist of the dura, pia and arachnoid matter (Figure 1.3) and their role is to protect the CNS with the help of the CSF circulation. The dura mater is the outermost layer which covers the inside surface of the skull and spinal vertebrae. The inner surface of the dura is covered by the arachnoid mater. The innermost layer covering the brain and SC is the pia mater. In the 2 to 9 mm of space separating the pia and arachnoid mater is the spinal subarachnoid space (SSS) filled with CSF and transversed by a network comprised of the arachnoid trabeculae, with an approximate diameter of $15\ \mu\text{m}$ ³⁶, many vessels, ligaments and nerves.

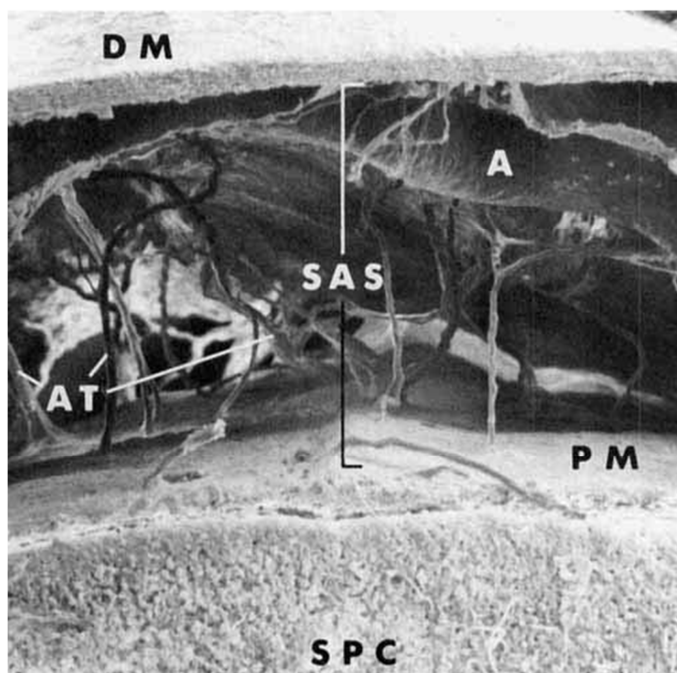


Figure 1.3 Illustration of spinal meninges and subarachnoid space with the use of electron microscopy. A view of the cut end of the spinal cord (SPC) shows the pia mater (PM) lying directly upon the surface of the cord. Arachnoid trabeculae (AT), continuous with the pia, extend to the arachnoid mater (AM) and to an artery (A) above. The separation of the arachnoid mater from the thick dura mater (DM) is an artifact of preparation. The subarachnoid space (SAS) separates the arachnoid from the pia³⁷

1.1.2 Cerebrospinal fluid circulation

The craniospinal subarachnoid space and the ventricles of the brain are filled with CSF, a colorless fluid, that provides nutrients to the brain and cushions it from mechanical shock¹³. CSF is produced with an average rate of 0.3 to 0.7 mL/min by the epithelial cells of the choroid plexuses. It flows from the lateral ventricles into the third ventricle, and from there through the aqueduct of Sylvius into the fourth ventricle (Figure. 1.4). Then most of it passes it through the median foramen of Magendie and the two lateral apertures of Luschka into the SSS. CSF in the SSS communicates with the cisterns at the base of the brain and spreads through the arachnoid trabeculae, diffusing superiorly around the brain and inferiorly around the SC.

The absorption of CSF is provided by the arachnoid granulations at the superior sagittal sinus into the venous circulation (Figure. 1.4 and 1.5). In the adult, about 130 ml of CSF constantly circulates and surrounds the brain on all sides. The volumetric distribution of CSF varies according to the region it circulates through. The majority of the fluid occupies the cranial subarachnoid space (100ml). The lateral ventricular horns where most of the production takes place contains 25-30 ml of CSF while within the third and fourth ventricle 2-3ml of CSF circulate. Finally, approximately 25 ml of CSF circulate within the

SSS³⁸. In order to maintain a constant volume, the CSF is replaced about three to four times each day (500 ml/day).

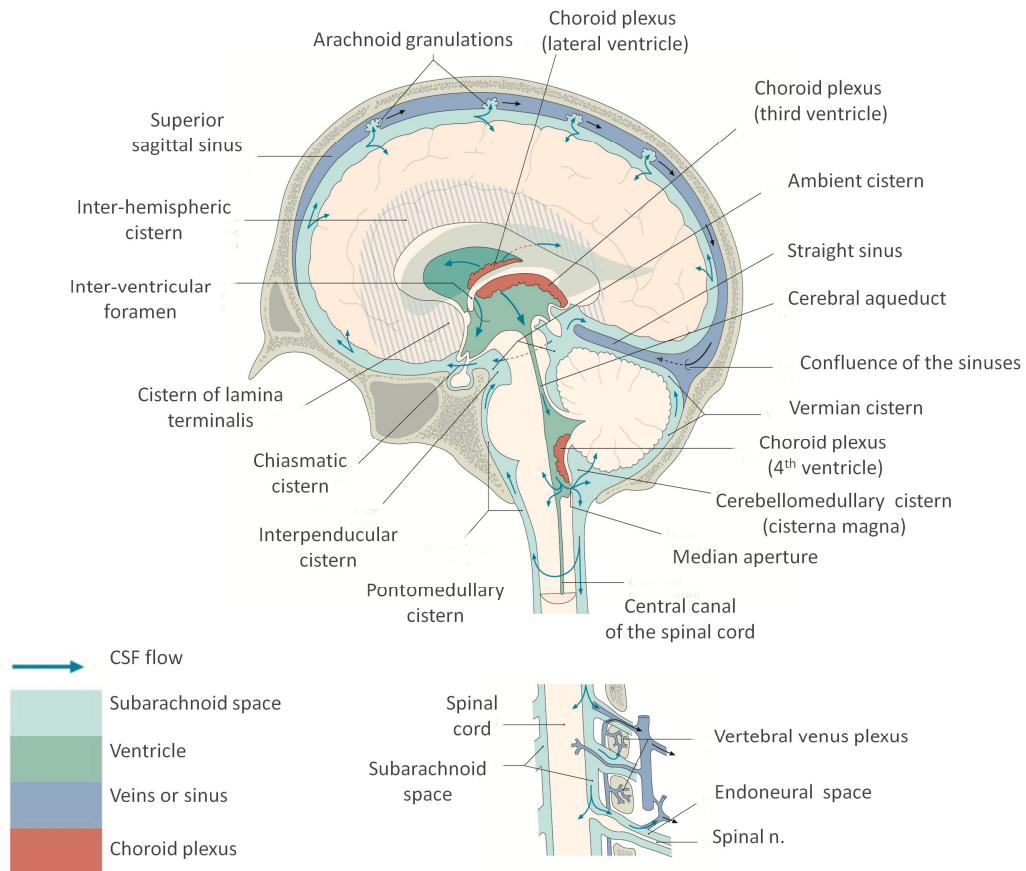


Figure 1.4 Cerebrospinal fluid circulation³⁹ (Reprinted by permission of Pearson Education, Inc.)

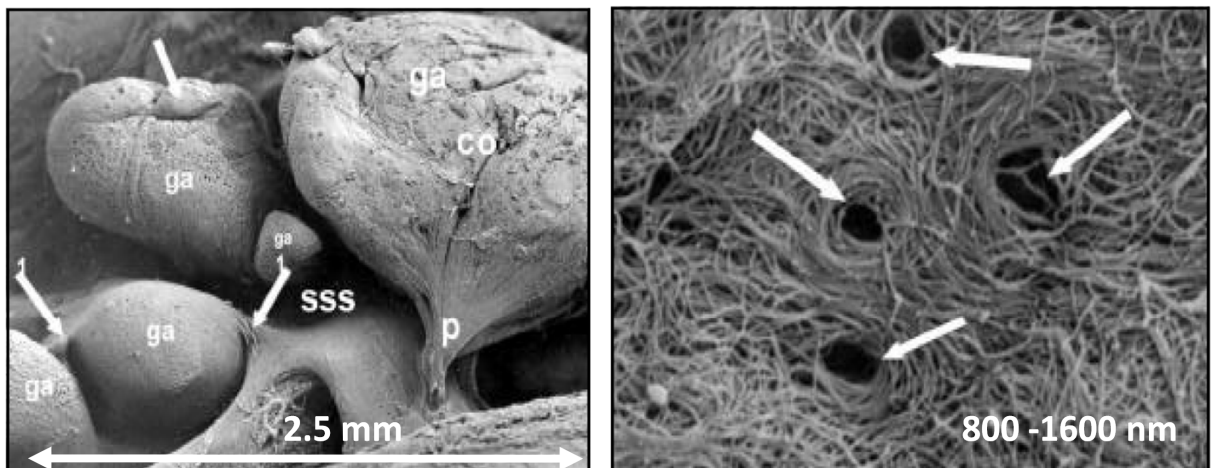


Figure 1.5 Left: Scanning electron microscopy of the superior sagittal sinus where arachnoid granulations (**ga**) are present (left). Observe the presence of a lobule (arrow), junction of the dura matter with the granulation capsule (arrows 1) and the regions of pedicle (p) and the body (co) on the larger granulation. Right: Scanning electron microscopy of the outer surface of the arachnoid granulation at the apical region indicating bundles of collagen fibers with circular orientation lining the smaller pores (arrows)⁴⁰

Next to a net flow caused by production and absorption, the expansion and contraction of cerebral arteries during the cardiac cycle as well as changes in venous pressure with the respiratory cycle drive CSF

flow in a pulsatile manner. In particular, CSF flows in the craniospinal cavities in a pulsatile manner that has mainly been associated with changes in blood volume within the cranial vault during the cardiac cycle. The systolic expansion and contraction of cerebral blood vessels compress the lateral ventricles in systole causing CSF to expel through the SSS and around the SC^{41, 42}. CSF pulsates caudocranially during systole and craniocaudally during diastole so that each cardiac cycle has equal amounts of CSF fluid movement with almost zero net flow⁴³. However, there are indications that there could be a secondary driving mechanism for CSF pulsation. For instance, Dunbar et al.⁴⁴ found the lumbar CSF pressure pulsations to persist in dogs even with the cervical canal blocked. In the present thesis, both subject-specific computational modelling and experimental assessment of the CSF system have been accomplished. In Chapter 2, *in vivo* 4D PC MRI measurements of the CSF motion were obtained at craniovertebral junction and compared for the first time to subject-specific 3D computational fluid dynamics simulations in healthy volunteers and patients with craniospinal disorders. In addition to this, in Chapter 3, the inter-operator geometric dependence of computational fluid dynamics modelling of the CSF movement at the cervical spine was investigated. In Chapter 4, *in vivo* 2D PC MRI measurements of the CSF at the cervical spine were acquired in healthy volunteers with and without the application of the CPAP in order to estimate the response of the system to CPAP.

1.1.3 Cranial blood flow

Normal function of the brain is dependent upon adequate supply of oxygen and nutrients through a complex and dense network of blood vessels. A physiologic CBF value for a healthy adult is about 20% of the cardiac output, which is 800ml/min. The brain is able to maintain a constant CBF between a normal range of mean arterial blood pressure (BP) (80-120mmHg). Blood is supplied to the brain, face, and scalp via two major sets of vessels: the right and left common carotid arteries (that separate to external and internal carotid arteries (ICAs)) and the right and left vertebral arteries (VAs) (Figure 1.6). These arteries converge into the Circle of Willis. Absorption of the CSF is taking place at the superior sagittal sinus.

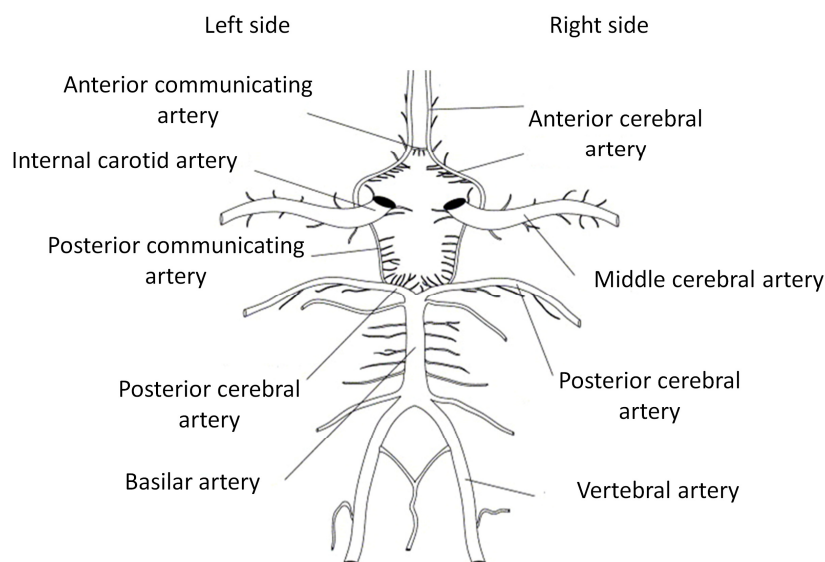


Figure 1.6 Schematic representation of the circle of Willis and main arteries supplying blood to the brain⁴⁵

The CSF circulation is directly linked and coupled to that of the cardiovascular, venous and respiratory system. The heart not only drives blood flow, but is also at the origin of CSF pulsations through the expansion and contraction of cerebral blood vessels, as it was detailed in the preceding section⁴⁶. Phase difference in the cerebral blood in and outflow results in pulsatile movement of CSF throughout the cranial and SSS. The pulsatile movement of CSF is reflected by ICP oscillations with peak-to-peak

amplitude ranging from 0.5 to 3 mm Hg. The relation of CSF, cerebral arterial and cerebral venous flow and pressure pulsations has been investigated⁴⁷⁻⁵³. Overall, these studies indicate that the SSS CSF flow pulsation at the upper cervical spine is approximately the sum of the total cerebral blood inflow (positive) and outflow (negative), with a small difference in magnitude and phase due to intracranial compliance. In the present thesis, we experimentally quantified the cranial blood flow so as to further understand its coupling with the CSF system. In particular, Chapter 4 is focused on the use of duplex color Doppler Ultrasound assessment of the CBF in healthy volunteers in baseline and under the presence of CPAP. In Chapter 5, we extended the arm of Chapter 4 and aimed at estimating the impact of CPAP on the arterial, venous as well the CSF system on healthy awake volunteers with the use of 2D PC MRI measurements.

1.2 Continuous positive airway pressure

The mechanism of continuous positive airway pressure (CPAP) (Figure 1.7) was used in Chapters 4 and 5 of the present thesis as a method to non-invasively alter intrathoracic pressure in order to study the effect of acute pressure changes in the chest on intracranial dynamics.

CPAP has been the main treatment of obstructive sleep apnea syndrome, preventing the collapse of the pharyngeal airway by increasing intrathoracic pressure²⁷. The reason we chose to use the device of CPAP is because it increases the intrathoracic pressure and the pressure transmission pathways between intrathoracic and ICP through the venous system have been examined by various researchers in the literature^{30, 54-56}. Considering that a rise in intrathoracic pressure increases jugular venous pressure, CPAP could have an effect on CBF by reducing the cerebral perfusion pressure^{29, 57}. Moreover, decreased venous return due to increased intrathoracic pressure may decrease right (and left) filling pressure, which may in turn decrease cardiac output. However, published data about the influence of CPAP upon cerebral and CSF dynamics are conflicting which may be due to inaccurate and/or insensitive CBF measurement methods^{26, 27, 32, 58}. As a result, in Chapter 4 we aimed to accurately quantify total CBF on healthy awake volunteers under the presence of CPAP using ultrasound measurements by integrating the arterial lumen diameter and flow velocity of the main vessels supplying blood to the brain, such as ICAs, VAs and MCAs.

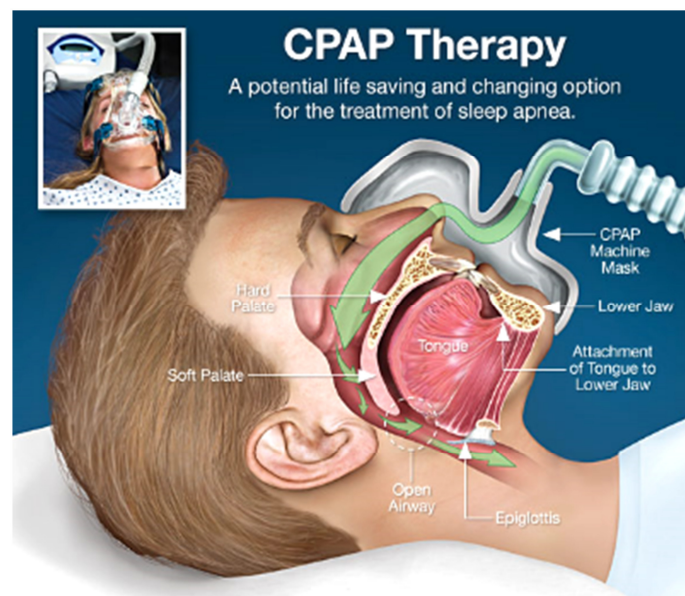


Figure 1.7 Schematic representation of patient receiving treatment with continuous positive airway(Reprint with permission from Dear Doctor Inc.)

During these measurements, the partial pressure of carbon dioxide (PCO_2) and oxygen saturation (SaO_2) were transcutaneously monitored with and without the CPAP applied. The reason for that was

because PCO_2 has a major impact on CBF, similar to the way in which hypocapnia constricts cerebral arteries and hypercapnia leads to a marked rise of CBF^{59, 60, 61}. After gaining knowledge around the subject of CPAP and CBF dynamics we extended the arm of the study in Chapter 5. The objective was to further understand the impact of CPAP on cranial blood flow (arterial and venous) and CSF dynamics with the use of 2D PC MRI measurements on healthy awake volunteers.

1.3 Chiari I malformation

CSF flow dynamics related to type I Chiari malformation (CMI) are being thoroughly investigated in the present thesis (e.g Chapters 2 and 3). CMI is a congenital craniospinal disorder in which a downward displacement of brain tissues into the spinal canal occurs. In particular, the lower part of the cerebellum, the cerebellar tonsils, hangs down through the opening at the bottom of the skull, the foramen magnum (FM), and causes blockage of spinal fluid to the spinal canal (Figure 1.8). In some cases, this blockage of the spinal canal due to CMI can cause the CSF to build up inside the SC. As the amount of CSF increases in the SC, it creates a syrinx-like cavity in the SC that results in stretching and can eventually injure the nerve fibers. CMI patients can have a variety of neurological symptoms and pain ranging from mild to severe⁶². It is thought that these symptoms result from abnormal pressure acting on the spinal cord, brain stem, and/or cerebellum due to crowding of the tissue in the craniovertebral junction⁷.

A static anatomic MRI of the brain and spine will tell whether or not a patient has CMI and the level of its severity. The traditional criterion for diagnosis of a patient with CMI is the presence of a cerebellar tonsillar herniation (CTH) greater than 5 mm below the foramen magnum. However, symptomatic CMI patients with a mild CTH below the foramen magnum (<5 mm) face the challenge of an accurate diagnosis with the traditional MRI scans though their symptoms may be very severe and may result in permanent nerve damage.

The reason CMI has been of great interest in the present thesis is that there is evidence of a complex CSF flow field present in Chiari patients^{8, 63}. Researchers have found differences in CSF velocities, pressure and resistance to flow in pre-surgery CMI patients compared to healthy subjects and post-surgery CMI patients. Detail analysis of the measurement of the CSF flow in Chiari patient is given in the next section as well as in Chapters 2 and 3 of the thesis at hand. Currently, it is unclear if the symptoms and tissue damage related to type I Chiari malformation are more the result of altered neuroanatomy or of altered CSF dynamics. Parameters such as resistance to flow and compliance of the craniospinal system are dynamic components of the CSF biomechanical environment that are not measurable by the traditional simple anatomic MRI evaluation techniques. Hydrodynamic measurements could provide doctors with more complete information in order to determine which patients will have progressive symptoms and would respond to treatment best. Thus, the combination of detailed measurement with novel *in vivo* techniques and engineering analysis of CSF hydrodynamics with the use of 3D CFD is considered as a powerful tool to better reflect the pathophysiology of the disorder and serve at the same time as a prognostic indicator of CMI.

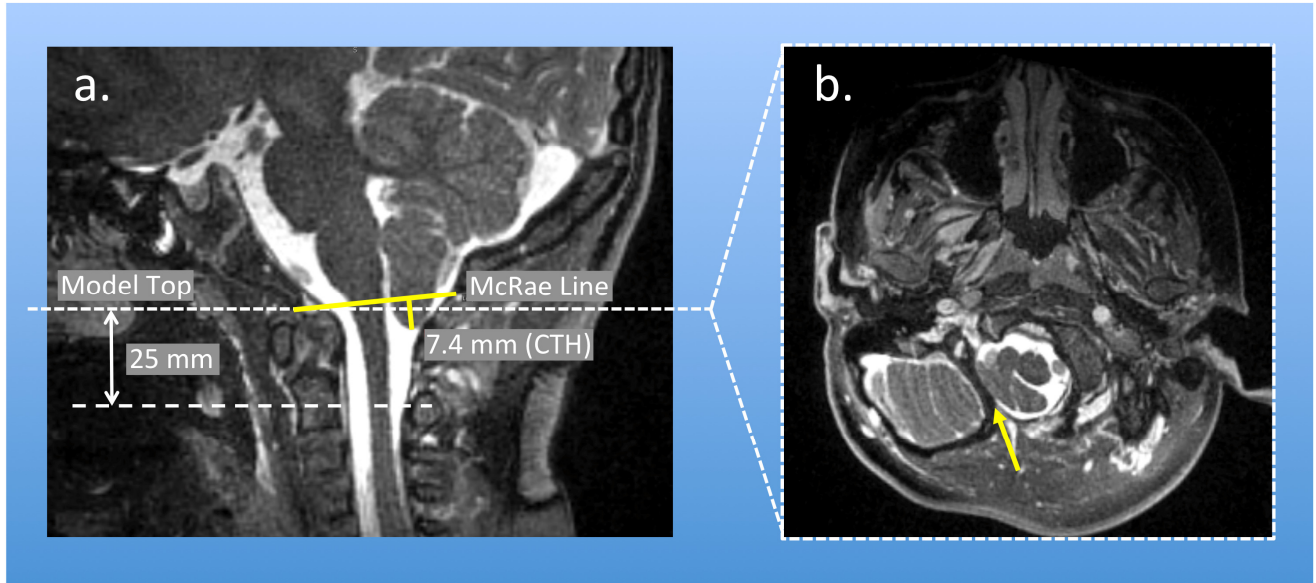


Figure 1.8 a) Midsagittal MRI image of the cervical spine of a CMI patient showing the cerebellar tonsillar herniation (approximately 7.4mm); (b) transverse MR image from the plane used to separate the top of the 3D model that was reconstructed, highlighting the separation between the cerebellar tonsils and body of the cerebellum⁶⁴.

1.4 Non invasive measurement of the craniospinal dynamics

1.4.1 Magnetic resonance imaging

Hydrodynamic measurement of the CSF flow field is useful to provide detailed information to help understand the pathophysiology of the various craniospinal disorders such as CMI. In particular, *in vivo* CSF measurements could offer doctors more complete information in order to determine which of the patients with craniospinal disorders will have progressive symptoms and would respond to the decompression surgery the best. Further, it may also be possible to gauge the success of surgical treatment with normalization of hydrodynamic parameters such as peak velocities.

Magnetic resonance imaging (MRI) has been mainly used to measure CSF and brain tissue motion within the spine and cranium in order to evaluate the CSF flow field¹²⁻¹⁵. For the last few decades, single-slice 2D phase contrast MRI (2D PC MRI) flow measurements in one direction have been the most widely explored technique, as it provides *in vivo* measurement of parameters such as peak CSF flow velocity and⁶⁵, relative timing of CSF and arterial pulsations^{48, 49, 66} and pulse wave velocity in the SSS⁶⁷. Quigley et al.¹⁰ used cardiac gated 2D PC MRI to measure spatial and temporal variation in CSF velocity at the FM in healthy volunteers and CMI patients. Results showed that in patients unlike in healthy volunteers, the flow field was characterized by flow jets, regions with a preponderance of flow in one direction, and synchronous bidirectional flow (Figure 1.9). On another study, peak CSF velocities in the craniocaudal direction of CMI patients were significantly higher than the velocities measured in healthy controls using 2D PC MRI⁹. In Chapter 5 of this thesis, we chose to use 2D PC MRI flow measurements at the C2-C3 cervical vertebrae level of healthy volunteers in order to evaluate the CSF flow as well as the total CBF from the main vessels supplying blood to the brain. The crux of this project was to explore, with the use of a specific 2D PC MR protocol, if CPAP has any impact on intracranial dynamics.

One drawback of the 2D PC MRI measurements is that they are limited by their narrow spatial coverage, which may not be representative of the entire CSF compartment of interest, and the one-dimensionality of their velocity encoding direction, i.e. either in-plane or through-plane velocity encoding. Recent advancements in the medical imaging field have entirely opened new MRI measurement methods to measure CSF and quantify CMI. Time-resolved 3D phase-contrast MRI (4D PC MRI) has been progressively thought to be well suited to estimate complex flow phenomena in the CSF-filled spaces

associated with CMI (Figure 1.10)^{8, 68-71}. 4D PC MRI may provide better diagnostic utility compared to conventional 2D PC MRI techniques, because of its three-directional information, larger field of view, and relatively small voxel size⁷². Known as one of the most detailed *in vivo* assessment tool, 4D PC MRI CSF flow measurements in the cervical SSS obtained from healthy volunteers and CMI patients were compared for the first time to 3D simulations of the same geometries in Chapter 2 of the present thesis.

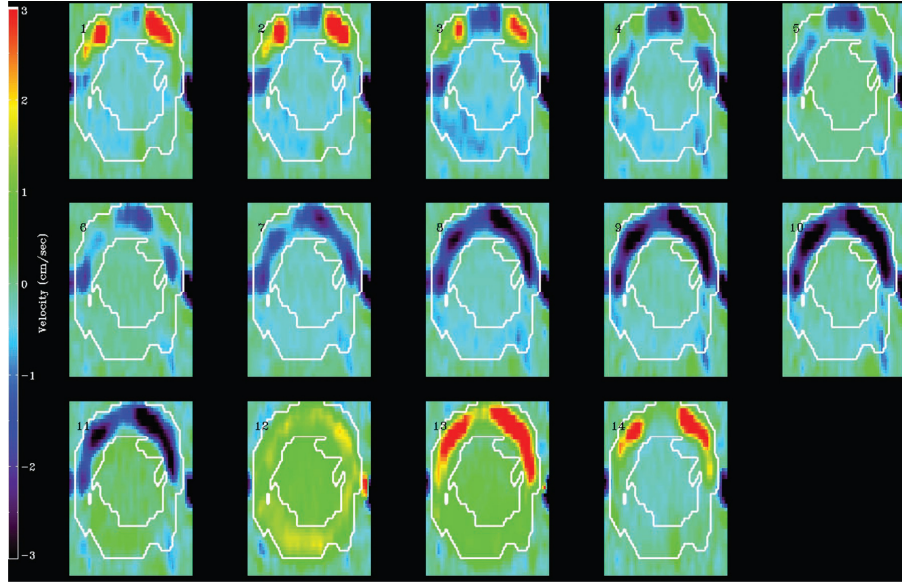


Figure 1.9 Fourteen successive transverse PC MR images of CSF flow through foramen magnum during cardiac cycle in a symptomatic Chiari I malformation patient. White lines represent the subarachnoid space. 1–5 show cranial CSF flow; 6–11, caudal CSF flow; and 13 and 14, cranial flow again. Color images show pronounced flow inhomogeneity. Regions of the anterolateral SSS have markedly elevated velocities. The posterior part of the SSS, compared to the anterior, is shown to have reduced velocities¹⁰.

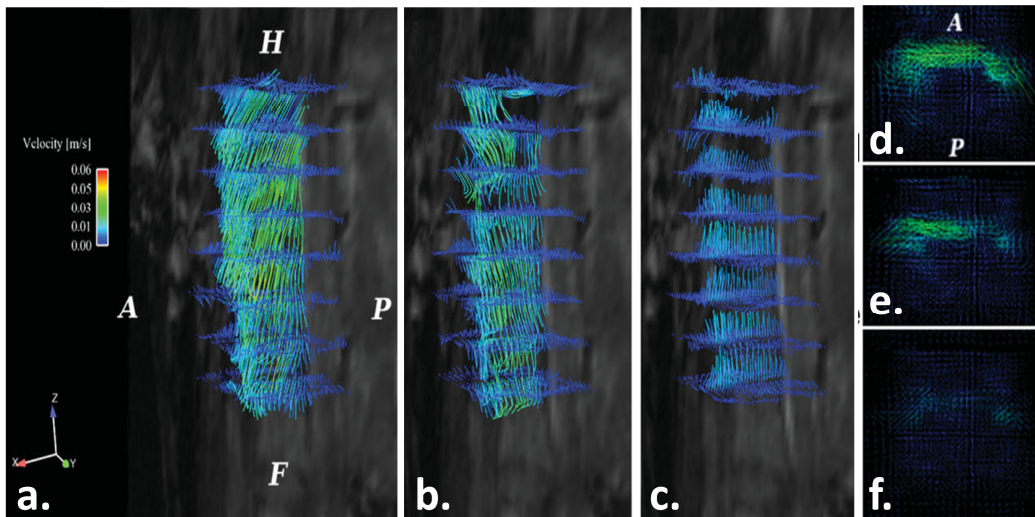


Figure 1.10 Streamlines representing CSF flow in the cervical spine (C3–C5 vertebrae level). Planes are placed axially 5 mm apart from each other. Image view is oblique sagittal/coronal approximately 45° in the left/posterior direction (frames a–c) and axial (frames d–f). Letters A–P and H–F represent the anteroposterior and head-foot directions, respectively. Vectors represent magnitude and direction of velocities of each point at three different cardiac phases: second phase after R wave (a,d), third phase(b,e), and last phase (eighth phase: c,f)⁷¹.

1.4.2 Duplex Doppler Ultrasound measurements

Duplex color Doppler Ultrasound (US) measurements were utilized in this thesis in Chapter 4 as a way to assess blood flow velocity and lumen diameter in M-mode⁷³ of all the main vessels supplying blood to the brain, such as the ICAs, VAs and MCAs (Figure 1.11) under the presence of CPAP. We chose to use US measurements to evaluate velocity rate and vessel diameter instead of transcranial Doppler US (TCD) since they do not take into account changes in the artery diameter that may occur during the CBF autoregulation because of PCO_2 . As a result, our focus was to assess the influence of CPAP on CBF dynamics. This was a primary study that helped us to move forward and investigate in Chapter 5 with the use of 2D PC MRI, the response of intracranial dynamics system (arterial, venous and CSF) to the presence of CPAP

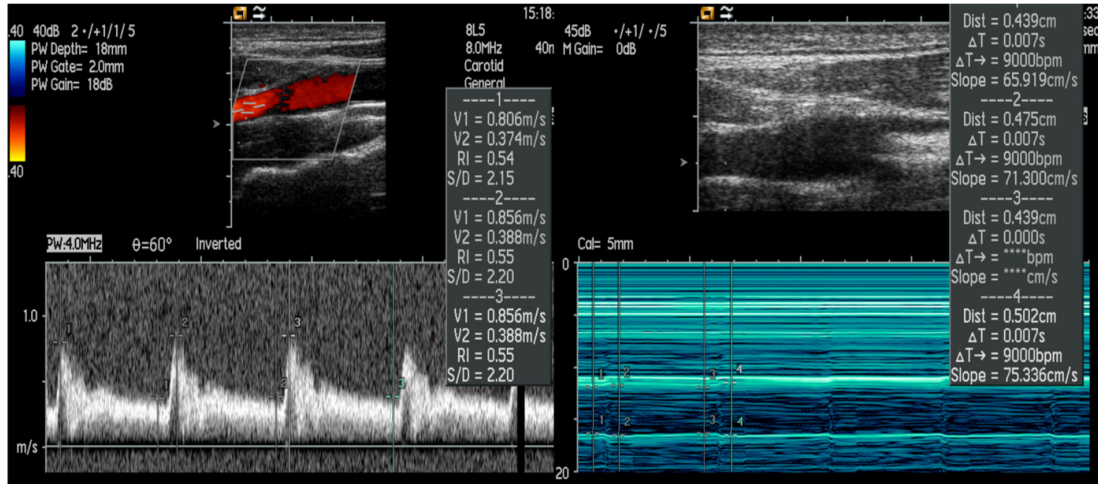


Figure 1.11 Flow velocity measurement (left) and lumen diameter in M-mode (right) at the right internal carotid

1.5 Computational fluid dynamics simulations of the CSF flow movement

Computational fluid dynamic (CFD) simulations and *in vitro* flow models based on 2D PC MRI measurements and additional anatomical data allow non-invasive analysis of the CSF flow environment in healthy and patient cases^{21-23, 74, 75}. CFD numerically simulate the flow field by approximating hydrodynamic variables, such as pressure and velocity and by solving the full Navier–Stokes equations with finite element or finite volume methods. To date, most of CFD models of the CSF flow within the craniospinal system consider the geometry of interest to be of rigid structure (Figure 1.12).

In addition, these models have incorporated various degrees of anatomical complexity with or without the inclusion of fine structures such as spinal cord nerve roots, denticulate ligaments and arachnoid trabeculae (Figure 1.13)^{75-79, 43}. In Chapter 2, a detailed literature review of the existing CFD studies of the cervical SSS CSF motion under varying levels of complexity is given.

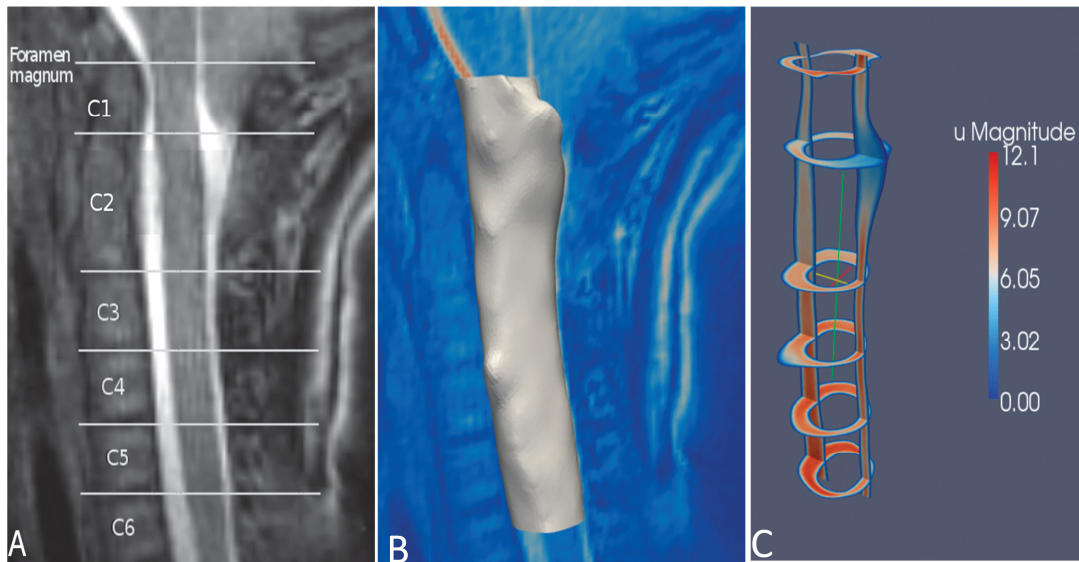


Figure 1.12 A. Sagittal MR image showing the axial orientation of the planes along the cervical spine of a patient with Chiari I malformation that will be used for the orientation of the planes in the 3D CFD model B. 3D reconstruction of craniocervical junction of a patient with Chiari I malformation C. Peak CSF velocities at each of the axial planes shown in A as well as in a sagittal plane computed by CFD simulations⁸⁰

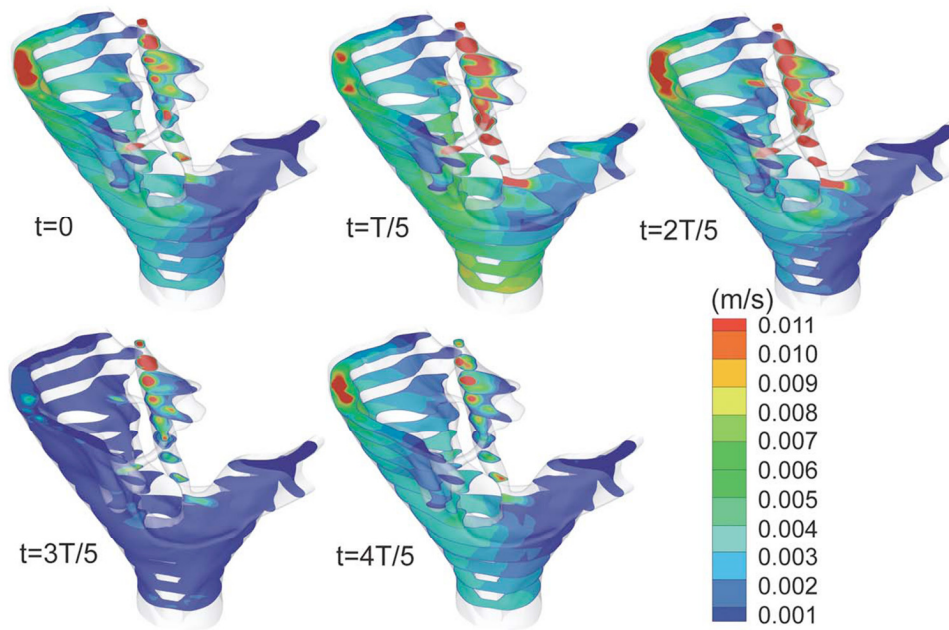


Figure 1.13 Velocity magnitude contours in the spinal subarachnoid space of anisotropic porosity of a control, over one cardiac cycle⁷⁵

Researchers have also investigated and simulated the CSF space and spinal tissue displacement by assuming the SSS to be an axisymmetric coaxial elastic tube system⁸¹⁻⁸⁴. These simulations are based on analytical solutions for wave propagation within tubes or 2D axisymmetric fluid structure interaction (FSI) simulations with simplified boundary conditions from *in vivo* measurements. These models highlighted the importance of mechanical properties of the neural tissue such as compliance and permeability and the complex fluid-structure interaction involved with the CSF flow obstruction and neural tissue. It should though be mentioned that FSI modeling of a patient specific geometry with a craniocervical disorder is complex and computationally expensive due to the additional moving geometry of the walls that is needed for each simulation.

One drawback of the computational modeling is that the numerical 3D approximation of the CSF flow field is sensitive to the boundary conditions which are obtained from the *in vivo* anatomical and flow data acquisition. For instance, due to the spatial resolution limit of the current 2D PC MRI techniques, *in vivo* measurements have provided limited information on the impact of the fine structures inside the SSS on the CSF flow field. The anatomical size of these structures is too small to quantify with the present state-of-the art MRI techniques that use ~0.5 mm isotropic resolution at 3T. Hence, it is necessary to be able to obtain accurate *in vivo* measurements of the CSF motion both in health and disease states in order to ameliorate the 3D representation by the CFD.

This need brought us to accomplishment of Chapters 2 and 3. In particular, Chapter 2 aimed at obtaining 4D PC MR measurements of the CSF flow at nine axial locations along the cervical SSS of healthy volunteers and patients with CMI. These measurements were then used as boundary conditions at anatomically simplified 3D rigid wall CFD simulations of the same subject- specific geometries. Hydrodynamic parameters such as peak velocities and thru-plane velocity profiles at peak systole were further compared between the two measurement methods. As a whole, Chapter 2 highlighted the utility of CFD in conjunction with 4D PC MRI for detailed analysis of CSF flow dynamics that could help distinguish physiological from complex pathological flow patterns at the cervical SSS.

In addition, we extended the aim of the study in Chapter 3, where we investigated the inter-operator geometric variability of the CFD modelling of the CSF movement at the craniovertebral junction. One of the geometries of the healthy subjects from Chapter 2 was segmented from 7 independent operators and simulated by CFD with the same methodology described in Chapter 2. In Chapter 3 we also attempted to identify objective CSF dynamics based parameters that are indicative of disease states, such as in peak CSF velocities, cross-sectional area, pressure, longitudinal impedance. Thus, geometric and hydrodynamic parameter variability was compared to the variability of same parameters previously documented in pre-/post-surgery CMI patients and controls.

2. Comparison of 4D phase-contrast MRI flow measurements to computational fluid dynamics simulations of cerebrospinal fluid motion in the cervical spine

Theresia I. Yiallourou¹, Jan Robert Kröger², Nikolaos Stergiopulos¹, David Maintz³, Bryn A. Martin^{4,1},
Alexander C. Bunck^{2,3}

¹Laboratory of Hemodynamics and Cardiovascular Technology,
École Polytechnique Fédérale de Lausanne, Switzerland

²Department of Clinical Radiology, University Hospital of Münster, Germany

³Department of Radiology, University Hospital of Cologne, Germany

⁴Conquer Chiari Research Center, University of Akron, OH, U.S.A.

2.1 Abstract

Cerebrospinal fluid (CSF) dynamics in the cervical spinal subarachnoid space (SSS) have been thought to be important to help diagnose and assess craniospinal disorders such as Chiari I malformation (CM). In this study we obtained time-resolved three directional velocity encoded phase-contrast MRI (4D PC MRI) in three healthy volunteers and four CM patients and compared the 4D PC MRI measurements to subject-specific 3D computational fluid dynamics (CFD) simulations. The CFD simulations considered the geometry to be rigid-walled and did not include small anatomical structures such as nerve roots, denticulate ligaments and arachnoid trabeculae. Results were compared at nine axial planes along the cervical SSS in terms of peak CSF velocities in both the cranial and caudal direction and visual interpretation of thru-plane velocity profiles. 4D PC MRI peak CSF velocities were consistently greater than the CFD peak velocities and these differences were more pronounced in CM patients than in healthy subjects. In the upper cervical SSS of CM patients the 4D PC MRI quantified stronger fluid jets than the CFD. Visual interpretation of the 4D PC MRI thru-plane velocity profiles showed greater pulsatile movement of CSF in the anterior SSS in comparison to the posterior and reduction in local CSF velocities near nerve roots. CFD velocity profiles were relatively uniform around the spinal cord for all subjects. This study represents the first comparison of 4D PC MRI measurements to CFD of CSF flow in the cervical SSS. The results highlight the utility of 4D PC MRI for evaluation of complex CSF dynamics and the need for improvement of CFD methodology. Future studies are needed to investigate whether integration of fine anatomical structures and gross motion of the brain and/or spinal cord into the computational model will lead to a better agreement between the two techniques.

Keywords

4D PC MRI, computational fluid dynamics, Chiari I malformation, cerebrospinal fluid dynamics, cervical spine, spinal subarachnoid space, spinal cord nerve roots, denticulate ligaments

2.2 Introduction

Cerebrospinal fluid (CSF) dynamics have been examined in craniospinal disorders because analysis of brain and spinal cord morphology alone has been insufficient to explain patient symptoms and surgical outcome^{18, 85}. Single-slice 2D phase contrast MR flow imaging (2D PC MRI) in the sagittal or axial orientation has been used to quantify CSF hydrodynamic parameters such as peak CSF velocities and jets in Chiari I malformation (CM)^{10, 65}, relative timing of CSF and arterial pulsations^{48, 49, 66} and pulse wave velocity in the spinal subarachnoid space (SSS)⁶⁷. However, the unidirectional encoding of 2D PC MRI CSF flow measurements does not permit quantification of 3D complexities within the CSF flow field⁸⁶. Time-resolved three-directional velocity encoded phase contrast MR imaging (4D PC MRI) has been increasingly appreciated for its potential to quantitatively and qualitatively assess CSF flow dynamics and provide insight into complex flow phenomena such as secondary flow and vortex strength that can occur in craniospinal disorders^{18, 71}. Bunck et al.⁸ found that 4D PC MRI resulted in detection of greater CSF peak velocities than single-plane 2D PC MRI measurements when assessing CSF flow in CM patients with and without a syrinx. 4D PC MRI has also been utilized to investigate the CSF flow field in the ventricles of the brain¹⁷ and in hydrocephalus patients⁸⁷.

To date, the CSF flow field obtained by 4D PC MRI has not been compared to 3D computational fluid dynamics (CFD) simulations; a helpful tool to quantify the CSF movement within the SSS and intracranial space^{75-78, 88, 89}. CFD simulations are uniquely suited for variational analysis; a technique that can be used to help assess the importance of individual anatomical aspects of the CSF system such as the spinal cord nerve roots or tonsillar descent in CM. Figure 2.1 summarizes the existing computational simulation studies of the cervical SSS CSF motion under varying levels of complexity.

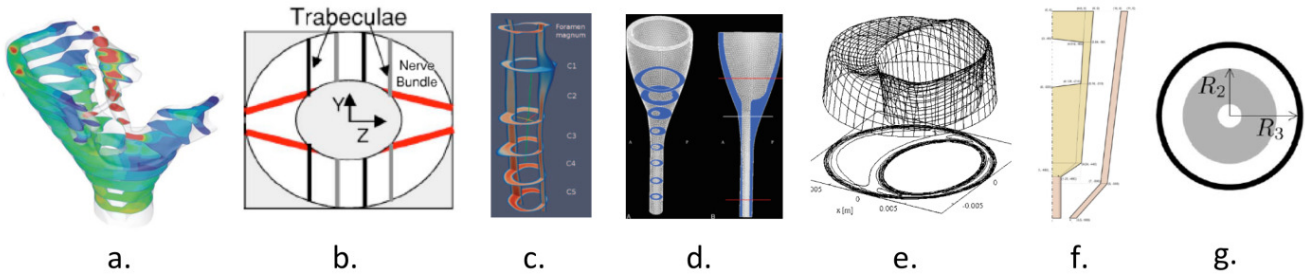


Figure 2.1. Varying levels of anatomical assumptions in the literature when simulating CSF in the cervical spine (Decreasing level of anatomical complexity from left to right, respectively). a) A subject-specific rigid wall geometry with CSF moving within a SSS of anisotropic porosity⁷⁵. b) An idealized 2D SSS geometry including spinal cord nerve roots, arachnoid trabeculae and denticulate ligaments in a symmetric arrangement around the spinal cord³⁶. c) A subject-specific 3D SSS geometry without small anatomical structures and geometric smoothing⁹⁰. d) An idealized 3D geometry of a healthy subject⁹¹. e) The first simulation of CSF in the cervical SSS idealized as two concentric ellipses⁸⁸. f) A 2D axisymmetric spinal cord and dura model with moving walls⁹². g) A 2D axisymmetric model of wave propagation in the spine based on an analytical solution of concentric elastic tubes⁹³. Refer to Table 1 for details in each simulation.

In accordance with Figure 2.1, Table 2.1 provides details for the computational studies and their anatomical simplifications. Loth et al.⁸⁸ conducted the first rigid wall CFD simulation of the CSF movement in the SSS. Small anatomical structures such as the spinal cord (SC) nerve roots, denticulate ligaments and arachnoid trabeculae were not included in the simulated geometry. Stockman³⁶ investigated the impact of small anatomical structures on the CSF flow field and found that the velocity profiles were not significantly affected by the presence of the fine structures when the spacing was symmetric around the SC. Subsequent to these studies it has generally been assumed that small structures in the SSS do not have a significant impact on macro-scale CSF velocity profiles.

Roldan et al.⁶⁸ simulated CSF in rigid geometrically realistic SSS models without fine structures based on MRI measurements. The results indicated heterogeneous CSF flow fields with anterolateral flow jets around the SC. Linge et al.⁹¹ examined the effect of anatomic variation on CSF dynamics without fine

anatomy and found the spatial variations in flow patterns to resemble those observed in PC MR studies. Rutkowska et al.⁹⁰ compared 3D rigid wall subject-specific CFD simulations of cyclic CSF flow to 2D PC MR measurements in CM patients, patients who had previous craniovertebral decompression and controls and observed that the various CSF flow patterns were greater in Chiari patients than in controls. In contrast to other studies assuming the subarachnoid space to be a strictly fluid space, Gupta et al.^{75, 89} conducted a study to simulate CSF movement within a uniformly distributed anisotropic porous media representative of the arachnoid trabeculae. Their results supported that the arachnoid trabeculae density and dimensions had a significant impact on pressure gradients and would alter kinetics of drug distribution within the CSF system.

Table 2.1. Literature review of computational simulations of CSF motion in the cervical SSS and/or craniospinal junction in healthy conditions and patients with craniospinal disorders

Author	Technique	Geometry	Tissue motion	Arachnoid trabeculae	Nerve roots
Gupta et al. ⁷⁵	CFD, anisotropic porous media	3D subject-specific	No	Yes	No
Stockman et al. ³⁶	CFD, Lattice Boltzmann	2D idealized	No	Yes	Yes
Roldan et al. ⁶⁸	3D rigid wall CFD	3D subject-specific	No	No	No
Linge et al. ⁹¹	3D rigid wall CFD	3D idealized	No	No	No
Loth et al. ⁸⁸	3D rigid wall CFD	2D concentric ellipse based on subject	No	No	No
Rutkowska et al. ⁹⁰	3D rigid wall CFD	3D patient specific	No	No	No
Bertram ⁹²	Numerical model/wave propagation	2D idealized axisymmetric, tapered tubes	Yes	No	No
Cirovic ⁹³	Numerical model/ wave propagation	2D concentric tube with constant diameter	Yes	No	No
Carpenter et al. ⁸¹ , Elliott et al. ⁹⁴ , Cirovic et al. ⁹⁵	Numerical model/wave propagation	1D coaxial, fluid-filled, elastic tubes	Yes	No	No
Elliott et al. ⁹⁶	Two multiple-compartment hydraulic circuit models	1D coaxial, fluid-filled, permeable tubes	No	No	No
Linninger et al. ⁹⁷	FSI	Multi compartment model of intracranial dynamics	Yes	No	No
Bilston et al. ⁹⁸	CFD	2D Axisymmetric, cylindrical model	Yes	No	No

Several authors have simulated the CSF flow field and spinal tissue displacement considering the SSS to be an axisymmetric coaxial elastic tube system^{82, 83, 92, 93, 99-101}. These simulations are based on analytical solutions for wave propagation within tubes or 2D axisymmetric fluid-structure interaction simulations with simplified boundary conditions from *in vivo*. These models helped to further understand the impact a stenosis and/or syrinx can have on wave propagation in the SSS and the internal stresses that might arise within the neural tissue. Martin et al.^{102, 103} conducted *in vitro* experiments to examine the importance of spinal stenosis and presence of a non-communicating syrinx on spinal CSF dynamics. Botton et al.¹⁰⁴ constructed a 3D phantom model of the intracranial pressure and CSF dynamics.

As a whole, the *in vitro* experiments and axisymmetric models, despite many anatomical simplifications, emphasized the importance of mechanical properties of the neural tissue such as compliance and permeability and the complex fluid-structure interaction involved with the CSF flow obstruction and neural tissue. Altogether these different approaches aiming to simulate CSF dynamics warrant verification by *in vivo* measurements in order to assess the extent to which the different models reflect *in vivo*. At present, 4D PC MRI can be regarded as the method that offers the best and most comprehensive insight into *in vivo* CSF dynamics. For that reason it is most suitable for a comparison to CFD models.

The aim of the present study was to compare the CSF flow field in the cervical spine, measured by a) 4D PC MRI flow imaging and b) simulated by subject specific CFD, under a variety of CSF flow conditions

(age and pathology). A variety of CSF flow conditions were examined by choosing a heterogeneous subject group of healthy volunteers and CM patients at different ages. For each subject we compared the 4D PC MRI to the CFD flow field in terms of 1) peak velocities and 2) velocity profiles. Our hypothesis was that important differences would be present between the CFD simulations and the 4D PC MRI measurements due to neglect of the small structures and tissue motion in the CFD simulations.

2.3 Materials and Methods

Ethics Statement

The MR data acquisition was performed at the Department of Radiology of Münster. The study was approved by the institutional review board of the University of Münster. Before the MR exams, written informed consent was obtained from all the healthy volunteers and CM patients. Prior to further data processing MR data were anonymized.

2.3.1 *In vivo* 4D PC MR measurements

4D PC MRI CSF velocity measurements were acquired in the cervical spine (from the foramen magnum (FM) to C7 vertebrae level) of three healthy volunteers (Healthy volunteers a, b and c) (aged 24 ± 5 years) with no history of neurological disorder or spinal trauma and four CM patients (CM 1, 2, 3 and 4) (aged 5 ± 2.8 years) (see Table 2.2 for the summary of the study population). Note that age and sex matching of the healthy volunteers and patients was not sought in this study because the primary focus was to obtain a variety of CSF flow conditions and compare them to subject specific CFD simulations. In addition, neck angulation of the subjects was not controlled.

Table 2.2. Demographic and clinical characteristics of the study population

Study population	Age/ Sex	Disorders	Symptoms	Flow abnormalities	Tonsillar herniation (mm)
Healthy volunteers a-c	28/F, 22/M, 22/M	None	None	None	N/A
CM 1	7/F	CM	Asymptomatic	Unilateral flow jet	28.9
CM 2	7/F	CM	Migraine	Inhomogeneous flow	16.4
CM 3	1/M	CM	Complex syndrome	Bilateral flow jets and bidirectional flow	10.3
CM 4	5/M	CM	Impaired balance, lack of concentration	Unilateral flow jets	5.8

4D PC MRI measurements were taken on a 1.5 T MRI scanner (Achieva 2.6 scanner, Philips, Best the Netherlands) with a standard 16-channel head and neck coil, using the sequence parameters as described in the protocol by Bunck et al. ¹⁸. In brief, for 4D PC MRI imaging a retrospectively ECG-triggered, T1-weighted, segmented gradient echo sequence (T1-TFE) with a three directional velocity encoding and an isotropic resolution of 1.5 mm was used (reconstructed voxel resolution: 1 mm). Encoding velocity was set to 10 cm/s in healthy volunteers and 20 cm/s in all patients. For PC measurements a local phase correction (LPC) filter provided by the manufacturer was used to subtract the background offset caused by eddy currents. The image volume was aligned in the sagittal plane with the 3D stack covering the craniocervical junction and the entire cervical thecal sac. Imaging time varied between 8 and 14 minutes depending on the individual heart rate and encoding velocity factor.

To define the cervical spine geometry for the CFD simulations, a high resolution T2-weighted 3D, turbo spin-echo sequence (VISTA) with an isotropic spatial resolution of 0.8 mm was obtained. The 3D

field of view was adjusted to anatomical dimensions, laterally securely extending beyond the inner confinement of the FM.

Motion of the cerebellar tonsils in the sagittal plane during the cardiac cycle was obtained using a retrospective ECG-triggered balanced TFE sequence with an acquired spatial resolution of 1x1 mm (reconstructed in-plane voxel resolution: 0.4 mm) and a slice thickness of 6 mm. A single slice in the sagittal midplane was acquired with 30 heart phases, 70% phase percentage and a 50° flip angle.

2.3.2 CFD simulation

The three-dimensional anatomy of the cervical SSS was reconstructed for each subject from the T2 weighted VISTA MRI images with manual segmentation using ITK Snap software (Version 2.2.0, PA) (Figure 2.2). The lower cervical spine was manually segmented approximately 5 cm caudal to C7, beyond the region of flow comparison. Spinal cord nerve roots, denticulate ligaments and other fine anatomical structures were not taken into account in the segmentation. Careful attention was given to exclude the epidural space outside of the dural confinement. The 3D geometry was smoothed with a Laplacian smoothing using MeshLab software (Version 1.3.0, Italy, Rome). A rigid wall unstructured computational grid was generated within the ANSYS ICEM CFD software (Version 13.0, Canonsburg, PA) consisting of approximately two million tetrahedral elements.

A subject specific CSF flow waveform was imposed for each CFD simulation based on the following methodology (See Figure 2.3). The CSF flow waveform was obtained at nine axial locations along the SSS (FM to C7) based on the 4D PC MRI measurements for each subject. CSF flow was determined by integrating the pixel velocities within the region of interest (ROI) at each axial location (see data processing and analysis for details on ROI selection). Based on a CFD study by Loth et al.⁸⁸, the CSF flow waveform at each axial location was offset so the net CSF flow per cycle was zero (net flow in the SSS is known to be nearly zero). The average offset for all subjects was relatively small compared to the peak flow rates (-0.23 ± 0.10 cm/s).

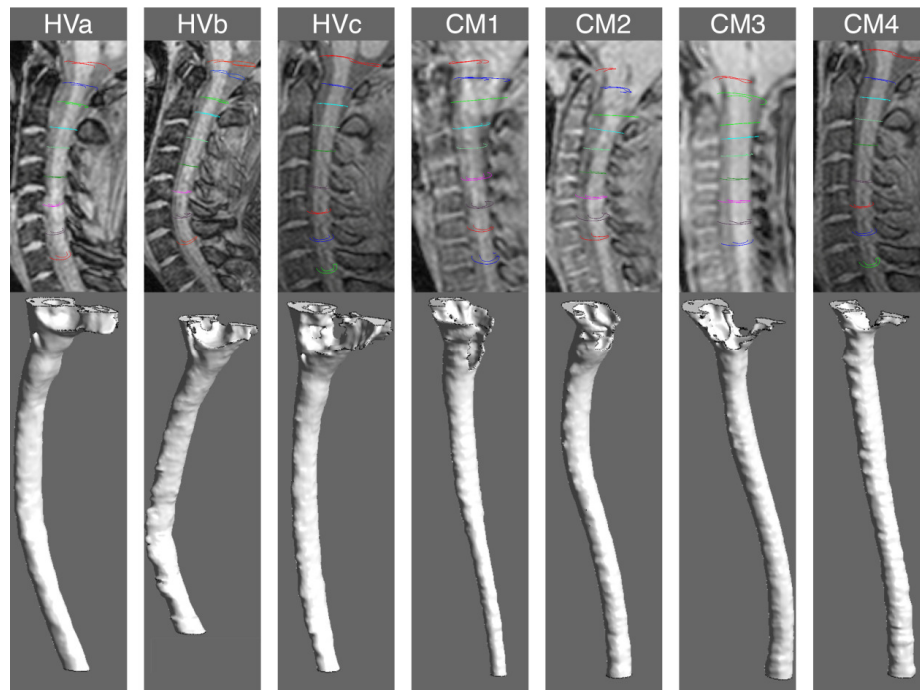


Figure 2.2. 3D reconstruction of the cervical SSS based on manual segmentation of the healthy subjects (left) and CM patients (right). The 3D reconstruction depicts the SSS where the CSF pulsates (between the dura and spinal cord tissue). Note the SSS constriction near the FM in the four CM patients in comparison to the healthy subjects.

The CSF flow waveform from the axial location with the greatest peak flow rate was selected for the inlet boundary condition of the CFD simulation. This location was selected to assure that the CFD results did not under predict CSF velocities and because a higher fidelity MRI signal is expected within a ROI with greater CSF movement. For our study, the axial location with the greatest CSF flow rate was located at the C1, C2M or the C3 level for all subjects. Systolic CSF flow occurred in the cranial-caudal direction. Based on the CSF flow waveform, a blunt CSF velocity profile was imposed at the flow inlet on the caudal end of the CFD model (approximately 5 cm below C7). The caudal end of the model was chosen as an inlet to allow for a fully developed velocity profile within the ROI (FM to C7). A no-slip boundary condition was specified at the walls. Similar to other CSF CFD studies in the literature^{68 105}, a zero pressure boundary condition was imposed at the flow outlet on the cranial end of each CFD simulation.

The Navier-Stokes equations were solved numerically by the commercial finite volume CFD solver ANSYS CFX (Version 13.0, Canonsburg, PA), resulting in a flow velocity vector and a pressure scalar at each point of the computational mesh. CSF was modeled as an incompressible Newtonian fluid with the hydrodynamic characteristics of water at body temperature^{106, 107} (density of $\rho=1000\text{kg/}$ and dynamic viscosity of $\mu=0.001\text{Pa}\cdot\text{s}$). Flow was assumed to be laminar. ANSYS CFX uses an element-based finite volume method to solve the Navier-Stokes equations by implementing the Gauss' Divergence Theorem to convert volume integrals involving divergence and gradient operators to surface integrals. Within the CFX solver settings, the utilized advection scheme had second order accuracy. The utilized transient time-stepping scheme was second order implicit backward Euler. The root mean square residual (RMS) was set to $1\cdot 10^{-4}$ as a convergence criterion. Each CFD simulation took approximately 8 hours to complete in parallel on a computer with 8 processors and 12-GB RAM. The total simulation time was sufficient for temporal periodicity to be established.

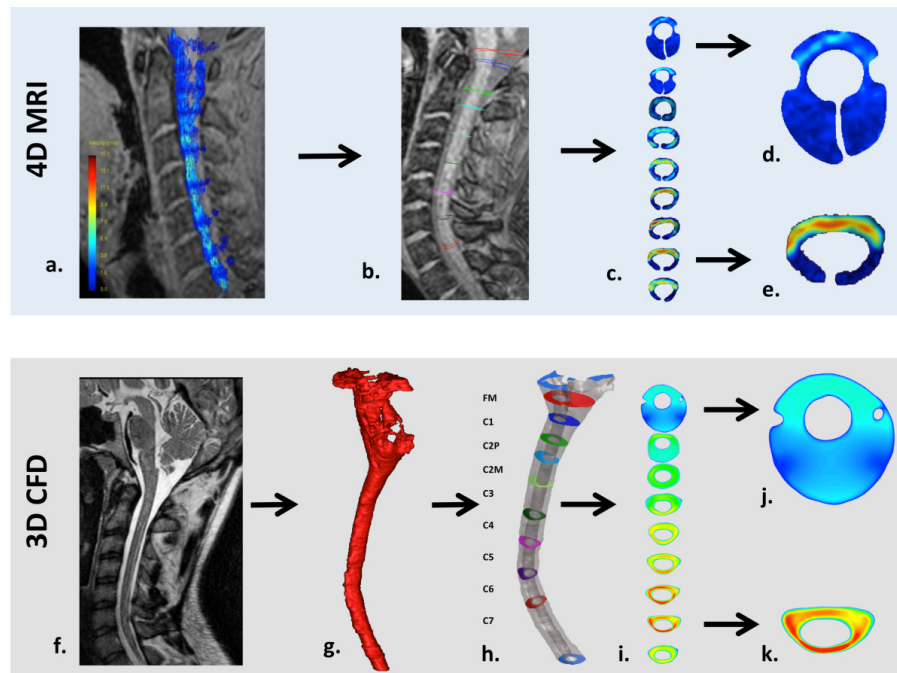


Figure 2.3. Workflow for 4D PC MRI (top row) and CFD (bottom) methodology in a healthy volunteer. **a)** 4D PC MRI velocity vectors superimposed on the coarse 2D anatomy scan. **b)** Placement of axial planes along the cervical SSS and **c)** 2D velocity profile visualization of the axial planes. **d)** Velocity profile example at the FM where ROI image truncation was required due to low velocities and noise in the MRI signal (see Methods for details). **e)** Velocity profile in the lower cervical SSS where the ROI required less image truncation. **f)** High resolution anatomical MRI scan used to define the geometry for the CFD simulation. **g)** 3D rendering of the cervical SSS segmentation before end truncation and geometric smoothing. **h)** 3D rendering of the smoothed cervical SSS geometry and axial planes where the CFD velocity profiles were observed. **i)** 2D velocity profile plots for each axial location. **j)** Velocity profile at the FM showing a larger cross-section than the FM in the 4D PC MRI (compare to d). **k)** Velocity profile in the lower cervical SSS that compares more favorably in terms of ROI size and shape to that observed in the 4D PC MRI (e).

Grid and time step independence studies were carried out with the following methodology. Three grid sizes with tetrahedral elements were analyzed having 1,310,000 (coarse), 2,860,000 (medium) and 3,800,000 (fine) elements. Pressure and velocity contours at several cross-sections of the domain were compared at different simulation times during the third simulation flow cycle. We assessed maximum relative error, e , based on the following formula,

$$e = \max \left(\left| \frac{V_{w\text{fine}}(t_{\text{sys}}, x) - V_{w\text{medium}}(t_{\text{sys}}, x)}{V_{w\text{fine}}(t_{\text{sys}}, x)} \right| \right) \times 100$$

where V_w is the velocity in the z direction calculated at the time step, t_{sys} , corresponding to peak systolic flow within the cardiac cycle and x is the spatial position along a vector located within each cross-section (axial planes FM, C3 and C7). The subscripts “fine” and “medium” refer to calculations carried out with the fine and medium grid respectively. We used the same formula to estimate the relative error between the coarse and medium grids. Following confirmation that the medium grid was sufficient to capture the important flow features, the CFD simulations were carried out with the medium grid. Time-step independence was assessed by carrying out the computations for the first period using time step sizes of $T/100$, $T/1,000$ and $T/10,000$ where T is the length of one cardiac cycle for each subject. The time step size utilized for our presented simulation results was $T/1000$.

2.3.3 Data processing and analysis

Data processing of the 4D PC MRI data sets, flow quantification and flow visualisation was carried out using the GTFlow software (Version 1.6.4, Gyrotools Ltd., Zurich, Switzerland). For flow quantification, the ROIs were manually defined in the axial orientation orthogonal to the spinal axis at the level of the FM and every cervical vertebra including the middle of C2 (FM, C1, C2M, C2P, C3, C4, C5, C6, C7; see Figure 2.3b for typical ROI orientation). Special care was taken to avoid regions within the ROIs with high velocities that occurred due to vascular blood flow. Differentiation between high CSF flow velocities due to anatomical restrictions and low vascular flow velocities was visually performed based on the PC images by assessing direction of flow over time. While the direction of blood flow does not change over time, i.e. flow is either directed caudally for venous blood or cranially for arterial blood, flow direction of CSF changes from the caudal direction during systole to the cranial direction during diastole. The ROI axial planes with high velocities due to vascular flow were typically located at the FM level near the left and right vertebral and the basilar artery. In some cases the ROI at the FM and C1 required partial truncation due to lack of signal and/or noise in the 4D PC MRI signal (Figure 2.3c, d, and e) and because of high arterial blood flow velocities. It should be noted that the post-processing software ROI selection was limited to one closed shape region at each axial level. Thus, each ROI had a “cuff” shape located around the spinal cord, with each tip of the cuff located on the posterior side of the spinal cord where lower CSF velocities were present. In the regions where the spinal cord was completely surrounded by CSF, the tips of the “cuff” shaped ROI were adjusted to touch, resulting in a virtually ring-like shape. Overall, the ROI shapes were adjusted to include all relevant flow components by correcting the shape based on the velocity encoded PC images. By these means it was assured that peak velocities were not missed.

The 4D PC MRI measurements and CFD simulation results were compared in terms of 1) peak velocities and 2) visual inspection of the velocity profiles for each ROI along the spine. Axial planes were placed along the CFD simulated geometries with the same orientation and location as the 4D PC MRI ROIs. For each plane the peak thru-plane systolic (caudal) and diastolic (cranial) flow velocities were quantified. For each axial level along the spine the average and standard deviation of the peak caudal and cranial velocities were determined for the three healthy subjects and four CM patients. In addition, the flow was assessed visually to understand any differences in velocity profiles if present. We focused on a) anterior versus posterior flow differences, b) presence of flow jets and c) flow near the nerve roots. The CSF stroke volume (SV) for each ROI along the spine was determined by integrating the absolute value of the CSF flow waveform and dividing the integrated value by two (total pulsatile volume moving through an ROI).

Motion of the cerebellar tonsils during the cardiac cycle was assessed at the mid-sagittal plane near the FM for one healthy volunteer (Healthy c) and four CM patients using the following methodology. Based on the ECG-triggered balanced TFE cine images, the image with the maximum rostral and caudal displacement of the tonsils was selected by visual estimation of the tonsil position. The individual pixel values in the rostral and caudal displacement image were subtracted from one another to produce a transparent threshold image mask (aqua colour) that was overlaid on the original tonsil position with maximum rostral displacement. Thus, the space in the image without any transparent aqua masking corresponded to regions where the tissue moved during the cardiac cycle and vice versa. This provides a visualization of the level of tissue motion in each subject.

2.4 Results

2.4.1 Peak velocities

4D PC MRI data sets were acquired for three healthy subjects and four CM patients. The mean thru-plane peak cranial and caudal velocities measured by 4D PC MRI and simulated by CFD at different axial locations along the cervical spine are presented in Figure 2.4. All velocities are given as mean \pm SD cm/s. Positive and negative velocities reflect head and foot directed flow, respectively. The 4D PC MRI velocity measurements were consistently greater in magnitude than the CFD simulations. For healthy subjects at the FM, 4D PC MRI average peak caudal and cranial velocities were -5.2 ± 1.8 cm/s and 4.2 ± 2.5 cm/s, respectively. In contrast, average CFD velocities at the FM were -1.1 ± 0.3 cm/s and 0.5 ± 0.0 cm/s, respectively in healthy subjects. The difference between 4D PC MRI and CFD velocities was greater in the CM patients. For CM patients at the FM, 4D PC MRI average peak caudal and cranial velocities were -11.8 ± 9.0 cm/s and 6.2 ± 4.7 cm/s, respectively. For CM patients at the FM, average CFD velocities were -2.9 ± 0.6 cm/s and 1.8 ± 0.5 cm/s, respectively.

While the focus of this paper was not to differentiate healthy from CMI patients in terms of their velocities, a number of differences were observed in the two groups. Overall, the 4D PC MRI measurements had a greater standard deviation of peak velocities than the CFD results for both the healthy and CMI patients. In CMI patients the greatest standard deviation of peak velocities occurred in peak systole at the FM and C1 level for the 4D PC MRI measurements. In the healthy group, we noted that the greatest differences between the average CFD peak velocities and the 4D PC MRI peak velocities occurred in systole (caudal directed flow) at the C3 to C6 level. In contrast, in the CMI patients the greatest differences in average peak velocities occurred at the FM and C1 level (Figure 2.4).

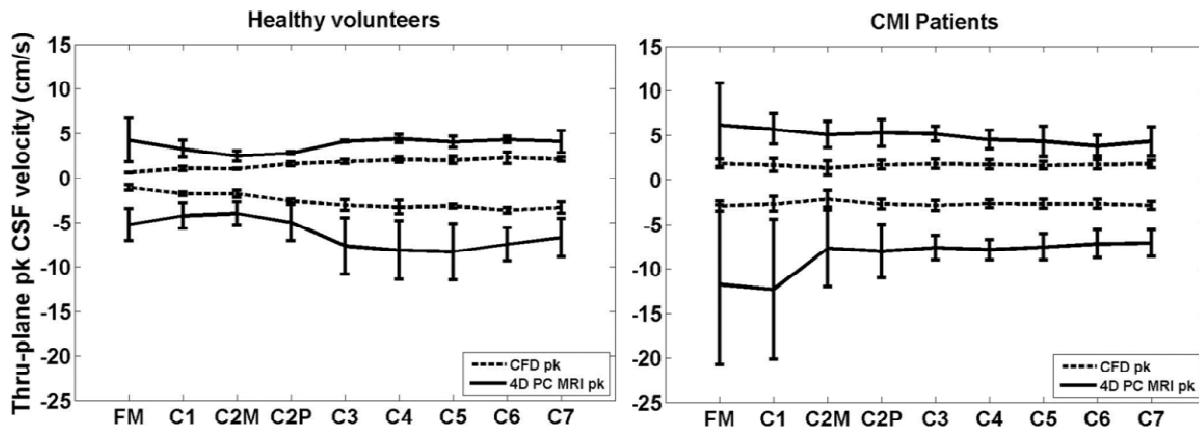


Figure 2.4. Comparison of the peak systolic and diastolic velocities that were measured by the 4D PC MRI and simulated by CFD in the cervical spine (FM-C7, FM is near the head and C7 is towards the feet) in healthy volunteers (Healthy a, b and c) and CM patients (CM 1, 2, 3, and 4). Values are given as mean \pm SD (cm/s) for the three healthy subjects (top) and four CM patients (bottom). Positive (diastolic) and negative (systolic) velocities reflect head and foot directed flow, respectively.

2.4.2 Velocity profiles

Visual inspection of the 4D PC MRI and CFD thru-plane velocity profiles at peak systole revealed large spatial differences in flow patterns (Figures 2.5 and 2.6). Colours indicate the magnitude of thru-plane axial velocity (caudal direction).

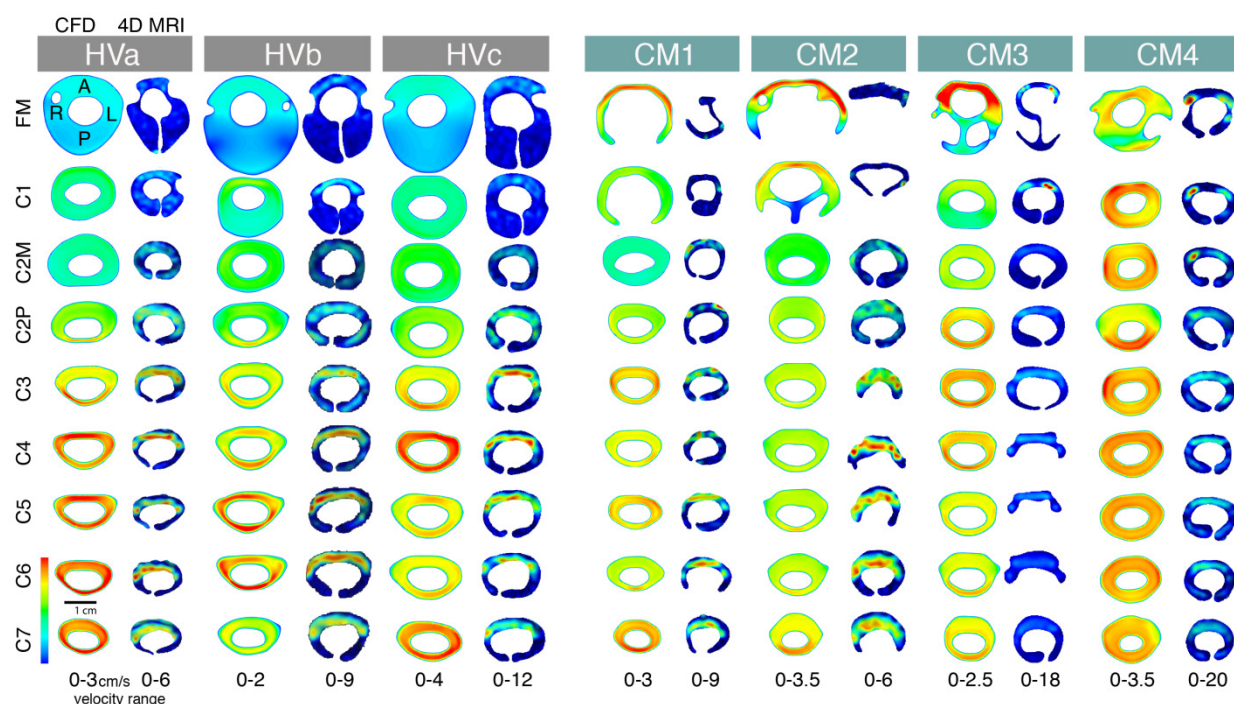


Figure 2.5. Thru-plane peak CSF velocity profiles (foot direction) at each axial location along the cervical spine. The left and right image for each subject corresponds to the CFD simulation and 4D PC MRI measurements along the cervical spine (FM-C7 level), respectively. CSF velocities were elevated in the anterior SSS in comparison to the posterior space in all of the 4D PC MRI velocity profiles (healthy and patients). The posterior versus anterior flow differences were not present in the CFD results; which maintained a fairly uniform velocity profile around the spinal cord in all simulations except CM 1 and CM 2 near the FM. Note, velocity scales are different for each image (shown at bottom of each image set) so as to highlight the difference in velocity profiles.

Greater CSF velocities were observed by 4D PC MRI in the anterior SSS in comparison to the posterior space in all healthy subjects and CM patients. In contrast, relatively uniform CSF flow profiles were simulated by CFD. Two of the four Chiari patients (CM 3 and 4) showed flow jets on the 4D PC MR images (see CM3 at FM and C1; CM4 at FM, C1 and C2M). No such flow jets were present in the corresponding CFD velocity profiles. The flow jets were unilateral in both subjects. Velocity profile was skewed to the narrower posterior subarachnoid space in a number of the CFD simulations (see HVa at C3; HVb at C2P, C3 and C4; HVc at C3 and C6; CM2 at C7; CM3 at C2P, C6 and C7; CM4 at C2P). In the 4D PC MRI images, velocity profiles were not skewed to the posterior subarachnoid space in any of the measurement planes. Instead, relatively high and concentrated regions (jets) of CSF flow were observed throughout the anterior subarachnoid space for the healthy and CMI group 4D PC MRI measurements. Figure 2.6 shows a detailed view of the 4D PC MRI and CFD velocity profiles for a healthy subject (healthy a) and CM1 patient (from C2P – C7 level). The ↑ and + symbols highlight anterior dominated CSF flow and reduced CSF velocities near nerve roots, respectively. In HVa at C2P and C3, and in CM1 at C6, the CFD velocity profiles are skewed posterior to the cord while in all of the 4D PC MRI planes the velocity profile is skewed to the anterior to a great degree. The velocity profile at peak systole measured by 4D PC MRI was much rougher than the smooth uniform velocity profiles simulated in CFD. Localized velocity jets were observed on each side of the cord in HVa and to a lesser degree in CM1.

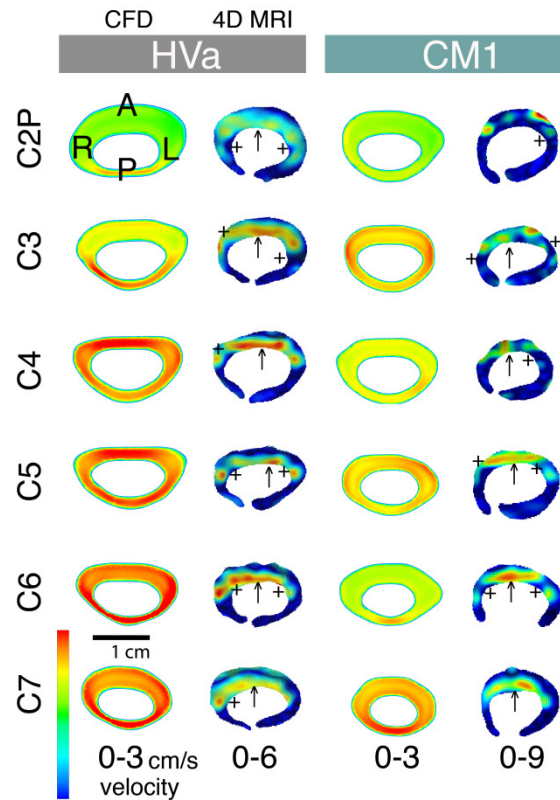


Figure 2.6. Comparison of the peak systolic thru-plane CSF velocity profiles between the 4D PC MRI and CFD for HVa (left) and CM1 (right). Note the different velocity scales for each plot (optimized for visualization of flow profiles in each case). Colors indicate the magnitude of thru-plane velocities. ↑ symbols highlight the elevated anterior CSF velocities in comparison to the posterior that were observed in all of the 4D PC MRI velocity profiles (healthy and patients). The posterior versus anterior flow differences were not present in the CFD simulations (see Figure 2.5). + symbols indicate locations where the nerve roots appear to local CSF velocities.

2.4.3 Motion of cerebellar tonsils

Motion of the cerebellar tonsils during the cardiac cycle is depicted in Figure 2.7 (top row) for the four CM patients and one healthy subject (hvc). Regions without a blue mask colour highlight tonsillar motion. As a whole, healthy subjects had less tonsillar motion than the CM patients. CM 1, 2 and 4 had greater tonsillar motion than CM 3. Motion of the spinal cord was also noted near the brain stem in CM1 and CM2, while in CM3 and CM4 little motion was present at the brain stem. CSF flow over the cardiac cycle at C1 and C2M vertebrae level (middle row) and total SV at various axial locations along the SSS (bottom row), as obtained from the 4D PC MRI measurements, are shown below the tonsillar motion image for each subject. The CSF flow waveform at C1 and C2M was very similar in Hvc, CM3 and CM4. In CM1 and CM2 the waveform varied a great degree in terms of shape and amplitude. Stroke volume (SV) varied a great degree at different axial locations along the spine for the subjects in our study. At the FM, SV was greatest in healthy subjects at about 0.76 ml per CSF flow cycle. In the CMI patients, SV at the FM varied from nearly zero, in CM1 and CM2, to approximately 0.3 ml, in CM3 and CM4. Interestingly, the two patients with the greatest reduction in SV (CM1 and CM2) at the FM had the greatest brain motion. The two patients with a smaller level of brain motion had a smaller reduction in SV near the FM. Below the C2P level, SV decreased along the spine in the healthy subject while in the CM patients SV remained fairly uniform.

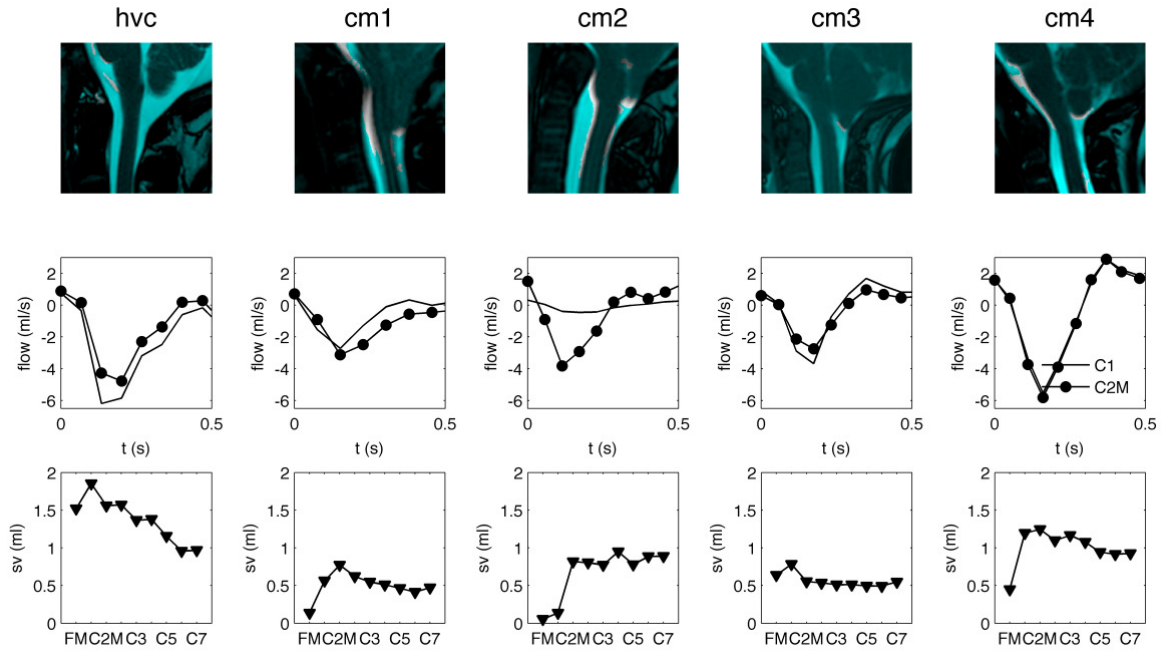


Figure 2.7. Motion analysis of the MRI images for healthy subject c (Hty c) and CM patients. Pixels in the image that are not masked in blue indicate tissue regions of the brain/spinal cord that move during the cardiac cycle. The larger the region, the greater the tissue motion; e.g. CM1, CM2 and CM4 appear to have the greater level of tissue motion in comparison to CM3. Unsteady CSF flow measured at the C1 and C2M is shown in the center row for each patient. CSF stroke volume (SV) at each axial location along the SSS (FM – C7) is shown in the bottom row for each subject.

2.4.4 Independence studies

Figure 2.8 shows the z-direction velocity, Velocity w at peak systole for a selected vector within the axial planes located at FM (a), C3 (b), C7 (c) for the coarse, medium and fine grid simulation performed with a $T/1,000$ time step size. Time-step independence studies showed graphically indistinguishable results, especially in the cases of the medium and fine mesh. The maximum relative error, e , was 20% for the coarse to medium grid and 5% for the medium to fine grid.

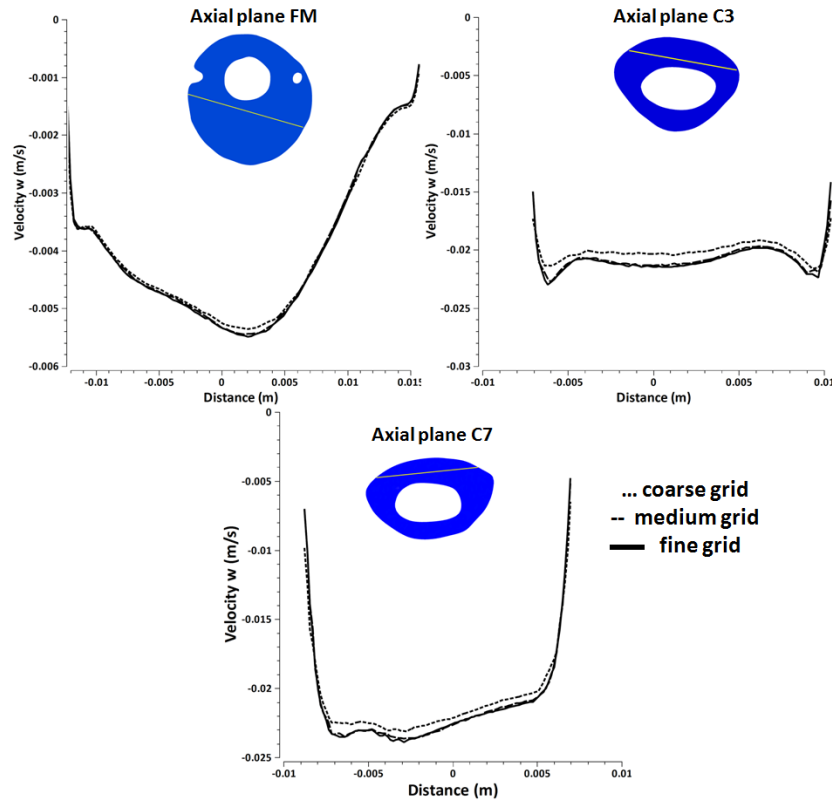


Figure 2.8. Plots of peak systolic velocity in the z direction (velocity w) along vectors through the cervical spinal cord for three different axial locations as calculated with three grids (a) Velocity- w along the vector at the cross-section of axial plane FM, (b) Velocity- w along the vector at the cross-section of axial plane C3 (c) Velocity- w along the vector at the cross-section of axial plane C7.

2.5 Discussion

In the present study we focus on analysis of CSF dynamics present in the cervical SSS by comparing 4D PC MRI measurements to subject-specific rigid wall and anatomically simplified CFD simulations. Our goal was to compare these two possibly important techniques to better understand their potential to assess CSF dynamics in healthy and diseased conditions. We compared the two techniques in terms of 1) peak velocities and 2) visual inspection of velocity profiles since both of them are regarded as possible indicators of symptomatic patients with CM. As such, those two factors, when visualized with 4D PC flow imaging and in combination with CFD simulations, may help to more precisely identify patients who are likely to benefit from craniocervical decompression.

Our results showed that the 4D PC MRI measurements and CFD simulations did not have similar CSF dynamics in terms of peak velocities or velocity profiles over a heterogeneous range of CSF flow conditions in terms of age, sex and pathology. These differences were more pronounced in CM patients particularly near the FM. We hypothesize that the differences can be accounted for due to i) neglect of small structures and/or tissue motion in the cervical SSS in the CFD simulation and ii) noise in the 4D PC MRI measurements.

Potential reasons for different peak CSF velocities

Our results supported that thru-plane peak systolic velocities were consistently greater in magnitude for the 4D PC MRI measurements than the CFD simulations in both healthy subjects and CM patients (Figure 2.4). These velocity differences were more pronounced in CM patients compared to healthy volunteers, in particular at the level of the FM. The lower peak velocities in the CFD simulations in comparison to the 4D PC MRI measurements could be due to the following reasons a) overestimation of the SSS cross-sectional area, b) underestimation of the CFD input flow boundary condition, c) non-uniform porosity of the SSS, d) structural motion of the neural tissue, e) noise in the 4D PC MRI measurements. We conjecture c, d, and e to be the most plausible.

a) Overestimation of the SSS cross-sectional area

The 3D CFD geometry was manually segmented based on the high-resolution VISTA MRI geometry scans. It is possible that the CFD geometry cross-sectional area was larger than *in vivo* thus resulting in lower peak velocities due to the linear relation of velocity and cross-sectional area for an incompressible fluid moving in a rigid conduit. However, we do not expect this to be the case since the velocity differences occurred along the entire cervical spine and because these differences were 4X greater in some cases. For this to occur, the manual segmentation would need to be incorrect by a factor of four or more. Nonetheless, in our study the manual segmentation for each subject was checked by two radiologists and confirmed to be representative of *in vivo*.

b) Underestimation of the CFD input flow boundary condition

Similar to overestimation of cross-sectional area, underestimation of the input flow boundary condition for the CFD simulation would result in lower peak velocities. However, our methods involved carefully specifying the input boundary condition with the greatest peak flow rate and thus we do not expect an underestimation of the flow boundary condition but rather possibly an overestimation. The CSF flow waveform amplitude, that was quantified at different axial levels by 4D PC MRI, was found to vary along the cervical spine; presumably due to compliance of the SSS (see Figures 2.5, 2.6 and 2.7)⁸. To some extent, these variations may be attributed to noise in the 4D PC MRI signal in regions with low velocities and structural motion of the tissue (see below for more on structural motion). For the CFD simulation flow boundary condition, we chose to use the CSF flow waveform with the greatest peak flow value (caudal direction) reasoning that at this location signal to noise would be better than other regions. The selected location was at C1, C2M or C3 for the study population.

c) Inhomogeneous porosity of the SSS

Our 4D PC MRI measurements show a dominance of anterior CSF velocities in comparison to the posterior cervical SSS (Figures 2.4 and 2.5). In contrast, the CFD simulations did not show anterior dominance of CSF velocity in any of the simulations. Instead, the velocity profile was skewed to the narrower posterior subarachnoid space in a number of the CFD simulations. We suspect that these differences are due to inhomogeneous distribution of arachnoid trabeculae or other fine anatomical structures that result in preferential CSF movement through the anterior SSS in the cervical SSS. However, the CFD simulation considered the SSS to be a fluid continuum in which the fine anatomical structures were neglected. If these structures were present the SSS cross-sectional area would be reduced and thus peak velocities would increase. Additionally, a study in the literature has shown that the arachnoid trabeculae were more densely packed in the posterior SSS³⁷. Under this condition CSF would move more freely on the anterior SSS and thus CSF velocities in this region would be greater.

d) Structural motion of the neural tissue

The CFD simulation did not take into account structural motion of the neural tissue. However, it was clear that structural motion was present, particularly in the patients near the FM (Figure 2.7). Unsurprisingly, the CFD and 4D PC MRI results deviated from one another to the greatest degree in patients near the FM. The motion analysis of the cerebellar tonsils during the cardiac cycle showed descent of the tonsils during systole. Thus, at this time point the cross-sectional area of the SSS would be reduced and make CSF velocities in this region increase. However, the motion of the tonsils was not taken into account by the CFD simulation likely resulting in lower peak velocities. While tissue motion at the cerebellar tonsils may account for velocity differences near the FM, it would not account for velocity differences in the middle/lower cervical spine that were observed in our study where little tissue motion was observed in any of the subjects. As a result, in these regions it is more plausible that peak flow differences were due to either a, b, or c as mentioned above.

e) Noise in the 4D PC MRI measurements

It has been argued above that the difference in 4D PC MRI and CFD results can be accounted for by oversimplification of the CFD simulation. However, it should be noted that the 4D PC MRI measurement methodology also needs improvement. Phase contrast imaging requires a maximum measurable velocity to be set so as to balance noise and phase aliasing. In order to correctly detect high velocities and avoid aliasing artifacts, the sequence presets had to be adjusted to higher velocity encoding factors in Chiari patients than healthy volunteers (see methods). By choosing a higher velocity encoding factor, the sensitivity for the detection of slow flow components was reduced and may have led to an underestimation of slow flow. By these means, overall flow rates which were used as inlet flow boundary conditions may have been underestimated. New techniques using multiple velocity encoding schemes aim at increasing the overall sensitivity for a wider range of flow velocities and reduce the velocity-to-noise ratios¹⁰⁸.

Bunck et al.⁶³ evaluated the accuracy of the 4D PC MR sequence by comparing CSF flow velocities as measured by a conventional 2D PC MRI to 4D PC MRI sequence at four representative sites of the cervical canal. The comparison showed an overall good agreement of peak velocities in healthy volunteers with only a small bias. With no 2D PC data acquired in their patient population, future studies are required to assess how 4D PC MRI could be compared with conventional 2D PC flow imaging and whether it adds clinically valuable information. Long acquisition times make the 4D PC imaging prone to motion artifacts that could increase the noise level. This technique also requires a significant level of pre-processing and filtering of the data for analysis. Each step of post-processing can introduce error to the measurements.

Different velocity profiles and importance of small anatomy

The 4D PC MRI CSF velocity profiles showed a strong dominance of flow on the anterior SSS in comparison to the posterior (Figures 2.5 and 2.6) while CFD velocity profiles were fairly uniform along the cervical spine except near the FM in CM 1 and CM 2 patients. One might argue that the 4D PC MRI measurements are suspect since they have spatial and temporal limitations. However, the MRI flow measurement generally improves with flow velocity. Thus, while the noise that is present on the posterior spinal cord 4D PC MRI measurements does make the exact flow profile in this region suspect, it does not mean that an overall dominance of CSF flow would not be noticed. In the present case velocities were relatively high anterior to the SC and thus one would still be capable of delineating flow dominance on one side of the SC or another.

The differences in velocity profiles and peak velocities between the 4D PC MRI measurements and CFD simulations suggest that the level of anatomical detail in CFD simulations are not adequate to accurately model the CSF dynamics in the cervical spine. The differences in anterior versus posterior flow in the 4D PC MRI measurements appear to be important in the overall flow field. However, the CFD did not capture the level of anterior flow dominance. Thus, SC nerve roots, denticulate ligaments and/or

other small anatomical structures such as the arachnoid trabeculae may be required to accurately model the flow field. It is yet clear if all or just some of these anatomical structures need to be included.

Various researchers have completed computational studies including different aspects of small structures in the SSS (see Table 2.1). Nevertheless, none of these studies have included all of the anatomical fine structures in their computational model, including the subject-specific geometries and flow boundary conditions and compared their simulation results with 4D PC MRI or 2D phase-contrast MRI measurements. Neglecting anatomical details makes the CFD simulations simpler and require less computing time ; however it may not be representative of the *in vivo* flow field.

While the present study did not include the small structures in the CFD simulations, it did compare directly the CFD results with the *in vivo* 4D MR measurements in healthy subjects and CM patients. One reason for the lack of comparison in the literature is that the 2D phase contrast MRI images are generally obtained with a slice thickness greater than the nerve root dimensions thus washing out some of the spatial flow complexity. Therefore, the single direction of velocity encoding does not permit quantification of the more complex flow phenomena that might arise near fine structures. Additionally, fine structures within the SSS are difficult to be captured with the current imaging techniques. Sigmund et al.¹⁰⁹ recently utilized 7T MRI with a custom designed neck coil to obtain high-resolution anatomical images of the cervical SSS with as low as 180 micron isotropic resolution. This resolution has potential to geometrically define nerve roots and denticulate ligaments but not arachnoid trabeculae.

Importance of tissue motion

Tissue motion appeared to relate with CSF dynamics near the FM. It appeared that differences between C1 and C2M level CSF flows and stroke volumes could be related to tissue motion of the brain (Figure 2.7). In particular, greater changes in CSF stroke volume were present near the FM in subjects with greater brain tissue motion. It can be hypothesized that abnormally elevated brain tissue motion in CM patients could result in movement of CSF by displacement. However, more patients and healthy subjects would need to be analysed to validate this hypothesis. Cousins et al.¹¹⁰ measured tonsillar motion with CINE MR imaging in patients suspected to have CM and subjects without any tonsillar ectopia. They found that patients and subjects with normal cerebellar tonsils both depicted a small-amplitude tonsil movement in cephalad and caudal directions during the cardiac cycle.

Limitations

There were a number of limitations in this study in terms of: 1) study population, 2) 4D PC MRI flow imaging methods and 3) CFD methodology. The primary aim of the study was to compare quantification of CSF dynamics by 4D PC MRI and CFD under a variety of CSF flow situations. Thus, a limited study population was selected to encompass both healthy subjects and CM patients that depicted a variety of CSF flow patterns. We chose four CM patients with differences in flow alterations, severity of tonsillar herniation and symptoms. The healthy subjects were considerably older than the CM patients and thus were also likely to have different flow characteristics^{86, 111}. In addition, several factors were not controlled including neck angulation that might have had an impact on CSF dynamics¹¹²⁻¹¹⁵. Future studies should be performed in a larger population with age-matched controls. It would also be useful to conduct repeatability studies.

The 4D PC MRI methods presented a number of important limitations. Slow moving CSF velocities were difficult to obtain due to inherent lack of signal and/or noise in the 4D PC MRI and relatively high velocity encoding values needed. This was particularly in the case of CM patients where flow jets were present within the ROI near FM and C1 level. The 4D PC MRI post-processing tool had limited ability for ROI selection and made it difficult to define complex geometries such as near the FM. At the FM avoidance of high arterial blood flow velocities from the vertebral arteries was difficult and altered the ROI. Future

improvements in the 4D PC MRI post processing could be achieved by a more robust pixel selection technique such as a point-by-point selection that incorporates spectral analysis and/or cross-correlation of pixel velocities.

To define the geometric region used for the CFD simulation we utilized an MRI scan with a spatial resolution of approximately 1 mm. This scan provides limited details about the fine anatomy that appeared to be an important factor in our study. It would be helpful to utilize images of higher resolution to define the geometric boundaries such as those that can be obtained with 7T MRI. Flow boundary conditions for the CFD model were difficult to define due to differences in CSF flow amplitude. A more accurate CFD simulation of the cervical CSF might incorporate the fluid structure interaction of the spinal cord, dura and other structures. It may also be required to incorporate moving boundary methods to model the tonsil and/or spinal cord motion in CM patients. Similar to previous studies in the literature, we set the pressure boundary condition to zero at the flow outlet. However, at this region there was at times bifurcating and/or complex flow outlet geometry. It is expected that the *in vivo* pressure could be different for the outlets and thus would impact CSF flow velocities. Even with these alterations in flow, we do not expect them to propagate further down the spine where the pressure around the spinal cord would likely be relatively uniform.

Overall, this study represents the first comparison of 4D PC MRI measurements and CFD simulation of CSF motion in the cervical SSS for healthy subjects and CM patients. CSF dynamics were found to be considerably different in 4D PC MRI versus CFD simulations. We believe the deviation of CFD results from the 4D PC MRI measurements is likely due to neglect of small anatomical structures in the cervical SSS and tissue movement. Thus, the present anatomically simplified rigid wall CFD methods likely need to be improved to accurately model CSF dynamics in the cervical SSS in terms of peak flow velocities and velocity profiles. Further analysis, such as incorporation of the spinal cord nerve roots and/or denticulate ligaments and an *in vitro* study, should be conducted to understand the differences in flow fields between the two methods. The results of our study also highlight the utility of CFD in conjunction with 4D PC MRI for detailed analysis of CSF flow dynamics that could help distinguish physiological from complex pathological flow patterns at the FM and cervical SSS. However, a full understanding of why pulsatile motion of the CSF is needed to maintain craniospinal health remains enigmatic. We expect that a combination of 4D PC MRI measurements and CFD simulations will be key tools to help assess and understand the CSF dynamics in health and disease states.

3. Inter-Operator Dependence of Magnetic Resonance Image-Based Computational Fluid Dynamics Prediction of Cerebrospinal Fluid Motion in the Cervical Spine

Theresia I. Yiallourou¹, Soroush Heidari Pahlavian^{2,3}, Francis Loth^{2,3}, Nicholas Shaffer^{2,3}, Alexander C. Bunck^{4,5}, Daniel B. Sheffer⁶, Jan Robert Kröger^{4,5}, Nikolaos Stergiopoulos¹, Bryn A. Martin^{2,3}

¹Laboratory of Hemodynamics and Cardiovascular Technology,
École Polytechnique Fédérale de Lausanne, Switzerland

²Department of Mechanical Engineering, University of Akron, OH, U.S.A

³Conquer Chiari Research Center, University of Akron, OH, U.S.A.

⁴Department of Radiology, University Hospital of Cologne, Germany

⁵Department of Clinical Radiology, University of Muenster, Germany

⁶Department of Biomedical Engineering, University of Akron, OH, U.S.A

3.1 Abstract

This study represents the first analysis of inter-operator dependence of magnetic resonance image (MRI) based computational fluid dynamics (CFD) modeling of cerebrospinal fluid (CSF) motion in the cervical spinal subarachnoid space (SSS). Time-resolved 3D velocity encoded phase-contrast MRI (4D PCMRI) flow measurements and T2-weighted anatomy MRI images were obtained at the cervical-medullary junction of a single healthy volunteer. 3D anatomy of the cervical SSS was reconstructed by manual segmentation by seven independent operators. CFD simulations considered the geometry to be rigid-walled with the CSF modeled as an incompressible Newtonian fluid. CFD results were compared at nine axial locations along the SSS in terms of eight hydrodynamic and geometric parameters: cross-sectional area, hydraulic diameter, peak systolic and diastolic velocities, pressure gradient, integrated longitudinal impedance, Reynolds and Womersley numbers. Intraclass correlation (ICC) was computed to assess the inter-operator agreement for each parameter over the axial locations and coefficient of variation (CV) was used to compare the percentage of variance for each parameter between the operators at each axial location. ICC between the operators was greater than 0.88 for all parameters analyzed with the exception of Reynolds number (ICC = 0.74). Peak systolic velocity was the parameter with greatest variance (CV=19%) while hydraulic diameter, cross-sectional area and Reynolds number had the least variance (CV~3.5%) between the operators. These results show a high degree of reliability for MRI-based CFD simulations in the prediction of CSF hydrodynamic and geometric-based parameters in the cervical spine of a healthy subject.

Key words

Cerebrospinal fluid (CSF), computational fluid dynamics (CFD), magnetic resonance imaging (MRI), Chiari malformation, neurohydrodynamics

3.2 Introduction

Abnormal cerebrospinal fluid (CSF) dynamics can result in devastating neurologic disorders that occur in much of the population such as hydrocephalus (1 in 2000 births⁶), Chiari malformation (1 in 3000¹¹⁶) and syringomyelia (1 in 8000¹¹⁶). Investigators have begun to research the link of CSF dynamics and disease states in terms of objective parameters such as CSF velocities⁸, integrated flow waveforms^{48, 117}, and bi-directional flow jets^{9, 10}. A powerful way to help understand the possible link of CSF dynamics and disease is the combined usage of computational fluid dynamics (CFD) based on subject-specific medical imaging of *in vivo* geometry and flow¹¹. This methodology has been used extensively in vascular hemodynamics and is attractive because it can provide subject-specific non-invasive information about disease states.

While the field of CSF dynamics has been investigated invasively for more than a century¹¹⁸, usage of MRI has enabled huge advances in recent years. Approximately 25 ml of CSF is contained within the spinal subarachnoid space (SSS)¹¹⁹ where it moves in a pulsatile manner synchronous with each cardiac cycle around the spinal cord,^{43, 79} with a peak Reynolds number of 300-400¹²⁰ and Womersley number ranging from 5 to 17⁴³. MRI measurements have shown that the volumetric CSF pulsation that moves in and out of the intracranial space is approximately one milliliter with nearly zero net flow^{49, 121} and has a peak systolic flow velocity ranging from 1-5 cm/s in healthy subjects⁶³. While the CSF pulsation to the SSS is small, many craniospinal pathologies have been associated with abnormalities in the CSF flow dynamics^{9, 10, 16, 122}. 2D phase-contrast magnetic resonance imaging (2D PCMRI) has been the mainstay for *in vivo* analysis of CSF flow dynamics. Recent studies have also used time-resolved 3D velocity encoded phase-contrast MRI (4D PCMRI) to assess 3D CSF flow field complexities, such as bisynchronous flow jets and vortices^{8, 63}.

To further understand the importance of CSF flow, CFD^{75-78, 88, 89, 123, 124} and *in vitro* bench-top experiments⁸⁴ have been used to investigate CSF flow and quantify parameters that can be difficult to measure or lack sufficient detail when acquired by MRI, such as pressure⁷⁰. These experimental and computational methods also enable variational analysis and application of reductionism that cannot be applied *in vivo*, for example reductionism to determine impact of anatomical features on CSF flow, such as spinal cord nerve roots and denticulate ligaments¹²⁰. In addition, they can be used to identify new quantitative parameters to assess disease states; for example, application of CFD in the cervical spine for Chiari malformation patients showed elevated impedance to CSF flow compared to controls^{64, 125}.

Uncertainty in model geometry impacts the reliability of CFD-based prediction of CSF flow. To date, all of the CFD studies of CSF flow have relied on a single operator segmentation of the CSF space. Analysis of inter-operator dependence of CFD results has been an important part of CFD investigation of vascular hemodynamics^{11, 126-129}. Long et al.¹²⁹ conducted a reproducibility study of MRI-based CFD modeling in the carotid bifurcation of human volunteers scanned twice using the same MRI protocol. Results were compared in terms of contour shape factors, cross-sectional area and mean radius difference and showed that the vessel was well reproduced. In a subsequent study¹²⁶, the authors analyzed the impact of the above geometric differences on CFD predicted flow patterns and wall shear stress; a parameter thought to be associated with atherosclerosis development. They observed wall shear stress to be sensitive to variations in local geometry and computational mesh design. Glor et al.¹²⁷ studied the dependence of 3D ultrasound measurement-based CFD modeling of blood flow in a carotid bifurcation based on images acquired by four ultrasound technicians and subsequently segmented by two operators. It was shown that parameter variability, such as cross-sectional area and wall shear stress (8% and 0.19 Pa, respectively), was impacted more due to the ultrasound technician than the image-processing operator.

While CFD requires validation to ensure accuracy^{120, 130}, the combined usage of MR imaging and CFD is a useful approach to investigate CSF flow. However, analysis of inter-operator dependence of MRI-based CFD results for CSF flow in the upper cervical spine has not yet been completed. To analyze this dependence, our approach was to conduct seven CFD simulations based on geometries that were manually segmented by seven independent operators for a single healthy subject MRI data set. Inter-

operator agreement of the CFD results was assessed in terms of eight geometric and hydrodynamic parameters quantified at nine axial planes along the spine.

3.3 Materials and Methods

Ethics statement

The MR data acquisition was performed at the Department of Radiology of Münster. The study was approved by the institutional review board of the University of Münster. Before the MR exams were conducted, written informed consent was obtained from the healthy volunteer. MR images were anonymized prior to data processing.

3.3.1 4D PC MRI data acquisition

The CFD models were based on subject-specific 4D PCMRI measurements in the cervical spine of a healthy subject (22-years-old) with no history of neurological disorder or spinal trauma, who is referred as HVb in the previously published study of our group . All images were acquired on a 1.5 T MRI scanner (Achieva 2.6 scanner, Philips, Best, The Netherlands). In brief, a high-resolution T2-weighted 3D, turbo spin-echo sequence (VISTA) with an isotropic spatial resolution of 0.8 mm defined the cervical spinal geometry for the CFD simulations. To define the flow boundary conditions for the CFD model, 4D PCMRI measurements were acquired with a standard 16-channel head and neck coil using the sequence parameters as described in the protocol by Bunck et al.⁶³.

3.3.2 Three-dimensional reconstruction and mesh generation

3D anatomy of the cervical SSS, including the dura mater and spinal cord, was reconstructed by seven operators (Op.1-7) based on the same set of T2-weighted MRI images. Manual segmentation was completed using ITK Snap software (Version 2.2.0, PA, U.S.A.). See Figure 3.1 for a segmentation example. Three of the seven operators were experienced with the process of manual segmentation of the SSS. The remaining four had never before segmented the SSS.

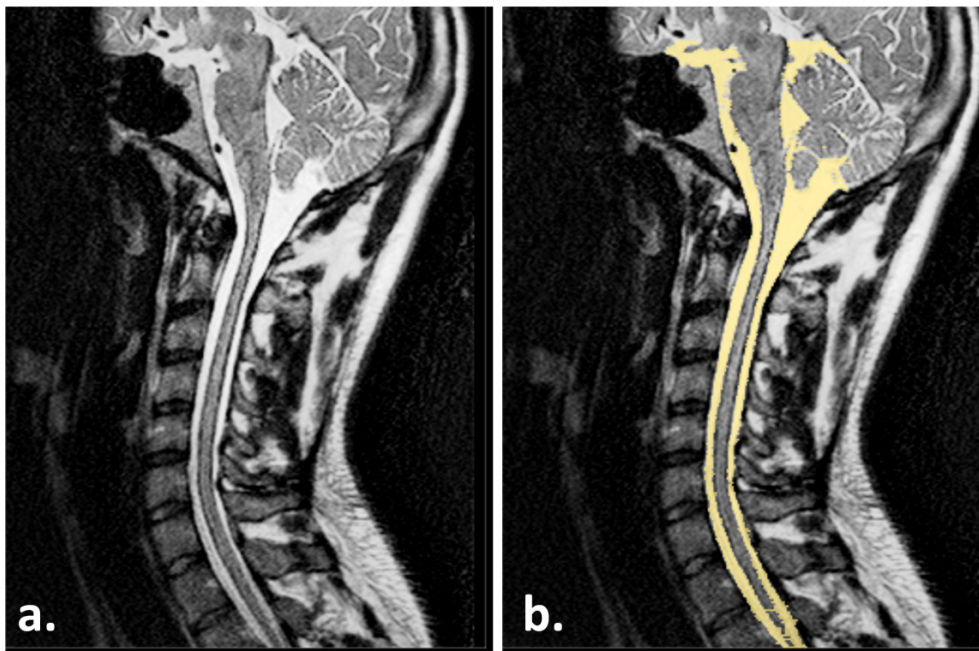


Figure 3.1. **a)** T2 weighted MRI image of the cervical spine for the healthy volunteer. **b)** Example of manual segmentation of the SSS from the T2-weighted MRI for one operator.

The caudal end of each model was segmented approximately 5 cm below C7 to prohibit entrance length effects within the region analyzed. Vertebral arteries were included in the model near the foramen magnum. Other fine structures such as spinal cord nerve roots, blood vessels, and denticulate ligaments were not included in the segmentations. After segmentation, each 3D geometry (Figure 3.2) was smoothed with the Laplacian smoothing algorithm within MeshLab software (Version 1.3.0, Italy, Rome). The 3D geometries were then imported into ANSYS ICEM CFD software (Version 13.0, Canonsburg, PA) and rigid wall unstructured computational grids were generated by a single operator consisting of approximately 2 million tetrahedral elements.

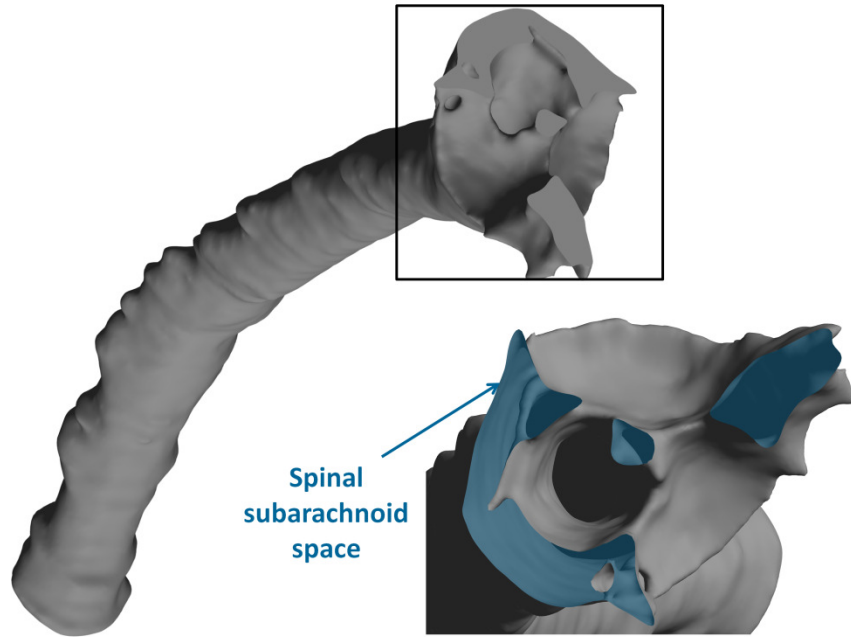


Figure 3.2. Three-dimensional CFD model of the cervical spinal canal built from manual segmentation (left). Zoom of the upper cervical spine (right) showing the region of space (blue) where the CSF flows.

3.3.2 CFD simulations

The same CSF flow waveform was chosen as the inlet flow boundary condition for all simulations and was based on the C3 level CSF flow measurement for HVb in Yiallourou et al.¹³⁰ (Figure 3.3). The flow waveform was imposed as a blunt CSF velocity profile at the caudal end of the geometry. A no-slip boundary condition was specified at the walls with a zero pressure boundary condition imposed at the model outlet (cranial end)^{68, 105}. The CFD simulation was completed using ANSYS CFX (Version 13.0, Canonsburg, PA) with CSF modeled as an incompressible Newtonian fluid with the fluid properties of water (density of $\rho=1000\text{kg/m}^3$ and dynamic viscosity of $\mu=0.001\text{Pa.s}$) at body temperature^{106, 107}.

Flow was assumed to be laminar. Within the CFX solver settings, second order accuracy advection scheme was implemented to solve the Navier-Stokes equations by the use of Gauss' Divergence Theorem. The time-step size was chosen to be $T/100$, where T represents the period of CSF flow cycle ($T=0.78\text{s}$). The utilized transient time-stepping scheme was second order implicit backward Euler. The root-mean square residual (RMS) was set to 10^{-4} as a convergence criterion. The total duration time for the completion of each CFD simulation to reach convergence was approximately 5 hours when ran in parallel on a computer with 8 processing cores and 12-GB RAM. Grid and time independence was demonstrated for the above methods in an earlier study for the same geometry and CFD settings¹³⁰. Results were analyzed for the third cycle after convergence was reached.

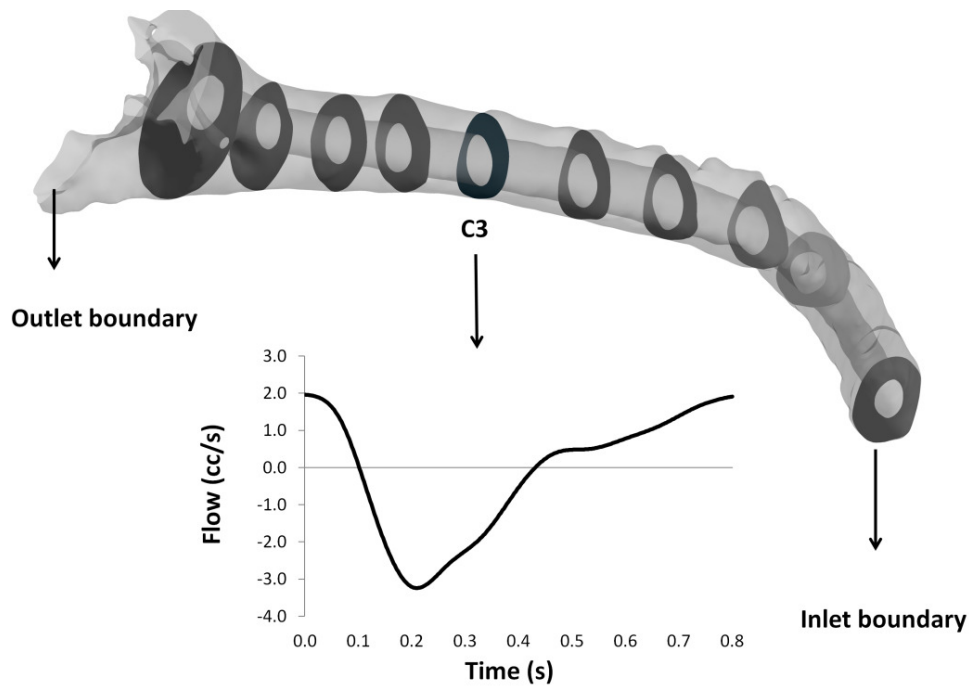


Figure 3.3 Axial orientation of the nine planes for one of the CFD models that are placed orthogonally to the direction of CSF flow (top). Zero pressure was set at the outlet cranial boundary. The CSF flow rate that was based on the *in vivo* PCMRI measurements at C3, was imposed at the model inlet boundary for all simulations.

3.3.3 Data processing

CFD results were analysed using ANSYS CFD-post (Version 13.0, Canonsburg, PA). Nine axial planes (from foramen magnum (FM) to C7 vertebral level) were placed along the CFD models orthogonal to the primary CSF flow direction (Figure 3.3). For each location, thru-plane peak systolic velocity profiles were visualized for the seven CFD models. The following geometric and hydrodynamic parameters were quantified for each axial location:

a) *Geometric parameters*: Cross-sectional area, A_{CS} , and hydraulic diameter D_h , based on the wetted perimeter, P_{WET} and A_{CS} was calculated according to equation:

$$D_h = \frac{4 A_{CS}}{P_{WET}}$$

b) *Peak thru-plane CSF velocities*: peak systolic, V_{sys} (caudal) and diastolic V_{dia} (cranial) flow velocities.

c) *Reynolds number*: Reynolds number, Re , based on hydraulic diameter, D_h , and V_{sys} was quantified by the following equation to help validate the assumption of laminar flow for the CFD model.

$$Re = \frac{\rho D_h V_{sys}}{\mu}$$

where ρ is the density of CSF ($\rho=1000\text{kg/m}^3$) and μ refers to the dynamic viscosity of CSF ($\mu=0.001\text{Pa.s}$)

d) *Womersley number*: Womersley number, a , was computed by the following equation in order to define the importance of inertia on the flow field.

$$a = \frac{D_h}{4} * \sqrt{\frac{\omega}{\nu}}$$

where ω is the angular velocity ($\omega=2*\pi/T$) of the volume flow waveform and ν is the kinematic viscosity of CSF ($\nu=\mu/\rho$).

e) *Pressure gradient*: The unsteady pressure gradient, $\Delta P(t)$, was calculated over each spine segment (e.g. FM-C1). In addition, the pressure gradient over the entire model from FM to C7 was obtained. Peak pressure gradient magnitude within each spine segment was also quantified.

f) *Integrated longitudinal impedance*: Longitudinal impedance, or the unsteady flow resistance, was calculated as the ratio of Fourier coefficients of the pressure gradient, $F(\Delta P(t))$ and the input flow waveform, $F(Q(t))$ at each harmonic¹³¹. The impedance modulus Z_L was calculated for each frequency according to the following equation :

$$Z_L = \left| \frac{F(\Delta P(t))}{F(Q(t))} \right|$$

The resulting curves for Z_L (in dyn-s/cm⁵) for each harmonic were then integrated from 1–8 Hz to obtain the integrated longitudinal impedance (ILI), for each of the spine segments (e.g. FM-C1) in all seven CFD simulations.

3.3.4 Statistical analysis

Mean±standard deviation (SD) of each parameter for the seven operators was calculated. Statistical analysis was conducted with Minitab 16 (State College, PA) and Excel (Microsoft Office 2007, WA). Analysis of variances (ANOVA) was used to estimate the level of inter-operator agreement for each parameter over all locations analyzed by computing the intraclass correlation coefficient (ICC) with a confidence interval of 95%. Coefficient of variation (CV) was used to quantify the parameter variability between the seven operators at each of the measurement locations.

3.4 Results

3.4.1 Geometric parameters

Comparison of geometric parameters between the operators showed a high level of agreement in mean and SD over the entire cervical spine (Figure 3.4, Table 3.1).

Table 3.1. Summary of the calculated geometric and hydrodynamic parameters for all seven CFD simulations (Values are given as mean ±SD)

Axial level	D _h (cm)	A _{cs} (cm ²)	V _{sys} (cm/s)	V _{dia} (cm/s)	Reynolds number	Womersley number
FM	1.7±0.05	5.9±0.2	-0.9±0.05	0.6±0.04	144±7.2	11.9±0.4
C1	1.1±0.06	2.6±0.2	-1.9±0.2	1.3±0.1	203±8.8	7.8±0.5
C2M	0.9±0.05	2.1±0.1	-1.8±0.1	1.2±0.1	170±2.8	6.7±0.4
C2P	0.8±0.05	1.9±0.1	-2.5±0.2	1.7±0.1	209±4.7	5.9±0.4
C3	0.7±0.05	1.4±0.1	-2.8±0.3	1.9±0.2	182±5.0	4.8±0.4
C4	0.6±0.04	1.4±0.1	-2.8±0.3	2.0±0.2	173±4.9	4.4±0.3
C5	0.6±0.05	1.3±0.1	-3.1±0.4	2.2±0.2	178±5.5	4.1±0.4
C6	0.6±0.04	1.2±0.1	-3.7±0.7	2.6±0.5	212±28.7	4.1±0.3
C7	0.7±0.03	1.3±0.1	-2.9±0.2	2.0±0.1	191±12.2	4.7±0.3

Abbreviations: D_h = hydraulic diameter, A_{cs} = cross-sectional area, V_{sys} = peak systolic velocity, V_{dia} = peak diastolic velocity, SD = standard deviation.

In general, parameters had better agreement near the FM (Table 3.2). Dh and Acs had the greatest and smallest CV between operators at C5 (~10%) and FM (~4%), respectively (Table 3.2). ICC for Dh and Acs was greater than 0.98.

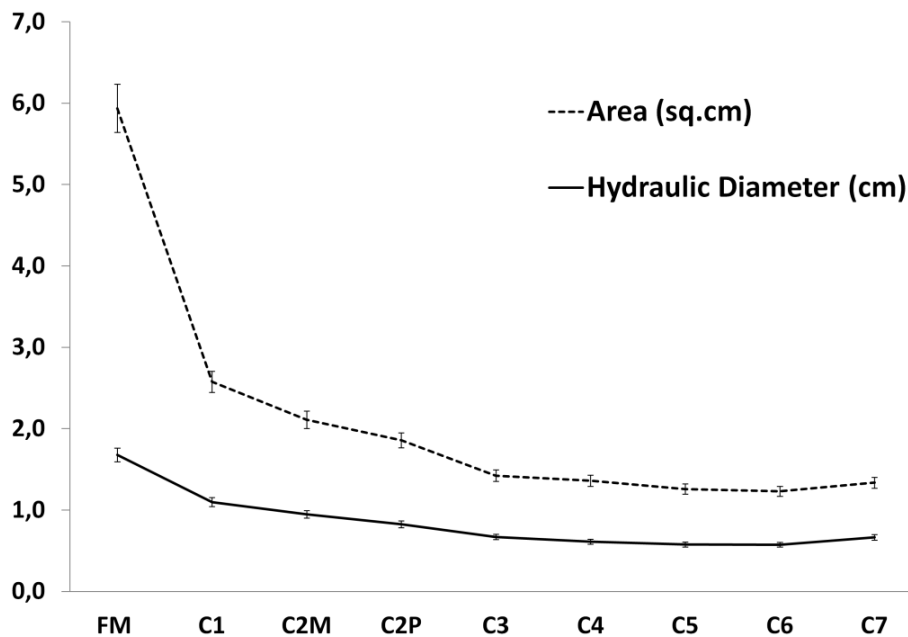


Figure 3.4. Mean values and standard deviations of the hydraulic diameters, D_h , and cross-sectional areas, A_{cs} computed at each axial plane of the cervical SSS for the seven operators (FM = foramen magnum, C2M = middle of 2nd cervical vertebra, C2P = junction of C2/C3 vertebra).

Table 3.2. ICC and CV given as maximum and minimum percent at the corresponding location for the seven operators

Parameter	Min CV (axial location)	Max CV (axial location)	ICC (95% CI.)
D_h	3.6% (FM)	9.6% (C5)	0.98 (0.98-1.00)
A_{cs}	3.8% (FM)	11.2% (C5)	0.99 (0.99-1.00)
V_{sys}	5.1% (C2M)	19% (C6)	0.88 (0.73-0.98)
V_{dia}	4.5% (C2P)	17.3% (C6)	0.90 (0.79-0.98)
Re	1.8% (C2P)	14.6% (C6)	0.74 (0.45-0.93)
a	3.6% (FM)	9.6% (C5)	0.98 (0.97-1.00)
ΔP	5.3% (FM-C1)	11.6% (C6-C7)	0.99 (0.97-1.00)
ILI	8.8% (C3-C4)	18.5% (C6-C7)	0.99 (0.98-1.00)

Abbreviations: ICC=intraclass operator variability, CI=confidence interval, CV=coefficient of variation, D_h = hydraulic diameter, A_{cs} = cross-sectional area, V_{sys} = peak systolic velocity, V_{dia} = peak diastolic velocity, Re= Reynolds number, a =Womersley number, ΔP = pressure gradient, ILI = integrated longitudinal impedance

3.4.2 Hydrodynamics parameters

Quantification of hydrodynamic parameters computed from CFD, such as V_{sys} , V_{dia} , a , and ΔP , for each operator depicted a strong agreement with a minimum ICC of 0.88, excluding Reynolds number, Re , with an ICC of 0.74 (Table 3.2). Overall, hydrodynamic parameters had the smallest CV within the FM to C2P level. Similar to geometric parameters, the agreement of V_{sys} and V_{dia} between the operators decreased along the spine towards the feet with a maximum CV of ~18% at C6 (Figure 3.5, Table 3.2). This location also had the maximum V_{sys} and V_{dia} (Table 3.1). Maximum value of Reynolds number occurred at C6 and with a CV of 14.6%. A maximum CV of 9.6% for Womersley number, a , occurred at C5.

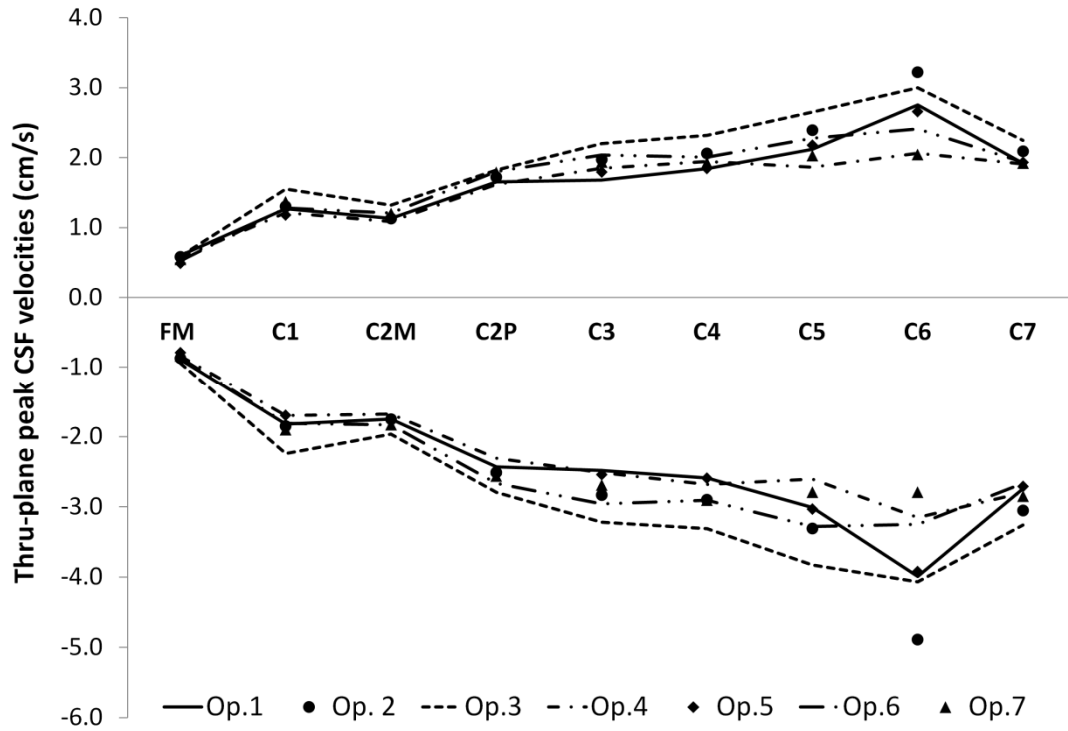


Figure 3.5. Peak systolic, V_{sys} , and diastolic, V_{dia} , velocities obtained from the seven CFD simulations based on each operator (Op.1 to Op.7). Positive (diastolic) and negative (systolic) velocities reflect head and foot directed flow, respectively.

Unsteady pressure gradient measured between FM to C7 showed similar trend in waveform shape and magnitude for each of the operators (Figure 3.6). The agreement of waveform shape was expected considering that the CSF flow input was identical for each model and model geometric differences were small. Peak pressure gradient, ΔP , over the cardiac cycle increased along the spine (Table 3.3). ΔP within the C6-C7 segment had the greatest CV between the operators (11.6%), while the FM-C1 segment had the least CV (5.3%) (Table 3.2). Similar to ΔP , the greatest ILI CV occurred at the C6-C7 segment (18.5%).

Based on qualitative inspection, CFD-computed velocity profiles for the seven operators were similar in terms of distribution around the spinal cord (anterior versus posterior) and location of peak velocities (Figure 3.7). Differences in velocity profiles were most noticeable from C3 to C7. Velocity profiles from FM to C2M were nearly identical. Velocity profiles were skewed to the narrower posterior and anterolateral SSS in all operators in a number of planes (C2P-C7).

Table 3.2. Mean values of peak pressure gradient and integrated longitudinal impedance for all seven CFD simulations (Mean \pm SD)

Spine Segment	Peak ΔP (Pa)	ILI (dyn/cm ⁵)
FM-C1	1.9 \pm 0.1	90 \pm 8
C1-C2M	3.1 \pm 0.2	145 \pm 19
C2M-C2P	3.1 \pm 0.2	164 \pm 20
C2P-C3	5.3 \pm 0.4	235 \pm 25
C3-C4	8.0 \pm 0.7	317 \pm 28
C4-C5	6.9 \pm 0.7	265 \pm 33
C5-C6	8.1 \pm 0.8	320 \pm 33
C6-C7	7.4 \pm 0.9	311 \pm 58
<i>Total</i>	<i>43.8\pm3.5</i>	<i>1847\pm177.2</i>

Abbreviations: ΔP = pressure gradient, ILI = integrated longitudinal impedance, SD = standard deviation

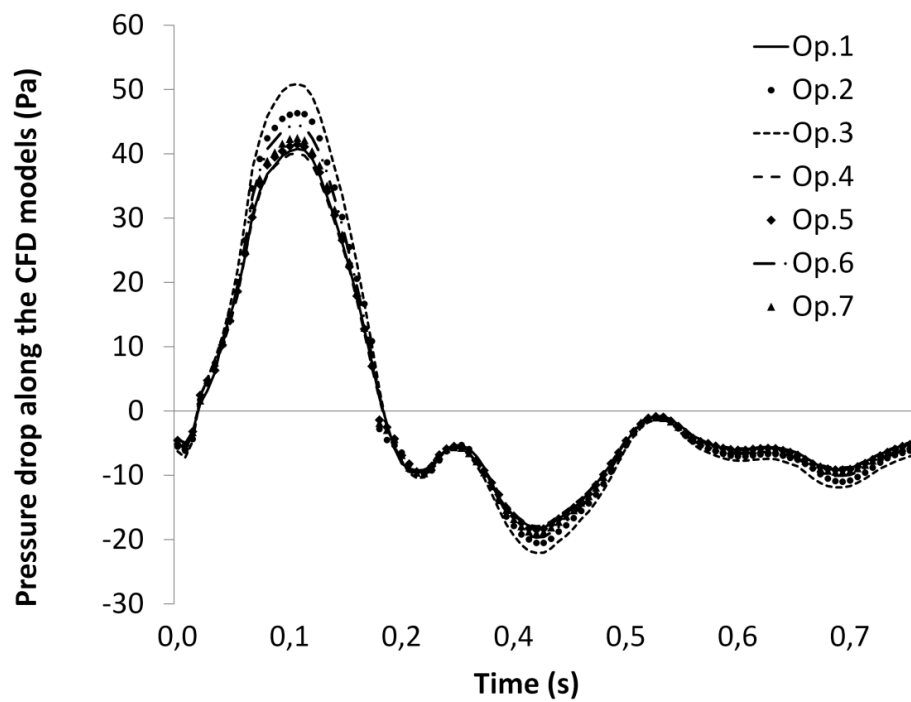


Figure 3.6. Unsteady pressure gradient waveform computed between the FM and C7 for each CFD simulation from the seven operators (Op.1 to Op.7).

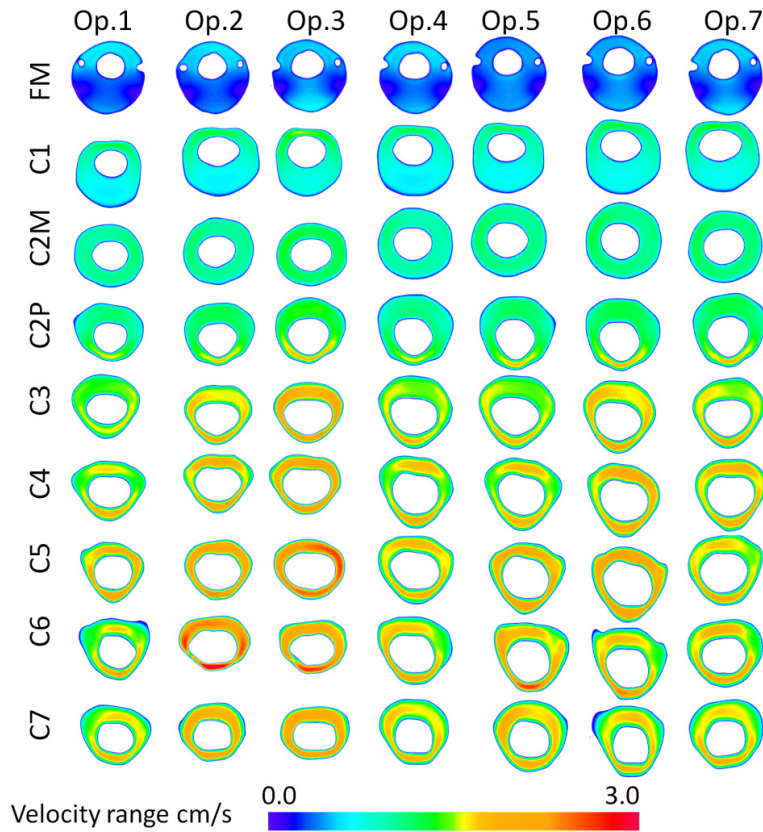


Figure 3.7. Thru-plane peak systolic velocity profiles at nine axial locations along the cervical spine for the geometries segmented by the seven operators (Op.1-Op.7).

3.5 Discussion

This study shows that the combined usage of MRI measurement of SSS geometry and CFD modelling can provide a consistent geometric and hydrodynamic description of the CSF spaces in the cervical spine. Our approach was to compare CFD-based geometric and hydrodynamic parameters that result from a manually segmented model of the cervical spine created by seven independent operators. The same CSF flow boundary condition was used for the seven simulations, thus differences in CFD results would only be due to geometric variations between the operators. The quantified geometric and hydrodynamic parameters showed a high level of ICC agreement, greater than 0.90 with a confidence interval of 95% between the operators (excluding Reynolds number with ICC=0.74). Parameters assessed in the lower cervical spine (C5-C7) had greater variability than the upper, with a maximum CV of ~20% for all parameters analysed. Results showed less variability in the upper cervical spine (FM to C2P), with a maximum CV of ~5% for all parameters analysed.

The overall objective of the present study was to identify CSF dynamics based parameters that are indicative of disease states. At present, CSF dynamics have been carefully described in healthy controls versus patients with Chiari malformation and alterations in patients that occur pre- and post-surgery. Thus, discussion focuses on parameter variability in the present study compared to variability of the same parameters previously reported in Chiari malformation patients and controls. Also, when possible, parameter variability is considered for Chiari malformation patients pre and post-spinal decompression surgery. Ideally, a parameter's variability should be significantly less than the sensitivity required for diagnosis/detection of the disease state and analysis of surgical treatment.

Importance of geometric parameters

Geometric assessment of the cervical-medullary junction has been a mainstay for morphometric analysis studies of Chiari malformation and syringomyelia^{131, 132}. At present, these studies have focused on 1D assessment of features in the mid-sagittal plane and thus provide a limited view of the 3D geometry presented by the spinal cord, medulla, cerebellar tonsils and dura mater. It is expected that future work

will increasingly include 3D analysis of the SSS and thus, quantification of the inter-operator geometric variability of manual segmentation of the SSS is crucial.

The seven operators provided consistent geometric reconstruction of the CSF space with an ICC greater than 0.95 and maximum CV of 11% (Table 3.2) for D_h and A_{cs} (Figure 3.4, Table 3.1). This level of consistency was found even while four of the seven operators had never before segmented the SSS prior to this study. The FM axial location had the lowest CV in both parameters, indicating that this region is more consistently segmented. CV increased further down the cervical spine showing that this region was more difficult to segment consistently.

The present study results show that operator dependence of D_h and A_{cs} is likely not an important factor when differentiating patients from controls, but may be important to detect changes in geometry due to surgery. A study by Bunck et al.⁸ documented that A_{cs} in healthy controls ($n=10$) was ~ 400 and $\sim 200\%$ greater than Chiari malformation patients ($n=20$) at the foramen magnum and C1, respectively ($p<0.001$). Similar magnitude of differences between the Chiari patient population and controls was quantified by others¹³⁰. In another study, average D_h near the cervical-medullary junction was more than 200% greater in a healthy subject compared to two Chiari patients pre-spinal decompression surgery. For that study, average D_h and A_{cs} was found to increase by only 10 to 50% post spinal decompression surgery ($n=2$). It should be noted that these differences were computed for the average D_h and A_{cs} over a 2.5 cm region below the FM, thus any particular axial slice location could have a much greater difference. Also, these considerations are based on *in vivo* studies with few subjects and should be examined in a larger population.

Importance of hydrodynamic parameters

Elevated peak CSF velocities have often been found near the FM in Chiari malformation^{8, 9, 16, 130}. Researchers have hypothesized that the elevated CSF velocities are due to FM obstruction (stenosis) by the cerebellar tonsils. However, the *in vivo* PCMRI measurements used to show the velocity differences lack detail about the full CSF flow field complexity. Subject-specific CFD has been applied as a tool to understand CSF dynamics in greater detail and as a potential means for disease assessment. As such, it is necessary to understand the variability of peak CSF velocities due to geometric reconstruction from different operators.

Similar to geometry, the present study results show that operator dependence of V_{sys} and V_{dia} is likely not an important factor to differentiate patients from controls, but may be important to detect changes in velocity due to surgery. V_{sys} and V_{dia} showed slightly less agreement (ICC >0.88 , Table 3.2) than the geometric parameters. Peak velocities had small variance for the axial locations analyzed and had a maximum difference lower in the cervical spine (CV at C6 was $<19\%$). The greater variance of velocity lower in the spine can be attributed to an increase in D_h and A_{cs} variance within that region and vice versa. Several *in vivo* studies in the literature have shown peak CSF velocities to be ~ 200 to 300% greater in Chiari patients than controls^{8, 9, 16, 130}. In a study to quantify peak CSF velocity alterations pre- and post-decompression surgery, peak velocity decreased by $\sim 30\%$ ($n=8$, $p=0.01$)¹³³.

Qualitative comparison of the thru-plane CSF velocity profiles at peak systole showed similar flow patterns for all operators (Figure 3.7). All simulations showed profile skewing at some axial locations to the posterior and anterior-lateral SSS. As expected, peak velocities were inversely related with A_{cs} and D_h and locations with greater variance in A_{cs} and D_h had greater differences in velocity profiles (e.g. at C6).

A great deal of evidence points towards the role of abnormal pressure gradients in CSF system pathologies. Pressure differences (dissociation) within the CSF system, caused by the pulsatile intracranial blood flow and CSF motion, are complex in terms of magnitude and distribution⁷⁹ and, when abnormal, may damage tissue and result in pathologic conditions, such as in type I Chiari I malformation⁸⁵. *In vivo* measurements have found craniospinal pressure dissociation to be elevated in Chiari patients compared to controls, to decrease after surgery and associated with symptom improvement^{54, 56, 134}.

The results showed that ΔP reliability between the operators is likely sufficient to help detect Chiari patients versus controls, but not alterations in ΔP post-surgery. Unsteady pressure gradient, $\Delta P(t)$, between the FM and C7 showed strong agreement in terms of waveform magnitude and shape (Figure 3.6) and axial distribution (ICC=0.99, Table 3.2 and 3.3). ΔP variance showed a similar trend as D_h and A_{cs} with the greatest CV values lower in the cervical spine (C6-C7) and the smallest CV near the cervical-medullary junction (FM-C1). Peak ΔP in Chiari patients has been found in several CFD studies to be greater than controls by up to 200%^{131, 135}. Post surgery (n=2), ΔP was found to be variable ranging from ~10% increase to ~20% decrease¹³¹. The presented methodology required solving the full 3D Navier-Stokes equations to obtain pressure gradients in the flow field. It should be noted that viscous effects were insignificant with Womersley number ranging from 4 to 12 (Table 3.1) thus, it is expected that ΔP waveforms can be predicted by A_{cs} spatial integration of the linearized Navier-Stokes equations⁴³.

Unsteady resistance to CSF flow, ILI, was computed based on the inlet volume flow, $Q(t)$, measured from MRI, and the pressure gradient, $\Delta P(t)$, calculated from CFD for the axial sections of each model (e.g. pressure gradient between FM to C1)¹³¹. ILI is a hydrodynamic parameter that has been used to help objectively quantify CSF flow blockage inside the SSS for Chiari malformation patients. Similar to ΔP , ILI agreement was strong (ICC=0.99). ILI followed the same trend as the peak pressure gradient, with the greatest CV at the C6-C7 segment and the least variation at C3-C4. The ILI for the healthy subject in this study ranged from 175 to 303 dyn/cm⁵ (Table 3.2) a value similar to other studies in healthy subjects^{64, 120, 131}. Shaffer et al. found that ILI was more than 200% greater in Chiari patients than controls ($P<0.001$).

The analysis of Reynolds and Womersley number is presented to help understand the hydrodynamics. These parameters are not expected to related directly with disease states but rather are helpful to compare the present study results with the literature and validate the CFD methodology assumptions, such as laminar flow. Maximum Reynolds number for all simulations was ~250 and located at C6, the location where maximum V_{sys} and minimum D_h occurred. Thus, Reynolds number was lower than the critical value of transition to turbulence and agreed with studies in the literature^{120, 131}. Although one study noted possible transitional flow features¹²⁴. For all seven CFD models, Reynolds number was shown to increase with distance from the skull (Table 3.1). Womersley number, a , had a similar trend as D_h (Table 3.1) with the maximum and minimum value at the FM and C5/C6, respectively. Values of a found in this study are in the range reported in the literature^{43, 131} with inertial effects dominating the flow field, particularly in the upper cervical spine from FM to C1.

Limitations

Each operator segmented the geometry of a healthy volunteer that was scanned once on a single MRI machine. If the same subject was scanned in different MRI machines it is expected that different imaging parameters could have an impact on the reconstructed geometries. Also, scanning multiple times on different machines could introduce error due to alterations in neck angulation. These factors may have an important impact on geometry and should be analyzed, but were not the subject of the present study. It should also be noted that patients with craniospinal disorders, such as Chiari malformation, often have restricted CSF spaces, with smaller areas, and may be more difficult to segment the complex geometry. However, the smallest A_{cs} in the present study (1.2 cm² at C6, Table 3.1) was similar to that measured in Chiari patients in vivo (1.2 – 2.4 cm² at the FM¹³¹). Thus, we expect that the variance in geometric and hydrodynamic parameters observed in the present study would be of similar magnitude for Chiari patients at the FM.

Another limitation of the presented work was that the “gold standard” geometry was not available as a basis for assessment of geometric reconstruction accuracy. This could be assessed by conducting an in vitro study where the model geometry is known as in previous hemodynamics studies¹¹. However, an in vitro model is still limited because it does not have identical properties as human tissue. Another approach could be to utilize high resolution 7T MRI¹³⁶ to better define the geometric boundaries, however in this case the “gold standard” geometry would still not be known.

While CFD applied to model CSF flow has provided insight, it requires many simplifications to the complex in vivo anatomy. CFD studies of CSF flow in the cervical spine have been conducted under geometrically simplified^{43, 83, 91}, subject-specific 3D models without fine anatomical structures^{68, 69, 120, 124, 130, 137} and with idealized spinal cord nerve rootlets and denticulate ligaments¹²⁰. Spinal cord nerve rootlets and denticulate ligaments were not included in the modeling approach of the present study as these were not possible to quantify based on the MR images¹²⁰. Thus, some of the in vivo flow features observed by MRI, such as increased CSF flow velocities (jets) near nerve rootlets^{10, 130, 133} were not present in the models of this study. Our approach was to utilize the most commonly used CFD method for CSF flow modeling in order to determine the importance of different operators on the results in a trial to spot CSF dynamics-based parameters that are indicative of disease states. This approach included a geometry with rigid spinal cord and dura mater and subject-specific CSF flow boundary condition. However, this common CFD modeling perspective should be validated in greater detail to assure that it accurately reflects the in vivo CSF flow phenomenon.

All in all, this study represents the first analysis of inter-operator dependence of MRI-based CFD modeling of CSF movement in the cervical spine. The findings show that the CFD-based geometric and hydrodynamic parameters were little impacted by the operator that completed the image segmentation (mean ICC for the parameters analysed was 0.93). This agreement was found even when four of the seven operators had never before segmented the SSS. The maximum variance was 19% (CV) for all parameters analysed at every axial location along the cervical spine. Variability was greater in the lower cervical spine compared to the upper (CV at FM ~ 2-5%). When considered with respect to disease, the operator variability in the parameters analysed was small in comparison to the differences observed for the same parameters in Chiari patients compared to controls. These results support the use of subject-specific MR-based CFD modelling of CSF flow within the cervical spine to provide consistent quantitative geometric and hydrodynamic parameters for potential clinical diagnostic and assessment purposes.

4. The effect of continuous positive airway pressure on total cerebral blood flow in healthy awake volunteers

Theresia I. Yiallourou¹, Céline Odier², Raphael Heinzer³, Lorenz Hirt², Bryn A. Martin¹,
Nikolaos Stergiopoulos¹, José Haba-Rubio³

¹ Laboratory of Hemodynamics and Cardiovascular Technology,
École Polytechnique Fédérale de Lausanne, Switzerland

² Centre Hospitalier Universitaire Vaudois Lausanne (CHUV),
Neurosciences Department

³ CHUV, Center for Investigation and Research in Sleep (CIRS)

4.1 Abstract

Continuous positive airway pressure (CPAP) is the gold standard treatment for obstructive sleep apnea. However, the physiologic impact of CPAP on cerebral blood flow (CBF) is not well established. Ultrasound can be used to estimate CBF, but there is no widespread accepted protocol. We studied the physiologic influence of CPAP on CBF using a method integrating arterial diameter and flow velocity (FV) measurements obtained for each vessel supplying blood to the brain. FV and lumen diameter of the left and right internal carotid, vertebral, and middle cerebral arteries were measured using duplex Doppler ultrasound with and without CPAP at 15 cmH₂O, applied in a random order. Transcutaneous carbon dioxide (PtcCO₂), heart rate (HR), blood pressure (BP), and oxygen saturation were monitored. Results were compared with a theoretical prediction of CBF change based on the effect of partial pressure of carbon dioxide on CBF. Data were obtained from 23 healthy volunteers (mean±SD) (12 male, age 25.1±2.6years, body mass index 21.8±2.0kg/m²). The mean experimental and theoretical CBF decrease under CPAP was 12.5% (p<0.001) and 11.9% (p<0.001), respectively. The difference between experimental and theoretical CBF reduction was not statistically significant (3.84±79ml/min, p=0.40). There was a significant reduction in PtcCO₂ with CPAP (p=<0.001) and a significant increase in mean BP (p=0.0017). No significant change was observed in SaO₂ (p=0.21) and HR (p=0.62). Duplex Doppler ultrasound measurements of arterial diameter and FV allow for a noninvasive bedside estimation of CBF. CPAP at 15 cmH₂O significantly decreased CBF in healthy awake volunteers. This effect appeared to be mediated predominately through the hypocapnic vasoconstriction coinciding with PCO₂ level reduction. The results suggest that CPAP should be used cautiously in patients with unstable cerebral hemodynamics.

Keywords

Continuous positive airway pressure; cerebral blood flow; PCO₂; ultrasound

4.2 Introduction

Obstructive sleep apnea syndrome (OSAS) is characterized by repetitive episodes of upper airway obstruction during sleep and results in cessation (apneas) or reduction (hypopneas) in airflow which leads to awakening and the reduction of blood oxygen saturation (SaO₂). The most widely accepted treatment of OSAS is continuous positive airway pressure (CPAP). CPAP acts as a pneumatic “splint” by producing a positive pressure inside the airway thereby preventing upper airway collapse during sleep. Considering that a rise in intrathoracic pressure increases jugular venous pressure, CPAP could have an effect on cerebral blood flow (CBF) by reducing the cerebral perfusion pressure^{29, 57}. Moreover, decreased venous return due to increased intrathoracic pressure may decrease right (and left) filling pressure, which may in turn decrease cardiac output. CPAP use can also induce changes in partial pressure of carbon dioxide (PCO₂), which has a major impact on CBF, similar to the way in which hypocapnia constricts cerebral arteries and hypercapnia leads to a marked rise of CBF^{59, 60, 61}. Changes in CBF induced by CPAP may have important clinical implications in patients for whom an optimal CBF is mandatory, such as acute stroke patients.

Published data about the effects of CPAP on cerebral hemodynamics are conflicting^{26, 27, 58}. Various studies have reported an increase^{26, 138}, other a decrease^{58, 139} and some a no significant change²⁷ in CBF. The conflicting results may be due to inaccurate and/or insensitive CBF measurement methods. Furthermore, many of the studies that employed transcranial Doppler ultrasound (TCD) used only flow velocity (FV) and pulsatility index (PI) in the middle cerebral artery (MCA) to estimate total CBF^{26, 27, 58, 138, 139}. However, TCD measurements do not take into account changes in artery diameter or in cerebral posterior circulation. As a result, it is unclear whether changes in MCA FV accurately reflect total CBF change. A method that takes into account both blood FV and the artery diameter of all vessels supplying blood to the brain is likely to be more accurate. Furthermore, in the previous studies^{26, 27, 58} only end-tidal CO₂ level was monitored. This is an inaccurate measurement technique under the presence of CPAP considering that the expired CO₂ is diluted by incoming CO₂-free CPAP airflow.

The present study was performed to assess the effect of CPAP on total CBF measured by duplex color Doppler ultrasound (US) using a method, similar to that presented by Schoning et al.¹⁴⁰, incorporating FV and lumen diameter measurements obtained at the left and right internal carotid artery (ICA), vertebral artery (VA), and MCA. These measurements were obtained while transcutaneous carbon dioxide (PtcCO₂) level was monitored continuously.

4.3 Materials and Methods

Ethics statement

Healthy, young, non-smoking volunteers were invited to participate in the study by advertisement at the Centre Hospitalier Universitaire Vaudois and École Polytechnique Fédérale de Lausanne in Switzerland. Volunteers with a history of pulmonary, cardiac or cerebral disease were excluded. The study was carried out in accordance with the Declaration of Helsinki (1989) of the World Medical Association and was approved by the local ethics committee. All subjects gave their informed consent.

4.3.1 Ultrasound measurements

The US measurements were performed with and without CPAP (S8 AutoSet Spirit™ II, ResMed Inc, Poway, CA) applied at 15 cmH₂O through a fitted full face mask MIRAGE QUATTRO® (ResMed®, ResMed Inc, Poway, CA) in a randomized order following a structured protocol. Randomization was accomplished by flipping a coin. The measurements were performed during the afternoon at atmospheric pressure at least two hours after the last meal and drink with caffeine in a standard room with controlled temperature. All volunteers, who were studied in the supine position with a head tilt of 30°, tolerated CPAP at 15cm H₂O well. The arteries were studied with and without CPAP in the following order: a) right proximal ICA and VA, b) left proximal ICA and VA and c) right and left MCA.

Peak systolic and end-diastolic FV and arterial diameter were obtained in M-mode⁷³ for three time points at the left and right ICA and VA using a 5-8MHz- duplex probe (Echograph Acuson Sequoia 512). Only FV was studied at the MCAs using a 2-4MHz-pulsed TCD probe of the same manufacturer. PtcCO₂ level was monitored with a 'Tosca 500' system (Radiometer Basel AG, Basel, Switzerland) using a single sensor applied to the chest. SaO₂ and heart rate (HR) were monitored with a finger pulseoximeter (Ohmeda) during the measurement period. Blood pressure (BP) was recorded before and after each test. US measurements under CPAP began after the PtcCO₂ level returned to baseline (± 2 mmHg) or at steady state after at least 15 minutes of CPAP use. This time period was sufficient to ensure a steady state as changes in CBF caused by an alteration in PCO₂ level have been found to be completed within 30 seconds¹⁴¹.

4.3.2 CBF calculations

A single investigator performed all of the US exams and all velocity and diameter measurements, based on the US images, were performed by two investigators. Exams were reviewed by both investigators to assure that measurements were performed on the same M-mode screen and on the correct vessel within the region of interest. The mean value of both investigators' measurements was used for the calculations. The mean FV in each vessel was calculated by measuring the peak systolic, FV_{sys} , and end diastolic, FV_{dia} , FV for three cardiac cycles according to the following equation:

$$FV = \frac{FV_{sys} + 2FV_{dia}}{3}$$

Mean diameter \bar{D} of each vessel for three cardiac cycles was calculated based on the M-mode US measurements⁷³ using a similar equation as Eq. 1, except with FV replaced with the systolic and diastolic diameter. An example of the FV and diameter measurement obtained at the right ICA is shown in Figure 4.1.

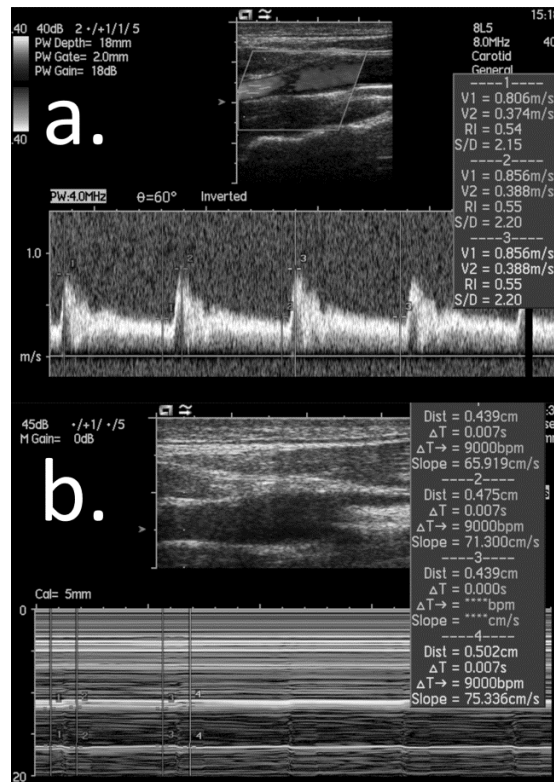


Figure 4.1 Flow velocity (a) and vessel diameter in M-mode ultrasound (b) measured at the right ICA.

Flow rate, Q (ml/min), in each vessel was calculated by the following equation and total experimental CBF, CBF_{exp} , was determined by the sum of the flow in the left and right ICAs and VAs assuming a parabolic velocity profile¹⁴²:

$$Q = \frac{FV}{2} * \frac{\pi \bar{D}^2}{4}$$

$$CBF_{exp} = Q_{ICAs} + Q_{VAs}$$

Vascular related results are presented as the average of the left and right vessel measurements for the 23 subjects (i.e. $FV_{ICA} = \frac{1}{23} \sum_{n=1}^{23} (FV_{ICAleft} + FV_{ICAright})/2$). The following method was used to predict a theoretical change in CBF given an experimentally measured change in PtcCO₂ level. The relationship between CBF (ml/min/100 g brain tissue) and arterial CO₂ tension (mm Hg) has been quantified in the literature (Figure 4.2)^{59, 143-149}. Table 4.1 summarizes the slope of the CBF to PCO₂ curve at baseline PCO₂ level based on Figure 4.2 and other studies in the literature.

The average slope was calculated to be 1.65, with a maximum and minimum slope value of 3.20 and 0.19, respectively (standard deviation = 0.92). The average slope was used to determine a theoretical reduction in CBF in ml/min/100 g of brain tissue, $\Delta CBF_{theor100}$, based on the experimentally measured change in PtcCO₂ level with and without CPAP ($\Delta CBF_{theor100} = -\text{slope} * \Delta PtcCO_2$). The total theoretical change in CBF was determined ($\Delta CBF_{theor} = 14 * \Delta CBF_{theor100}$) assuming that the human brain is approximately 14 times the weight of a Rhesus monkey¹⁴⁹. The CBF_{exp} measurements were used to determine the experimental CBF reduction (ΔCBF_{exp}). Positive CBF reduction values were defined to indicate that total CBF decreased under CPAP, and vice versa. The average and standard deviation of ΔCBF_{exp} and ΔCBF_{theor} were determined for the 23 subjects based on both investigators measurements.

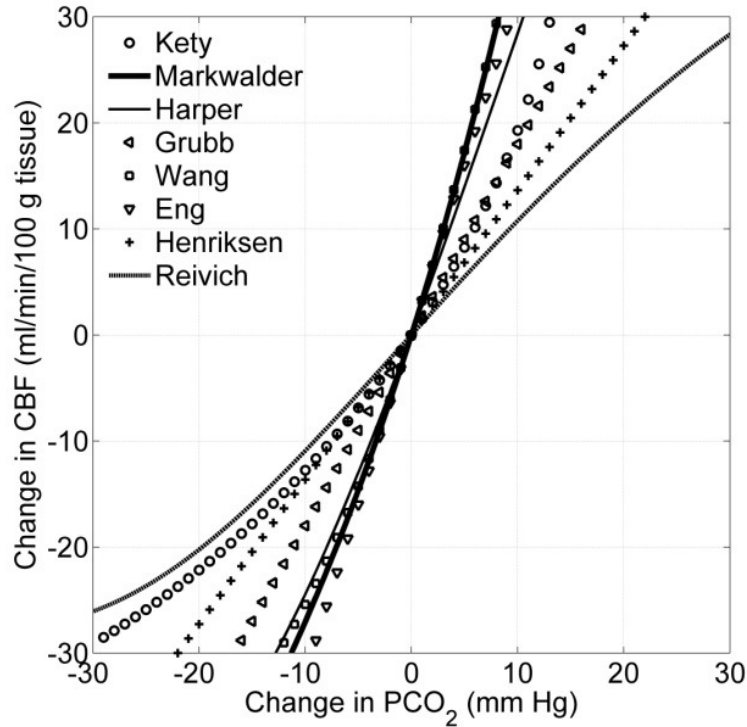


Figure 4.2. Relation for change in CBF (ml/min/100g brain tissue) given a change in PCO₂ (mm Hg) based on studies in the literature (Kety et al.¹⁴³, Markwalder et al.⁵⁹, Harper et al.¹⁴⁴, Grubb et al.¹⁴⁵, Wang et al.¹⁴⁶, Eng et al.¹⁴⁷, Henriksen et al.¹⁴⁸, Reivich et al.¹⁴⁹).

Table 4.1. Hemodynamic results for the 23 volunteers with and without CPAP. All values are expressed as mean (SD). Abbreviations: CPAP: continuous positive airway pressure; BP: blood pressure; HR: heart rate; PtcCO₂: transcutaneous carbon dioxide level; SaO₂: oxygen saturation; FV: flow velocity; PI: pulsatility index; D: diameter; CBF: cerebral blood flow; SD: standard deviation.

Investigator	Animal type	CBF measurement technique	Slope ($\Delta\text{CBF}/\Delta\text{PCO}_2$) at baseline PCO ₂
Kety ¹⁴³	Man	N ₂ O	1.47
Markwalder ⁵⁹	Man	Doppler	3.12
Wasserman ^{145, 150}	Man	N ₂ O	2.17
Harper ¹⁴⁴	Dog	Kr ⁸⁵	2.69
Grubb ¹⁴⁵	Rhesus Monkey	H ₂ ¹⁵ O	1.80
Wang ¹⁴⁶	Rat	NO	3.10
Eng ¹⁴⁷	Man	NO	3.20
Henriksen ¹⁴⁸	Man	Intraarterial ¹³³ Xe	1.36
Reivich ¹⁴⁹	Rhesus Monkey	Thermistor Flowmeter	1.11
White ¹⁵¹ , Lambertsen ¹⁵²	Man	N ₂ O	1.34
Alexander ¹⁵³	Man	Kr ⁸⁵	1.06
Pierce ¹⁵⁴	Man	N ₂ O	0.43
White ¹⁵¹	Monkey	Cerebral venous flowmeter	1.11
James ¹⁵⁵	Baboon	Kr ⁸⁵	1.22
Smith ¹⁵⁶	Goat	Kr ⁸⁵	1.79
Raichle ¹⁵⁷	Dog	Kr ⁸⁵	0.90
Fujishima ¹⁵⁸	Dog	N ₂ O	0.19
			Ave 1.65
			Max 3.20
			Min 0.19
			Std 0.92

4.3.3 Statistical analysis

Statistical analysis was conducted with STATA software (version 11; College Station, TX, USA). The variable measured parameters were compared between conditions using a two-tailed paired t-test and Mann-Whitney test, where appropriate. The level of significance was set at 95%. Multivariate logistic regression, limited to two variables according to the total number of subjects, was performed with predictors with a univariate result of $p < 0.1$. Agreement between investigators was calculated with the Lin's concordance correlation coefficient for agreement on a continuous measure.

4.4 Results

The study group was comprised of 23 subjects (12 male, 11 female) aged from 20 to 30 years (mean \pm SD) (25.1 ± 2.6 years) with a mean body mass index (BMI) of 21.8 ± 2.04 kg/m². Thirteen volunteers began the randomized measurement protocol with CPAP. Table 4.2 shows a summary of the hemodynamic data and results for the CBF calculations with and without CPAP.

With CPAP, FV decreased significantly in the ICA (0.05 ± 0.05 m/s, $p = 0.0002$) and the MCA (0.038 ± 0.06 m/s, $p = 0.009$), but not significantly at the VA (0.009 ± 0.04 m/s, $p = 0.25$). Decrease in the ICA diameter was insignificant (-0.06 ± 0.2 mm, $p = 0.14$), while decrease in VA diameter was significant (-0.12 ± 0.12 mm, $p < 0.001$). In a multivariate robust regression, with total CBF reduction as a dependant variable, only ICA FV ($p < 0.001$) remained significant, whereas MCA FV was not significant ($p = 0.21$). A significant reduction in PtcCO₂ under CPAP (2.6 ± 2.4 mm Hg, $p < 0.001$) and an increase in mean BP (2.7 ± 3.6 mm Hg, $p = 0.0017$) were measured. No significant change in SaO₂ ($0.4 \pm 1.6\%$, $p = 0.21$) and HR (0.9565 ± 7.3173 , $p = 0.62$) was

measured. Figure 4.3 illustrates the total CBF_{exp} reduction compared to the CBF_{theor} reduction for each of the 23 subjects and the average reduction for the entire study.

The mean CBF_{exp} decreased under CPAP by 12.5% ($66.6 \pm 63\text{ml/min}$, $p<0.001$), while the mean decrease in CBF_{theor} was 11.9% ($62.8 \pm 54.4\text{ml/min}$, $p<0.001$). There was no significant difference between experimental and theoretical CBF reduction ($3.84 \pm 79\text{ml/min}$, $p=0.40$). No difference was found according to the sequence of measurements with or without CPAP, gender, height, weight or BMI. No significant differences were found also between the left and right side US measurements of each arterial vessel. Agreement between final investigators results for CBF reduction in every subject was 87% (95%, confidence interval 0.73-0.97).

Table 4.2. Hemodynamic results for the 23 volunteers with and without CPAP. All values are expressed as mean (SD).

	NO CPAP (SD)	CPAP (SD)	p-value
BP(mmHg)	87.3 (6.6)	90 (7.1)	0.0017
HR	68.8 (10.6)	69.7 (12)	0.62
PtcCO ₂ (mm Hg)	36.3 (5.3)	33.7 (6.2)	<0.001
SaO ₂ (%)	97.5 (1.2)	97.9 (1.3)	0.21
FV _{ICA} (m/s)	0.48 (0.07)	0.43 (0.06)	0.0002
FV _{VA} (m/s)	0.31 (0.05)	0.30 (0.05)	0.25
FV _{MCA} (m/s)	0.65 (0.12)	0.62 (0.12)	0.009
PI _{ICA}	0.98 (0.18)	0.97 (0.22)	0.76
PI _{VA}	1.20 (0.18)	1.21 (0.18)	0.92
PI _{MCA}	0.78 (0.1)	0.82 (0.1)	0.12
\bar{D}_{ICA} (mm)	4.13 (0.6)	4.07 (0.6)	0.14
\bar{D}_{VA} (mm)	2.98 (0.4)	2.85 (0.4)	<0.001
CBF(ml/min)	535 (122.1)	468.5 (105.6)	<0.001

Abbreviations: CPAP: continuous positive airway pressure; BP: blood pressure; HR: heart rate; PtcCO₂: transcutaneous carbon dioxide level; SaO₂: oxygen saturation; FV: flow velocity; PI: pulsatility index; D: diameter; CBF: cerebral blood flow; SD: standard deviation.

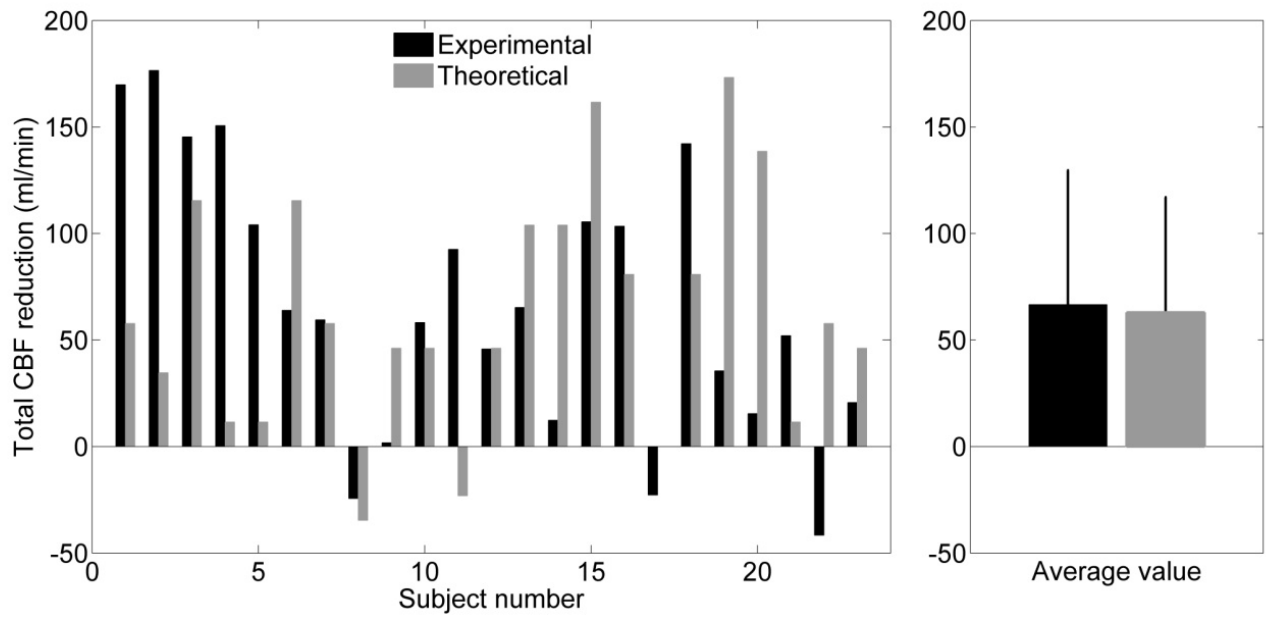


Figure 4.3 Comparison of the total CBF reduction (ml/min) under CPAP, ΔCBF_{exp} , with the predicted theoretical reduction in CBF, ΔCBF_{theor} , for each of the 23 subjects (left) and the average value for CBF reduction in all subjects (right).

4.5 Discussion

We observed that CPAP applied at 15 cmH₂O significantly decreased the total CBF in healthy awake volunteers. The change in CBF was studied using a method that integrates ultrasound measurements of blood FV and arterial lumen diameter obtained at the left and right ICA, VA, and MCA.

Previous studies measured FV and PI in the MCA with the hypothesis that these parameters were a good indicator of total CBF^{26, 27, 58, 138, 139}. Thus, the arterial diameter was assumed to remain stable⁶⁰. Table 4.3 summarizes the main technical characteristics and results of the previous studies that investigated the effect of CPAP on CBF hemodynamics. We chose to evaluate total CBF based on the arterial diameter and FV measured in each of the primary vessels that supply blood to the brain (ICAs and VAs). Measurement of diameter and FV in these vessels has been proposed to be a more accurate and detailed method to help estimate total CBF¹⁵⁹.

In our study we chose to monitor PCO₂ transcutaneously because it avoids the confounding dilution effect of end-tidal CO₂ measurements that occurs due to the mixing of expired CO₂ with incoming CO₂-free CPAP airflow. However, end-tidal PCO₂ monitoring has also several advantages, such as the quick response under provocative conditions as well as the fact it provides detailed information about the breathing pattern (i.e. respiratory rate). In the case of end-tidal PCO₂ monitoring, the problem of CO₂-dilution in the mask under CPAP could be avoided by the insertion of a thin catheter into one nostril far from the expiratory port^{58, 160}. The underlying physiological mechanism that results in CBF change due to CPAP usage is complex. A CPAP-induced increase in intrathoracic pressure may provoke hemodynamic effects (i.e. reduced cardiac output, reduced venous return, increased cerebral venous pressure) that could result in a decrease of cerebral perfusion pressure and CBF. On the other hand, it is well accepted that PCO₂ affects the muscular regulation of the arterial wall, with hypercapnia leading to vasodilatation and hypocapnia to vasoconstriction. The relative contribution of CPAP-induced changes, such as intrathoracic pressure and PCO₂ level, to CBF change is unknown.

Table 4.3. Summary of the main technical features of the studies in the literature that investigated the impact of CPAP on CBF hemodynamics

Investigator	Level of CPAP	#of subjects/health condition	Position of the subject/ type of CPAP mask	US measurement technique	CBF measurement technique	PCO ₂ measurement	Hemodynamic monitoring	Results
Bowie et al. ²⁷	5, 10 cm H ₂ O	15 awake/healthy	Supine/mouthpiece	TCD	FV on MCA	End-tidal CO ₂	BP	No significant change
Scala et al. ⁵⁸	5, 10, 15 cm H ₂ O	25 awake/healthy	Supine/mouthpiece	TCD	FV on MCA	End-tidal CO ₂	BP, HR, RR, SaO ₂ , anxiety score	Decrease of FV
Scala et al. ¹⁶⁰	Auto-CPAP mode (4-10 cm H ₂ O) and increasing levels of 5, 10, 15 cm H ₂ O	12 asleep and awake/acute stroke patients	Supine/nasal or facial	TCD	FV on MCA	End-tidal CO ₂	BP, SaO ₂	Decrease of FV
Haring et al. ²⁶	12 cm H ₂ O	9 awake/healthy	Supine/mouthpiece	TCD	FV on MCA	End-tidal CO ₂	BP, HR	Increase of FV
Present study	15 cm H ₂ O	23 awake/healthy	Supine/mouthpiece	Duplex color Doppler US	FV and lumen diameter of ICA, VA and FV on MCA	Transcutaneous PtcCO ₂	BP, HR, SaO ₂	Decrease of CBF

Abbreviations: CPAP: continuous positive airway pressure; BP: blood pressure; HR: heart rate; PtcCO₂: transcutaneous carbon dioxide level; SaO₂: oxygen saturation; FV: flow velocity; CBF: cerebral blood flow.

Our results supported that CBF reduction due to CPAP usage was primarily mediated through hypocapnic vasoconstriction. CPAP-induced intrathoracic pressure and venous hemodynamic changes did not appear to play an important role in CBF reduction. To determine the theoretical CBF effect of variation in PCO₂ level with and without CPAP, we used the average value of the slope of the CBF responsiveness to acute change in PCO₂ reported in the literature (Table 4.1). The difference between the theoretically predicted and experimentally measured change in CBF was not found to be significant (Figure 4.3). This suggests that the theoretical prediction of the CBF decrease, which takes into account only the monitored PtcCO₂ level, was sufficient to capture the CBF changes that were observed. Thus, an increase in intrathoracic pressure alone did not appear to play a significant role in CBF alteration.

This study cannot conclude if CPAP pressure had a direct impact on total CBF. This is because the statistical calculation used to determine that intrathoracic pressure increase did not have a significant impact on total CBF was critically dependent on the assumed slope for change in CBF to PCO₂ level. A wide range of slope values have been reported in the literature (Table 4.1, slope = 0.19 to 3.20) and thus it is possible that the theoretical predictions over or underestimated CBF change. For example, if the slope used to determine the theoretical change in CBF was chosen to be <1.1, the impact of CPAP pressure would have been found to be significant. To better understand the impact, if any, of intrathoracic pressure alterations brought on by CPAP usage on CBF, a study would need to be conducted with the PCO₂ level held constant while CPAP pressure is altered incrementally.

It appears that CPAP may decrease total CBF in healthy awake volunteers indirectly by modulating the PCO₂ level. However, the physiological mechanism for decrease of PCO₂ under CPAP is unclear. Our findings show a significant increase in BP under CPAP. This may be due to the autoregulation of systemic BP which seeks to maintain stable CBF¹⁶¹. Similarly, SaO₂ in the healthy range has little effect on the radius of blood vessels and subsequently on CBF¹⁶². One hypothesis for the change in total CBF is that CPAP

improves the lung perfusion/ventilation ratio, which may increase CO₂ washout. Another explanation could be that the subjects experienced a mild hyperventilation due to anxiety induced by breathing against the CPAP. In our study, anxiety was not measured, but our measurements were obtained after an acclimatization period. It is also possible that anxiety had a direct influence on CBF.

Changes in CBF induced by CPAP could have important clinical implications in patients requiring an optimal and stable CBF such as acute stroke patients. The question of CPAP use in early stroke patients with OSAS remains open considering the positive effect of CPAP on apnea-induced oxygen deprivation versus possible negative effects of CPAP, such as reduction of total CBF. A specific study would need to be performed to examine the impact of CPAP pressure on CBF in stroke patients to validate these conjectures.

Limitations

A primary limitation of this study is that the subjects who were tested were both healthy and awake. Subjects who are awake may react differently to CPAP than sleeping OSAS patients. However, these measurements could not be obtained on sleeping subjects, as these measurements would awaken them, and variable comorbidities (e.g. obesity, heart failure, medication) would make comparison between the subjects' results unreliable. Furthermore, our results suggest that non-invasive techniques that could be conducted during sleep, such as transcranial Doppler ultrasound obtained at the MCAs, may not be sufficient to measure the changes in CBF that were observed (Table 4.1). In our study, measurement of FV and diameter at all vessels supplying blood to the brain was needed to detect the CBF changes. In a multivariate robust regression with total CBF reduction as a dependent variable, only ICA FV remained significant. From a clinical point of view, this result justifies the fact that at bedside sampling of this parameter could more easily approximate total CBF, something that could be less time-consuming especially in the case of patients such as acute stroke patients or OSAS patients with ischemic encephalopathy. It would be very interesting for future studies to examine this US approach on the aforementioned clinical population.

A secondary limitation of this study is that even though the assignment to spontaneous breathing or to CPAP was based on a randomized order following a structured protocol, a "breathing-machine effect" could not be excluded¹⁶³. However, the protocol was set to evaluate the global impact of the CPAP (mask in combination with pressurized air) to cerebral hemodynamics as a mainstay therapy of OSAS. To further understand the effect of the CPAP mask and that of the CPAP mask and pressurized air using a "sham ventilation", a separate study should be conducted focused on the potential effect of the mask itself on the breathing pattern independently from the pressurized air.

Another limitation of this study is that CPAP was adjusted at the high level of 15 cm H₂O. Haring et al.²⁶, Droste et al.¹⁶⁴ submitted volunteers to CPAP 12 and 9 cm H₂O, respectively whereas Bowie et al.²⁷ and Scala et al.⁵⁸ studied the effects of different and increasing levels of CPAP on CBF. In our study, we applied CPAP of 15cm H₂O in young healthy awake volunteers. This high level of CPAP is rarely used in controlling patients with sleep disordered breathing. CPAP at 15 cm H₂O was useful in the experimental setting of our study in order to underline the maximum physiological effects of CPAP on cerebral hemodynamics by minimizing possible bias. The level of CPAP was set at 15 cm H₂O on the machine. It is possible that this high pressure could have resulted in substantial air-leaks and caused a gap between the applied and delivered mask pressure and subsequently increased subject discomfort^{165, 166}. However, during the ultrasound measurements of our study the presence of air-leaks was repeatedly assessed by the MD and adjusted when needed. All volunteers tolerated well the mask with CPAP at 15 cm H₂O.

Another limitation of this study is due to the operator-dependence of the measurements used to determine CBF. To minimize operator-dependent error, both operators that conducted the vessel lumen measurements reviewed the US images together after the measurements were made. This review helped to assure that the correct vessel and the same acquisition period were used for the diameter measurements. With this precaution, a good agreement score was found. In addition to operator-dependent error, our study utilized equations to calculate blood flow based on simplified hydrodynamics. To calculate total CBF, it was assumed that zero phase delay occurred between the arrival of the FV_{sys} at the ICA and VA and that a parabolic velocity profile was present to determine the true flow rate within the vessels¹⁴². To minimize measurement error, the mean flow in each vessel was approximated using the

average of three sequential diastolic and systolic FV and diameter measurements. Even with these simplifications, the presented methodology is robust because it is sensitive to changes in CBF, the measurement of which was the primary objective of this study.

In conclusion, our study presents a noninvasive bedside method to evaluate total CBF in awake subjects using CPAP that could potentially be an improvement over other methods which only take into account FV at the MCA. The results suggest that CPAP at 15 cmH₂O significantly decreases CBF in healthy, awake volunteers. This effect seems to be mediated predominately through the hypocapnic vasoconstriction and likely, to a lesser extent, through the direct effect of CPAP on intrathoracic pressure and venous hemodynamics. These results suggest that CPAP should be cautiously used in patients with unstable cerebral hemodynamics.

5. Continuous positive airway pressure alters cranial blood flow and cerebrospinal fluid dynamics at the craniovertebral junction

Theresia I. Yiallourou¹, Marianne Schmid Daners², Vartan Kurtcuoglu³, Jose Haba-Rubio⁴, Raphael Heinzer⁴, Eleonora Fornani⁵, Francesco Santini⁶, Daniel B. Sheffer⁷, Nikolaos Stergiopoulos¹, Bryn A. Martin^{7,8}

¹Laboratory of Hemodynamics and Cardiovascular Technology,
École Polytechnique Fédérale de Lausanne, Switzerland

²Institute for Dynamic Systems and Control,
Department of Mechanical and Process Engineering, ETH Zurich, Switzerland

³The Interface Group, Institute of Physiology, University of Zurich, Switzerland

⁴Centre Hospitalier Universitaire Vaudois (CHUV),
Centre for Investigation and Research on Sleep (CIRS), Lausanne, Switzerland

⁵Center for Biomedical Imaging (CIBM), CHUV, Lausanne, Switzerland

⁶Radiological Physics, University of Basel Hospital, Basel, Switzerland

⁷Department of Biomedical Engineering, University of Akron, OH, U.S.A

⁸Conquer Chiari Research Center, University of Akron, OH, U.S.A

5.1 Abstract

The impact of continuous positive airway pressure (CPAP) at 15 cmH₂O on total cerebral blood flow (tCBF), jugular venous flow (tJVF) and cerebrospinal fluid (CSF) dynamics was investigated in 23 healthy male subjects. 2D phase-contrast MRI (2D PC MRI) flow measurements, at the left and right internal carotids, vertebral arteries, jugular veins and spinal subarachnoid space at level C2-C3, were acquired with and without CPAP. Heart rate, transcutaneous carbon dioxide (PtcCO₂) and oxygen saturation were continuously monitored for each subject. Results showed that CPAP decreased CSF stroke volume and pulse amplitude by 20% (p=0.003) and 15% (p=0.005), respectively. No significant changes were found in tCBF, whereas tJVF pulse amplitude decreased by 21% (p=0.004). The latter finding was supported by the spectral analysis, where the first harmonic was significantly decreased with CPAP (p=0.001). CSF and tJVF waveforms showed significant spatial and temporal differences. These changes are attributed to the direct impact of CPAP on the intrathoracic pressure and were not correlated to the reduction by 5% of PtcCO₂ (p=0.003). The findings, although obtained in healthy volunteers, should be taken into consideration when deciding to treat with CPAP patients with craniospinal disorders and unstable cerebral hemodynamics such as in acute stroke.

Keywords

Cerebral blood flow, cerebrospinal fluid dynamics, cervical spine, continuous positive airway pressure, PtcCO₂, 2D PC MRI

5.2 Introduction

Clinical evidence and research has long shown a strong coupling of intracranial hemodynamics and cerebrospinal fluid (CSF) pulsations¹⁶⁷. A full understanding of the coupling between the two systems is thought to be important to understand the pathophysiology of cerebrovascular disorders such as stroke, interstitial fluid transport within the brain^{168, 169}, and craniospinal disorders including type I Chiari malformation¹³¹, syringomyelia¹⁷⁰ and hydrocephalus^{51, 171}. A number of studies have sought to understand the spinal subarachnoid space behavior and its importance on the overall intracranial balance between the arterial, venous, and cerebrospinal fluid (CSF) flow pulsations^{48, 49, 172}. One aspect of the coupling that is little understood is the physiological importance of the spinal subarachnoid space. Researchers have postulated that under normal conditions the healthy spinal subarachnoid space may act as a “notch filter” that dampens incoming cerebral blood flow (CBF) pulsations to supply smooth blood flow to the neural tissue^{4, 173}.

Non-invasive 2D phase-contrast magnetic resonance imaging (2D PC MRI) enables measurement of the CSF and CBF system fluid flow^{67, 84} and has been also used to estimate venous flow in the jugular and intracerebral veins as well as the major sinuses⁴⁸. According to the Monro–Kellie doctrine, the arterial, venous, CSF and brain tissue compartments co-exist in a state of dynamic equilibrium throughout the cardiac cycle^{174, 175}. A change in the volume in one component requires a change in the volume in either one or both of the other two. Schmid Daners et al.¹¹¹ showed using 2D PC MRI that the coupling of cerebral arterial inflow and CSF dynamics is age and sex dependent. A number of studies have been devoted to assessment of the cerebral venous system^{176, 177}. In a recent study, El Sankari et al.¹⁷⁷ simultaneously compared the venous flow, arterial and CSF flows of patients with multiple sclerosis to age and sex matched healthy adults. Results documented complex and heterogeneous venous drainage pathways and decrease in CSF oscillations.

The interaction between intrathoracic pressure and ICP due to posture¹⁷⁸, abdominal pressure changes¹⁷⁹ and coughing⁵⁶ have been well reported in the literature. These pressure changes are transmitted from the abdomen into the CSF system through the dural venous sinuses and epidural venous plexus¹⁸⁰. Published data have shown physiologic variations in the dural venous sinuses drainage that can occur either under specific respiratory mechanisms such as Valsava maneuver¹⁸¹ or with posture changes¹⁸². Thus, it is possible to manipulate the intrathoracic pressure by a number of non-invasive maneuvers that in turn modify the intracranial system as a whole.

One method to non-invasively alter intrathoracic pressure is with the use of continuous positive airway pressure (CPAP), the most widely accepted treatment for sleep apnea syndrome and a pathology documented to commonly occur in type I Chiari malformation patients²⁴. CPAP acts as a pneumatic “splint” by producing a positive pressure, thereby preventing upper airway collapse during sleep. While CPAP use has become routine, the full physiological effect of its use on CBF, venous flow and CSF dynamics is not yet fully understood. Studies have shown that CPAP affects cerebral hemodynamics in multiple ways^{27, 28}. Considering that a rise of the intrathoracic pressure increases the jugular venous pressure, CPAP could have an effect on CBF by reducing the cerebral perfusion pressure²⁹. Concomitantly, changes in the blood flow volume due to the increased intrathoracic pressure hinders cerebral venous drainage via the jugular veins³⁰. In human volunteers CPAP breathing has been shown to increase lumbar CSF pressure³¹ and reduce CSF peak velocity in the aqueduct of Sylvius³².

The study at hand hypothesized that acute pressure changes in the chest caused by the application of CPAP would alter intracranial and spinal CSF flow dynamics in the following manner: 1) the stroke volume (SV) and pulsation of CSF would decrease and 2) venous flow dynamics would be noticeably altered. We tested our hypothesis by applying CPAP at 15 cmH₂O in 23 healthy male volunteers and measuring physiological alterations using a 2D PC MRI protocol to quantify blood flow in the left and right internal carotid arteries (ICA), left and right vertebral arteries (VA), left and right jugular veins (JV) and CSF flow at the C2-C3 level of the cervical spinal canal with CPAP applied. Baseline measurements without the CPAP followed the initial recording with the CPAP using the same protocol. Using these measurements the

influence of CPAP on total cerebral blood flow (tCBF), total jugular venous (tJVF) and spinal CSF flow was assessed in terms of flow based metrics and spectral content of the flow waveforms.

5.3 Materials and Methods

Ethics statement

Healthy, young, non-smoking male volunteers were invited to participate in the study by advertisement at the local university hospital of Lausanne, Centre Hospitalier Universitaire Vaudois (CHUV) and École Polytechnique Fédérale de Lausanne in Switzerland. Volunteers with a history of pulmonary, cardiac, neurological, cerebral disease, spinal trauma or diagnosed sleep apnea were excluded. The study was carried out in accordance with the Declaration of Helsinki (1989) and was approved by the Swiss Human Research Ethics Committee of Vaud. The MR data acquisition was performed at the Centre d'Imagerie BioMédicale (CIBM) – Department of Radiology, CHUV in Lausanne. Before the MR exams, written informed consent was obtained from all the volunteers. Prior to further data processing MR data were anonymized.

5.3.1 *In vivo* 2D PC MR measurements

Twenty three healthy male volunteers, aged 24 ± 2.1 years with a mean body mass index (BMI) of 22.9 ± 2.51 kg/m² were scanned on a 3T MRI scanner (Siemens Magnetom Trio Tim, Siemens, Erlangen, D) with a standard 4-channel phased array carotid coil (Magnet Mach NET 4CHN, Siemens A Tim Coil), placed next to the left and right internal carotid artery and a neck coil (Neck matrix, 4CHN, Siemens) with CPAP (S8 AutoSet Spirit™ II, ResMed Inc, Poway, CA) applied at 15 cmH₂O through a fitted full face mask MIRAGE QUATTRO® (ResMed®, ResMed Inc, Poway, CA) in a specific order following a structured protocol. Baseline measurements without CPAP followed directly after the removal of the CPAP with the same protocol. The measurements were performed during the afternoon at atmospheric pressure at least two hours after the last meal and drink with caffeine in the MR scanner room with controlled temperature. A medical doctor was present throughout testing. Subjects were supine with their necks in a neutral position.

Both anatomy and cine phase contrast (PC) images were acquired. A set of T2-weighted turbo spin-echo sagittal images defined the anatomy in the upper cervical spinal canal. Fluid flow acquisition planes, oriented perpendicular to the nominal flow direction, were selected on a midsagittal scan at the C2-C3 subarachnoid space (n=5) (Figure 5.1a). Both left and right ICAs, left and right VAs and left and right JVs were imaged simultaneously with the same slice plane at the C2-C3 cervical spinal vertebrae orthogonal to the spinal cord with CPAP applied and during the baseline measurements (Figure 5.1b). Imaging parameters for the arterial and jugular flow measurements were set to an in plane acquisition resolution of 0.7×0.7 mm² with a slice thickness of 5 mm, a 124X114 acquisition matrix, a flip angle of 20°, a bandwidth of 814 Hz/Px, a field of view (FoV) read of 190x112, a FoV phase of 59.4%, a base resolution of 256, a phase resolution of 100%, a velocity encoding (VENC) of 80 cm/s (through-plane direction), a repetition time (TR) of 20 ms and an echo time (TE) of 6.5 ms, which results in a temporal resolution of 20 ms. The minimum repetition time available was used to optimize temporal resolution, and the minimum echo time available was used to optimize signal-to-noise ratio and to reduce intravoxel phase dispersion. All scans were prospectively triggered with electrocardiographic (ECG) gating. The number of heart phases acquired was adapted to the cardiac frequency and fixed to 35 phases for all the subjects.

CSF flow measurements were performed at the same location as the blood flow measurements (Figure 5.1c) but using a slightly modified protocol: the imaging parameters for the CSF flow acquisition were identical to those described for the vascular flow measurements, except for the VENC which was set to 10 cm/s and flip angle to 15°. Scan time was 8-10 minutes with the CPAP and another 8-10 minutes

without the CPAP, depending on the heart rate while the whole examination protocol lasted approximately 45 minutes.

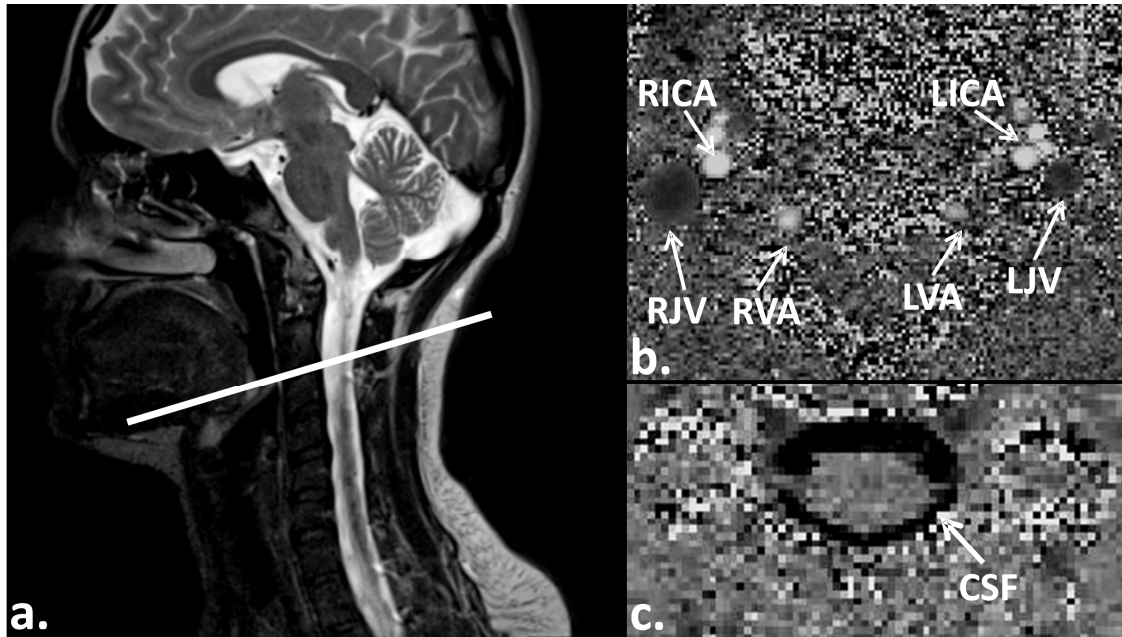


Figure 5.1. **a)** Sagittal T2-weighted localizer sequence used to select the C2-C3 vertebral level for 2D PC MRI flow quantification. The acquisition plane was selected perpendicular to the flow direction. **b)** 2D PC MRI phase mapping at the C2-C3 level used to measure vascular flows, in the left (L) and right (R) internal carotid arteries (ICA), vertebral arteries (VA) and jugular veins (JV), with and without CPAP (VENC = 80 cm/s, black voxels denote caudal directed flow, white voxels denote cranial directed flow). **c)** 2D PC MRI measurement of CSF flow at the C2-C3 measurement plane (VENC = 10 cm/s).

5.3.2 Physiological monitoring

Transcutaneous partial pressure of carbon dioxide (P_{tCO_2}), oxygen saturation (SaO_2) and heart rate (HR) were monitored throughout the exam with a ‘Tosca 500’ system (Radiometer Basel AG, Basel, Switzerland) using a sensor applied at the top surface of the foot. MRI measurements under CPAP were obtained first after the P_{tCO_2} level return to baseline (± 2 mmHg) or at least 15 minutes of CPAP use. Following MRI measurements with CPAP applied, the mask was removed and the same protocol repeated without CPAP to obtain the baseline measurements. All subjects were asked to rate their anxiety level under CPAP during the MR measurements from a scale of 0-3 where 0 refers to ‘not at all anxious’, 1 refers to ‘slightly anxious’, 2 refers to ‘moderately anxious’ and 3 refers to ‘highly anxious’.

5.3.3 Data processing and analysis

All 2D PC MR images were post-processed with Segment (Standalone version, Medviso AB, Lund, Sweden) by one operator blinded to subject status. For each scan, flow was determined with an adaptive region of interest (ROI) selection using manual segmentation based on the instantaneous lumen area. Images were visually inspected for adequate signal to noise at the ROI. Datasets presenting major artifacts or too low signal levels were excluded from the subsequent analyses. When aliased voxels were detected, aliasing correction was performed automatically by the unwrap procedure in Segment. Eddy current compensation was implemented automatically as well by the “eddy current compensation procedure and the Phantom experiment method (GE method)¹⁸³ in Segment.

The ICAs, VAs and JVs were segmented frame by frame in order to account for the temporal change in their cross-section due to the blood pulsation. The cervical spinal subarachnoid space was segmented in

single-image frames since its cross-sectional area did not vary with time. The ROI of spinal subarachnoid space was best outlined in early systole, when the contrast between CSF and spinal cord was at its maximum.

Data visualization was performed using MATLAB R2010b (The Mathworks Inc., Natick, MA, USA). Flow waveforms were obtained from the recorded velocity for each voxel from the 2D PC MR images. Then they were integrated over the area of the ROI in question using image processing software developed within MATLAB. The process involved integration of the velocity over the manually segmented cross-sectional area for an entire cardiac cycle: $Q(t) = \sum A_{\text{voxel}} [V_{\text{voxel}}(t)]$, where A_{voxel} is the area of the one MRI voxel, V_{voxel} is the velocity of the corresponding voxel, and $Q(t)$ is the voxel summation of the flow for each voxel of interest⁸⁴.

The total cerebral blood flow (tCBF) into the cranial space was calculated by summing the blood flow rates of all four main vessels supplying blood to the brain (left and right ICAs and left and right VAs): $tCBF = Q(t)_{\text{ICAs}} + Q(t)_{\text{VAs}}$, where $Q(t)_{\text{ICAs}}$ and $Q(t)_{\text{VAs}}$ are calculated as the sum of the left and right vessel measurements (i.e., $Q_{\text{ICAs}} = Q(t)_{\text{ICAleft}} + Q(t)_{\text{ICAright}}$ and $Q_{\text{VAs}} = Q(t)_{\text{VAleft}} + Q(t)_{\text{VAright}}$. Estimation of the tJVF was obtained by the summation of the flow rates through the left and right JVs: $tJVF = Q(t)_{\text{JVleft}} + Q(t)_{\text{JVright}}$. Unmeasured venous outflow due to the structural complexity and individual variation of the venous flow system (epidural, vertebral and deep cervical veins) as well as other secondary channels such as cavernous-facial outflow were not taken into consideration. CSF flow waveform was offset so the net CSF flow per cycle was zero since the net flow in the spinal subarachnoid space is known to be nearly zero⁴³.

Volumetric flow rates (mL/cardiac cycle) were also determined for both the vascular and the spinal CSF compartments. The stroke volume (SV) was calculated using the trapezoidal rule by computing volume changes for each time increment, which correspond to the area under the waveform curve of the flow difference into and out of the ROI. The SV at a given time interval was thus obtained by the summation of the volume changes dQ_{i-1} and dQ_{i-1i} from the first to the current time intervals $\Delta t = t_i - t_{i-1}$ as $SV_i = \sum_{i=1}^n [dQ_{i-1} + dQ_i] \times [t_i - t_{i-1}] / 2$, where n refers to the number of time points in one cardiac cycle⁸⁴.

For the frequency and flow rate analysis, the data were temporally and spatially normalized according to Schmid Daners et al.¹⁸⁴. The length of the cardiac cycle of the subjects with CPAP and during the baseline measurements was 0.94 ± 0.17 s and 1.0 ± 0.16 s, respectively. Therefore, the data were temporally normalized to 1 s and resampled with a time interval of 10 ms. The normalized cardiac cycle allows for comparison of frequency components (expressed in Hertz (Hz)) obtained via discrete Fourier transformation.

The frequencies were considered up to the noise level of each compartment, which was evaluated with the standard deviation of the respective compartment signals over all volunteers. The frequency components below one-fifth standard deviation were considered as noise¹⁸⁴. The zero frequency was not taken into account, because it does not correspond to the net flow due to the spatial normalization. The spinal CSF flow and the tJVF were spatially normalized by the average flow rate over the entire measurement length and the tCBF over the systole only. This approach considers the rather constant systolic phase in arteries and the small timing dependence on the systole in the other compartments. Generally, the spatial normalization accentuates the flow characteristics.

5.3.4 Statistical analysis

Statistical analysis of the hemodynamics and the CSF flow results was conducted with Minitab 16 (State College, PA) and IBM SPSS Statistics 19 (SPSS Inc., Chicago, IL, US). A Mann-Whitney U test was performed when the variances between groups were not equal. Multivariate analysis of covariance (MANCOVA) was performed to investigate the combined effects of the independent group of variables (height, weight, BMI and age) on each of the calculated dependent variables. Non-normally distributed data were logarithmically transformed before analysis. Frequencies of normalized flow rates that were

recorded with CPAP applied and during the baseline measurements were evaluated using repeated measures analysis of variance (ANOVA) with Greenhouse-Geisser correction to compensate for non-sphericity. The ANOVA was performed within both groups and between the data of the recordings with CPAP and baseline measurements. Individual frequency components were compared with a Mann-Whitney U test. Correlations were calculated with Spearman's rho. Differences were considered significant at p-value (p) < 0.05.

5.4 Results

All results are presented as mean±standard deviation (SD) for the number of volunteers (n) whose measurements were taken into account (see Tables 5.1 and 5.2). Results were analyzed in terms of average flow, systolic and diastolic peak flow, peak-to-peak pulse amplitude (PtPPA), area and SV of both the vascular and CSF components. Characteristics of the waveforms of the tCBF, tJVF, and spinal CSF flow are described with respect to their feature points and frequency content.

Table 5.1. Physiological changes assessed under CPAP usage (values expressed as mean±SD for the 23 volunteers).

	CPAP	Baseline	p-value
SaO₂ (%)	96±0.8	99±1	0.223
Heart rate (bpm)	65±10	61±8	0.006
PtcCO₂ (mmHg)	36±5	38±4	0.003

Abbreviations: CPAP: continuous positive airway pressure; PtcCO₂: Transcutaneous carbon dioxide level; SaO₂: oxygen saturation.

Table 5.2 Arterial, Vascular and CSF results for the study population with CPAP applied and at baseline

	Total cerebral blood flow			Total jugular venous flow			CSF flow		
	CPAP	Baseline	P-val.	CPAP	Baseline	P-val.	CPAP	Baseline	P-val.
n	17	18		17	14		22	23	
Average flow (mL/min)	547±119	552±104	N.S.	-529±171	-517±146	N.S.	0.00	0.00	---
Systolic peak flow (mL/min)	940±196	933±167	N.S.	-654±215	-673±195	N.S.	-165±55	-207±78	0.002 ↓
Diastolic peak flow (mL/min)	344±88	338±75	N.S.	-350±149	-261±82	<0.001 ↑	104±27	114±31	N.S.
PtPPA (mL/min)	596±131	595±123	N.S.	-304±127	-412±157	0.004 ↓	-269±79	-321±105	0.005 ↓
Area of the ROI (mm²)	64±14	67±13	0.015 ↓	84±32	66±23	<0.001 ↑	115±19	118±23	N.S.
SV (mL/cardiac cycle)	9.1±2.0	9.2±1.7	N.S.	8.8±2.8	8.6±2.4	N.S.	0.5±0.2	0.6±0.3	0.003 ↓

Abbreviations: n: indicates number of volunteers included for the measurement; CPAP: continuous positive airway pressure; CSF: cerebrospinal fluid; PtPPA: peak to peak pulse amplitude; SV: stroke volume; N.S.: no significant change (↓ refers to a statistically significant decrease and ↑ refers to a statistically significant increase under CPAP).

5.4.1 Physiological metrics

Under CPAP, a decrease in PtcCO₂ by 5% (p=0.003) and an increase in HR by 9% (p=0.006) were measured (Table 5.1). The changes in both HR and PtcCO₂ were not correlated with any of the changes observed in the arterial, venous and CSF flow dynamics. BMI was correlated with age (p=0.004). In terms

of the anxiety level, the results showed that 70% of the subjects tolerated the CPAP well, reporting “slight anxiety” with a mean value of 0.35 ± 0.49 in the anxiety index (see Methods). Anxiety was not correlated with any of the independent variables (height, weight, age, BMI). MANCOVA analysis showed that the independent group of variables (weight, height, age and BMI) had no significant effect on the PtPPA and the SV of the tCBF, the tJVF and the CSF flow. In addition, a significant effect was observed on the change of HR by the independent group ($p = 0.03$).

5.4.2 MR-based area and flow metrics

The area of tCBF that corresponds to the sum of areas of left and right ICA and VA decreased significantly under CPAP ($3 \pm 1 \text{ mm}^2$, $p=0.015$). All other changes in arterial flow-based metrics under CPAP were insignificant (Table 5.2 and Figure 5.2 A). Diastolic peak tJVF increased under CPAP by 40% ($89 \pm 67 \text{ mL/min}$, <0.001). The PtPPA of tJVF decreased by $108 \text{ mL} \pm 30 \text{ mL}$ ($p=0.004$). A significant increase in the total area of JV (sum of the areas of left and right JV) was observed ($18 \pm 9 \text{ mm}^2$, $p<0.001$). Volumetric venous and CSF flow rates are depicted in Figure 5.2B and 5.2C. CSF SV and PtPPA decreased by 20% ($-0.13 \pm 0.09 \text{ mL}$, $p=0.003$) and 15% ($-52 \pm 26 \text{ mL/min}$, $p=0.005$), respectively (Table 5.2). Spinal subarachnoid space area did not change under CPAP.

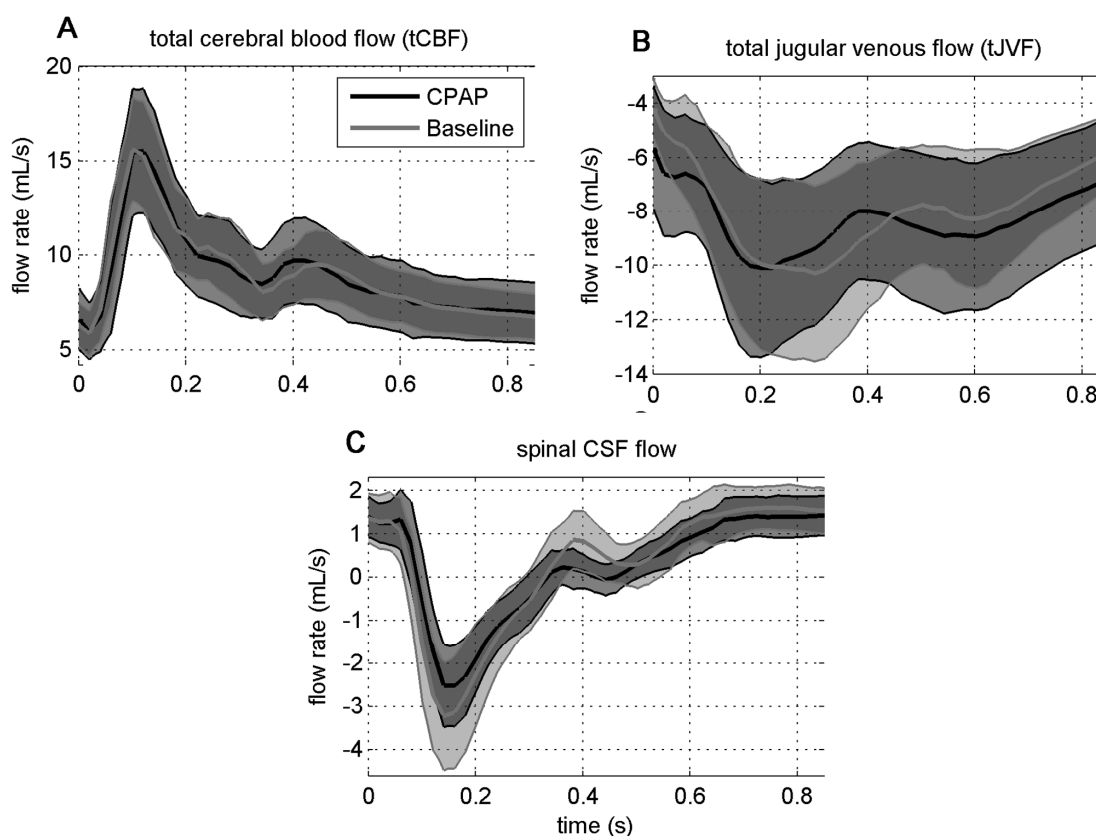


Figure 5.2. Volumetric flow rates for the tCBF (A), tJVF (B) and spinal CSF flow (C). The results are depicted as a mean (bold line) of the included subjects with CPAP (black) and without (gray, baseline) CPAP applied. The shaded area shows the corresponding standard deviation (SD).

5.4.3 Waveform characteristics

Differences of the waveform characteristics between the baseline measurements and with CPAP were analyzed using repeated measures ANOVA. The amplitude of the normalized tCBF ($p = 0.004$), the temporal locations of the tJVF ($p = 0.004$) and the feature points of the spinal CSF flow ($p = 0.034$) showed that these parameters were significantly different under the presence of CPAP compared to the baseline measurements (Figure 5.3). The Mann-Whitney U test of the feature points of the three compartments found the following significant differences: In the tJVF (Figure 5.3B), feature points v2 and v3 of the measurements with CPAP occurred significantly earlier in the cardiac cycle, as did s3 and s4 of the spinal CSF flow (Figure 5.3C). In contrast, the timing of systolic maximum (a2) of the tCBF was delayed with CPAP application (Figure 5.3A). Additionally, v4 of tJVF, s1, s3 and s4 feature points of the spinal CSF flow were found to have significant amplitude differences between the two groups with CPAP and baseline measurements. The corresponding p-values are listed in Figure 5.3. Several feature points of the normalized flow rates were significantly correlated with the HR: in particular, for the case of tCBF (Figure 5.2A), the timing of the aortic valve closure ($r = -0.588$ and $p < 0.001$) and diastolic maximum ($r = -0.346$ and $p = 0.041$), for the case of the tJVF (Figure 5.2B), the amplitude of v1 ($r = -0.433$ and $p = 0.015$) and timing of v3 ($r = -0.453$ and $p = 0.011$) and v4 ($r = -0.456$ and $p = 0.008$). Lastly, for the case of the spinal CSF flow (Figure 5.3C), the amplitude of s1 ($r = 0.306$ and $p = 0.041$), the timing of s3 ($r = -0.426$ and $p = 0.004$) and s4 ($r = -0.530$ and $p < 0.001$).

Frequency components of the normalized flow rates with CPAP were juxtaposed to those of the ones during the baseline measurements as shown in Figure 5.4. Significant differences in individual frequency components according to the Mann-Whitney U test are marked with curly brackets and the respective p-values are indicated in Figure 5.4. Intra- and inter-subjects effects were evaluated by repeated measures ANOVA. The frequency components of the tCBF (Figure 5.4A), the tJVF (Figure 5.4B) and the CSF flow (Figure 5.4C) were significantly different within the groups with $p = 0.001$, $p < 0.001$ and $p = 0.001$, respectively. The differences between the frequency components of the CPAP and those without were only significant in the case of tJVF ($p = 0.036$).

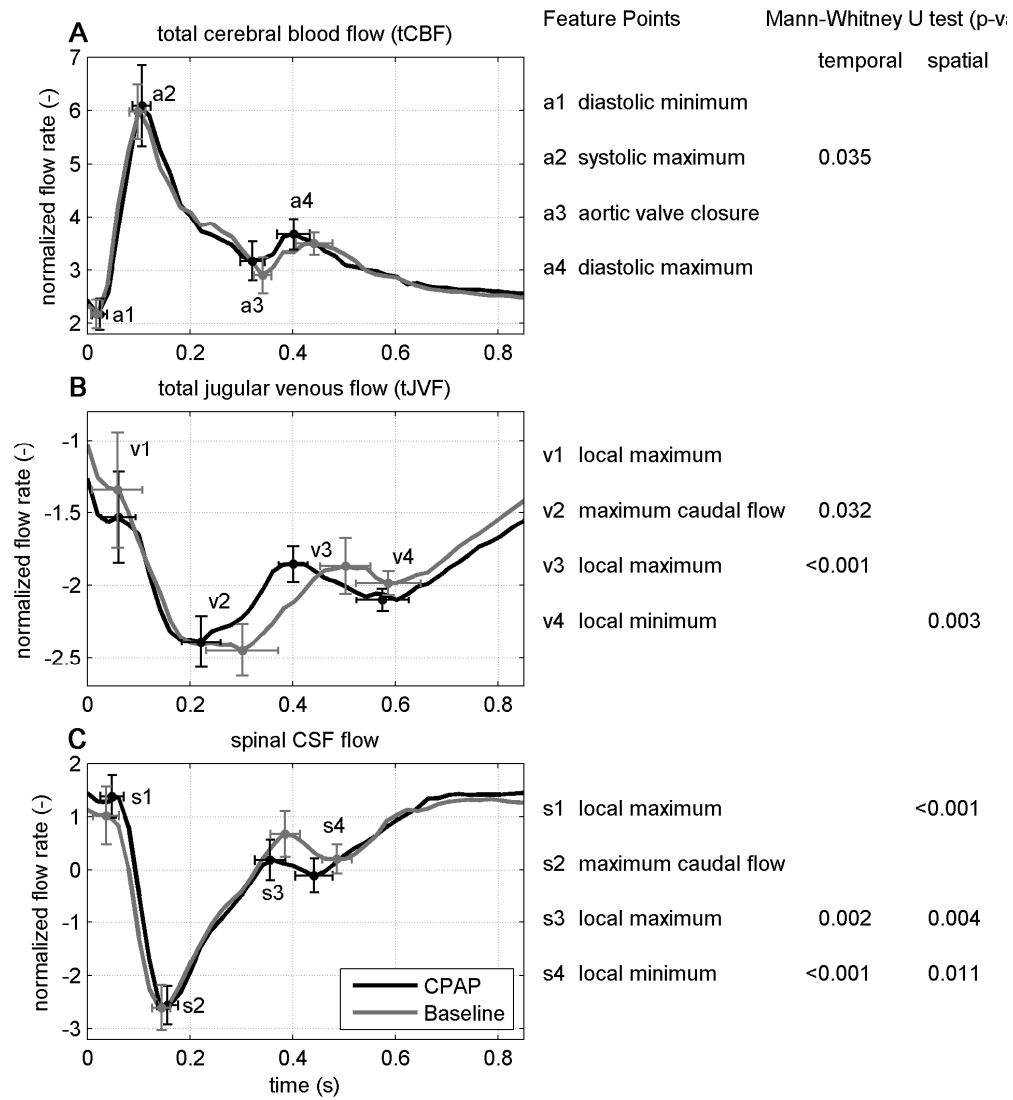


Figure 5.3. Normalized flow rates of the tCBF (**A**), tJVF (**B**) and spinal CSF flow (**C**). The results are depicted as a mean of the included subjects with (black) and without (gray, baseline) CPAP. Feature points are marked with the corresponding standard deviation (SD) error bars with respect to timing and flow deviations. Panel **A** shows the sum of mean (over subjects) normalized flow velocity curves in the left and right ICAs and the left and right VAs that corresponds to the tCBF. Panel **B** depicts the sum of the mean in the left and right JVs that corresponds to the tJVF. Panel **C** depicts the mean CSF flow. Positive values correspond to flow in caudocranial direction. At the right of the panels, the corresponding waveform feature points are described including the p-values evaluated with the Mann-Whitney test regarding the temporal and spatial deviations.

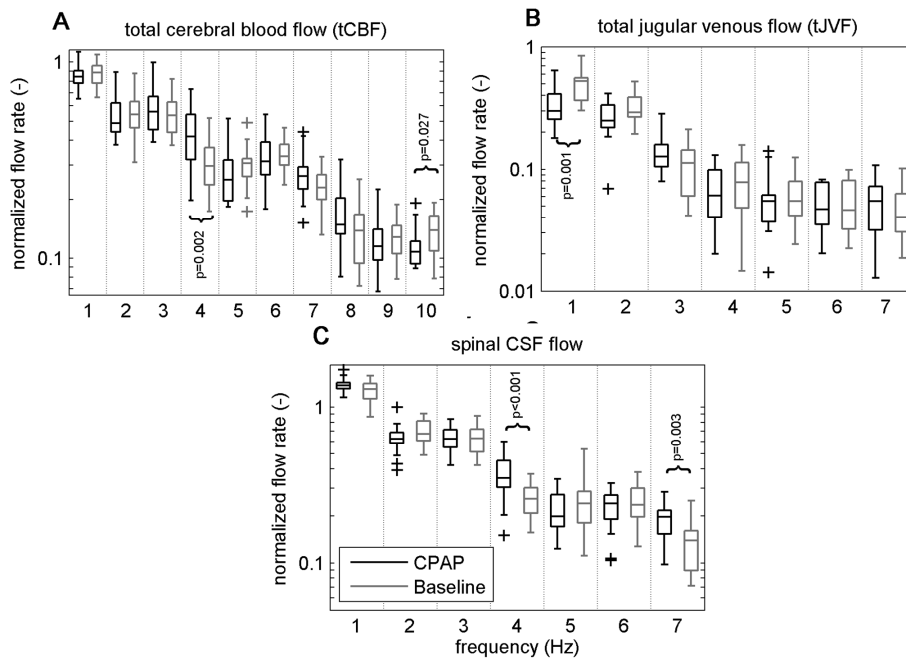


Figure 5.4. Juxtaposed frequency components (Hz) of normalized flow rates with CPAP (black, left) and at Baseline (gray, right) are illustrated using Box plots. In each panel, dotted lines separate the frequency components. In panel **A**, the first to the tenth frequency component of the tCBF are plotted. In panel **B**, the first to the seventh frequency component of the tJVF and in panel **C**, the first to the seventh frequency component of the CSF flow rate are illustrated. Curly brackets indicate significant differences of the respective frequency component's magnitudes analyzed with the Mann-Whitney test.

5.5 Discussion

In the present study, we observed the response of intracranial cerebral blood flow and spinal CSF flow dynamics to the application of CPAP at 15 cmH₂O in healthy male subjects with the use of 2D PC MRI flow measurement protocol. Our hypothesis was that CPAP would decrease the SV and pulse amplitude of CSF flow and would alter venous flow patterns. Our findings validated this hypothesis because CPAP was found to reduced CSF SV and PtPPA by 20% ($p=0.003$) and 15% ($p=0.005$), respectively. In addition, tJVF PtPPA decreased by 21% ($p=0.004$). However, flow based metrics of tCBF were not altered by CPAP. Additionally, normalized tJVF and CSF flow waveforms investigated with respect to their feature points showed significant spatial and temporal differences.

In the past, various studies have employed both transcranial Doppler ultrasound and 2D PC MRI measurements to estimate the effect of CPAP on cerebral and CSF hydrodynamics with conflicting results. In previous work by our group²⁸, we used Duplex color ultrasound to assess the change in tCBF under CPAP at 15 cmH₂O in healthy volunteers. Results showed a significant reduction in the tCBF likely related to hypocapnic vasoconstriction. Kolbitsch et al.³² found that systolic CSF velocity at the aqueduct of Sylvius decreased under CPAP. They reasoned that pressure transmission from the thorax to the craniospinal space increased the spinal CSF pressure, which resulted in an increase of the outflow resistance against the systolic CSF moving into the spinal subarachnoid space thereby decreasing the CSF pulsation at the aqueduct. In a subsequent study Kolbitsch et al.¹⁸⁵ documented a significant decrease in the regional CBF volume with the presence of CPAP at 12 cmH₂O using contrast-enhanced MRI measurements.

The physiological mechanisms responsible for alterations to vascular and CSF flow dynamics under CPAP are complex. A CPAP-induced increase in the intrathoracic pressure may have several hemodynamic effects, such as an increased cardiac output and venous return and increased cerebral venous pressure. Any of these factors could result in a decreased cerebral perfusion pressure²⁸. On the other hand, it is well accepted that PtcCO₂ impacts the muscular regulation of the vessel wall, with hypercapnia leading to

vasodilatation and hypocapnia to vasoconstriction^{186, 187}. Kolbitsch et al.¹⁸⁸ observed an increase of the systolic CSF velocity in the presence of CPAP due to hypercapnia when compared to normocapnia caused by a decreased outflow resistance for a systolic craniospinal CSF displacement. In a previous study, we also reported a reduction in the tCBF, but this effect appeared to be mediated predominately through the hypocapnic vasoconstriction coinciding with PtcCO₂ level reduction²⁸. In the present study, we also observed a significant reduction in the PtcCO₂ and HR. However, these alterations were not significantly correlated with any of the arterial, jugular or spinal CSF flow changes under CPAP. As a result, our present findings support that the observed changes in the tJVF and CSF dynamics are likely mediated by CPAP pressure acting on the lungs.

Increased intrathoracic pressure due to CPAP tends to elevate the pressure in the jugular vein, decreasing the arterio-venous pressure gradient across the brain. There are different theories that explain the transmission pathways of the intrathoracic pressure to the intracranial space. The pressure is transmitted not only through the JV, but also through longitudinal vertebral veins situated inside the vertebral column. A major part of the intrathoracic pressure is also transmitted to the thoracic spinal subarachnoid space via the thoracic intervertebral foramina³². Luce et al.¹⁸⁹ found an increase in ICP during positive end-expiratory pressure (PEEP) conditions that primarily resulted from an increased pressure in the superior vena cava and impeded the cerebral venous outflow. In this study, we were only able to measure flow through the JV since the structure and function of the overall cerebral venous system are difficult to be captured with the current imaging techniques and as a result there are only limited data published. ElSankari et al.¹⁷⁷ recently documented complex and heterogenous intracranial venous drainage pathways that did not differ between multiple sclerosis patients and healthy subjects. Additionally, it has been postulated that a reduction in the pulsatility of tJVF could cause an increased pressure in the spinal subarachnoid space, which is compensated by an increase in the CSF flow in the spinal subarachnoid space. In a second phase, these compensatory mechanisms are exceeded, which results in reduced flows and velocities in the spinal subarachnoid space¹⁷⁶. It is well established then, that any disruption in the balance of the intracranial space components alters the ability of spinal subarachnoid space to dampen tCBF pulsations. In analogy, an obstruction to CSF flow could decrease as well the damping effect on tCBF pulsations¹⁷⁴. A reduction in damping of the tCBF pulsations would in turn result in abnormal biomechanical forces acting within the craniospinal, arterial or venous system. Hence, the decrease we observed in the SV and pulse amplitude of both CSF and tJVF are in agreement with theories in the literature that the spinal subarachnoid space of the CSF system may act to dampen CBF pulsations^{4, 5}.

The feature points of the tCBF, tJVF and spinal CSF flow waveforms were found to be influenced under the presence of CPAP. In particular, the timing of the maximum caudal flow of the tJVF occurred earlier in the cardiac cycle under CPAP. Because this feature point did not correlate with the HR, its timing is related only to the effect of CPAP. The delay of the tCBF systolic maximum due to CPAP is possibly caused by the increase in the intrathoracic pressure accompanied by an increased resistance during the cardiac output. Most amplitudes of the spinal CSF flow feature points with CPAP differed significantly from those without. Additionally, the flow pattern of the normalized spinal CSF flow showed a behavior comparable to what we reported in an earlier study on the physiological difference between age groups in the same compartment¹⁸⁴. In analogy, the diastolic timings and amplitudes of the elderly male volunteers that were reported in our previous study correspond to the current CPAP group results.

The spectral content of the normalized tCBF only varies significantly in the fourth and the tenth frequency component. The effect of CPAP on the main arterial vessels of healthy young males appears therefore small. In the spinal canal, the fourth and the seventh frequency component of the CSF flow were significantly different with the presence of CPAP. The fundamental frequency of the tJVF was significantly decreased with CPAP, a finding that is related to the decreased tJVF SV. Generally, the influence of CPAP appears to be more significant in the tJVF: the repeated measures ANOVA between the measurements with CPAP and those without were significantly different for the temporal locations of the respective feature points and the tJVF frequency content.

Limitations

Using prospectively triggered image sequences, the acquisition window had to be set 10–20% below the average cycle length. Therefore, only 80–90% of the entire cardiac cycle was covered and was available for data analysis. Due to the fact that no data was recorded for the remaining 10–20% of the cardiac cycle, the diastolic phase is underestimated¹⁹⁰. Venous flow was approximated through the left and right JV. Few studies have measured cerebral venous flow because of the difficulty to image the complex venous structure with the available techniques¹⁹¹. Furthermore, the venous system has been mainly studied in pathologic conditions such as cerebral venous thrombosis or multiple sclerosis. Thus, there are no sufficient data to compare with the physiological states. We chose to adjust the CPAP level to 15 cmH₂O in order to emphasize the maximum physiological effects of CPAP on vascular and CSF flow dynamics by minimizing possible bias. It is possible that this high pressure could have resulted in substantial air-leaks and caused a gap between the applied and delivered mask pressure and subsequently increased subject discomfort. However, during the 2D PC MR measurements of our study the presence of air-leaks was repeatedly assessed by a medical doctor and adjusted when needed. Furthermore, all volunteers were asked to rate their anxiety level due to CPAP and 70% of the subjects tolerated the CPAP well without any difficulties.

In conclusion, our findings suggest CPAP has a direct and significant effect on spinal CSF flow and intracranial venous outflow and affects the overall intracranial equilibrium that normally exists between the arterial, venous, CSF flow and brain tissue. These findings were determined by the use of 2D PC MRI to quantify the alterations in the tCBF, tJVF and spinal CSF flow due to the increased thoracic pressure caused by CPAP at 15 cmH₂O. The results demonstrate a decrease in the SV of CSF and PtPPA of both CSF flow and tJVF at the craniocervical junction. Additionally, the timing of the maximum caudal flow of the tJVF was markedly decreased. These alterations are mainly attributed to the direct influence of the CPAP application on the intrathoracic pressure and are not correlated with the reduction in the PtcCO₂ level that was measured.

6. Conclusions

6.1 Main findings

The research studies that have been conducted in the present thesis have helped to assess and simulate the CSF dynamics and measure the cranial blood flow field. This was implemented by 1) computationally simulating the CSF flow field in the upper cervical spine with the use of subject-specific 3D CFD simulations and comparing it with 4D PC MRI measurements obtained at the same subjects and 2) experimentally assessing the spinal CSF flow and CBF in healthy volunteers with the use of MRI and US under normal conditions and with the application of CPAP.

In Chapter 2, we compared for the first time 4D PC MRI measurements to 3D rigid-wall subject-specific CFD simulations of the CSF motion in the cervical SSS of three healthy subjects and four CMI patients. Results were analyzed in terms of peak flow velocities in the craniocaudal direction and thru-plane velocity profiles at nine axial levels of the cervical spine. 4D PC MRI peak CSF velocities were found to be consistently greater than the CFD peak velocities and these differences were more pronounced in CMI patients than in healthy subjects. In addition to this, 4D PC MRI thru-plane velocity profiles showed greater pulsatile movement of CSF in the anterior SSS in comparison to the posterior and reduction in local CSF velocities near nerve roots. On the other hand, CFD velocity profiles were relatively uniform around the SC for all subjects. The results of this research study do underline the utility of CFD in conjunction with 4D PC MRI for detailed analysis of CSF flow dynamics that could help distinguish physiological from complex pathological flow patterns at the FM and cervical SSS.

In Chapter 3, we evaluated for the first time the inter-operator dependence of MRI-based CFD modeling of CSF movement in the cervical spine. The same geometry of a control was reconstructed by seven independent operators. Comparison of the CFD results was performed in terms of several geometric and hydrodynamic parameters as well as the thru-plane velocity profiles at peak systole. Our findings showed a small operator dependence of the image processing and reconstruction of the 3D geometry of the healthy volunteer implying very good agreement between the operators (ICC>0.90 for all the parameters). Greater values of CV~17-19% for all parameters were observed at the lower cervical spine while lower values of CV ~ 2-5% were found towards the cranial end, near the FM-C2M regions. Thus, the presented segmentation process and CFD methodology shows promise to be used as a tool to analyze the CSF flow field patterns in the cervical spine based on MRI measurements and to identify parameters indicative of disease states that could aid in the diagnosis of craniospinal disorders.

In Chapter 4, we used duplex color Doppler ultrasound measurements on 23 healthy awake volunteers as a noninvasive bedside method to assess the effect of CPAP 15 cmH₂O on total CBF by incorporating flow velocity and lumen diameter measurements obtained at the left and right ICAs, VAs, and MCAs, while PtcCO₂, SaO₂, HR and BP were monitored continuously. This was a primary study to understand the impact of CPAP on CBF system that could help us further on Chapter 5 to measure CSF flow and investigate the impact of CPAP on CSF dynamics. Our results showed that CPAP at 15 cmH₂O significantly decreased total CBF in all subjects. This effect appeared to be mediated predominately through the hypocapnic vasoconstriction coinciding with reduction in PtcCO₂ level reduction. Our findings suggest that CPAP should be used cautiously in patients with unstable cerebral hemodynamics.

In Chapter 5 we extended our results from Chapter 4 by conducting an additional study where we developed a specific MRI protocol to assess the impact of CPAP on cerebral hemodynamics and CSF dynamics in the upper cervical spine. We obtained 2D PC MRI measurements at the left and right ICAs, VAs, JVs and SSS at the C2-C3 cervical vertebrae level on 23 healthy subjects with and without CPAP while again PtcCO₂, SaO₂ and HR were monitored continuously. Our results showed a decrease in the pulse amplitude of both spinal CSF flow and tJVF at the craniocervical junction. No significant changes were observed in the tCBF hemodynamics. Spectrum analysis of the flow waveforms revealed the timing of the maximum caudal flow of the tJVF to be noticeable decreased. CSF and tJVF waveforms showed as well significant spatial and temporal differences with the presence of CPAP. Our findings suggest CPAP has a direct and significant effect on intracranial and spinal CSF flow on healthy individuals and affects the

overall intracranial equilibrium that normally exists between the arterial, venous, CSF flow and brain tissue.

6.2 Future perspectives

Careful measurement and modelling of the CSF hydrodynamics in healthy subjects, and more importantly in patients with craniospinal disorders, undoubtedly offers potential for better understanding of pathophysiology of those disorders and clinical utility. In this thesis, CSF hydrodynamic environment in the craniospinal system was both measured using *in vivo* MRI flow measurements and modeled using CFD simulations. The CBF hydrodynamic environment was also measured and characterized *in vivo*.

A number of assumptions are present in the thesis at hand that could further ameliorated and analyzed in the future. For instance, in Chapter 4 small anatomical structures were not taken into consideration in the CFD models. Incorporation of the spinal cord nerve roots and denticulate ligaments in the existing CFD model would be the first step to use as much as possible realistic models of the spinal anatomy. This has already been accomplished in a recent study of our group. In particular, it was found that the presence of nerve roots and denticulate ligaments within the upper cervical spine had an important impact on CSF dynamics in terms of velocity field and flow patterns (Figure 6.1)¹²⁰. However, pressure gradients were not altered to a great degree. In addition, velocity-based parameters were little impacted near the foramen magnum because the spinal cord nerve roots and denticulate ligaments are not present near this location.

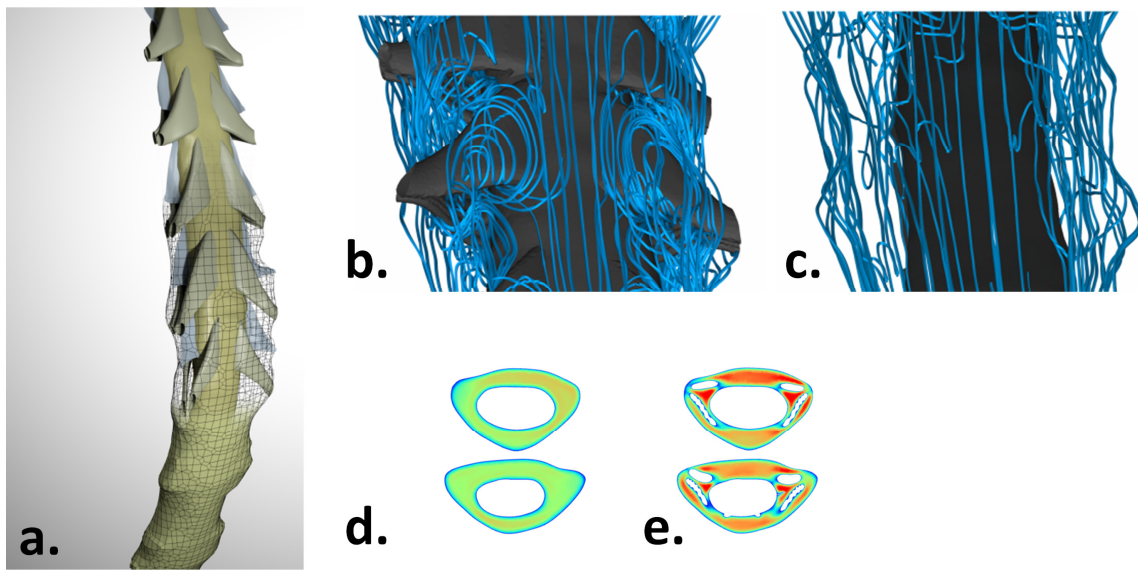


Figure 6.1 a. Rendering of the 3D geometry of the cervical SSS of a healthy subject containing idealized nerve roots and denticulate ligaments (in light green). The mesh indicates boundary of the dura. Streamlines plots for healthy case with fine structures in **b** and without fine structures in **c**. Velocity magnitude contours at C5 and C6 of the cervical SSS plotted at peak systole a for healthy case without in **d** and with fine structures in **e**, respectively¹²⁰.

In addition to this, the CFD models with the incorporation of fine structures should be compared to *in vivo* 4D PC MRI measurements. This is something that our group has already started investigating. Results have reported that the comparison between the two methodologies showed high level of spatial and temporal complexity of the CSF flow field in the cervical spine (Figure 6.2). On a later stage, arachnoid trabeculae and other small anatomical structures within the SSS should be included in the CFD models as well. One more parameter that should be taken into consideration in future studies would be the importance of tissue motion on CSF dynamics because it has been observed that the spinal cord moves a small but detectable amount during the CSF pulsation at a peak velocity of 0.7-1.2 cm/s^{15, 192}. It has been

documented in the literature that both patients with CMI and controls depicted a small-amplitude tonsil movement in cephalad and caudal directions during the cardiac cycle¹⁹³.

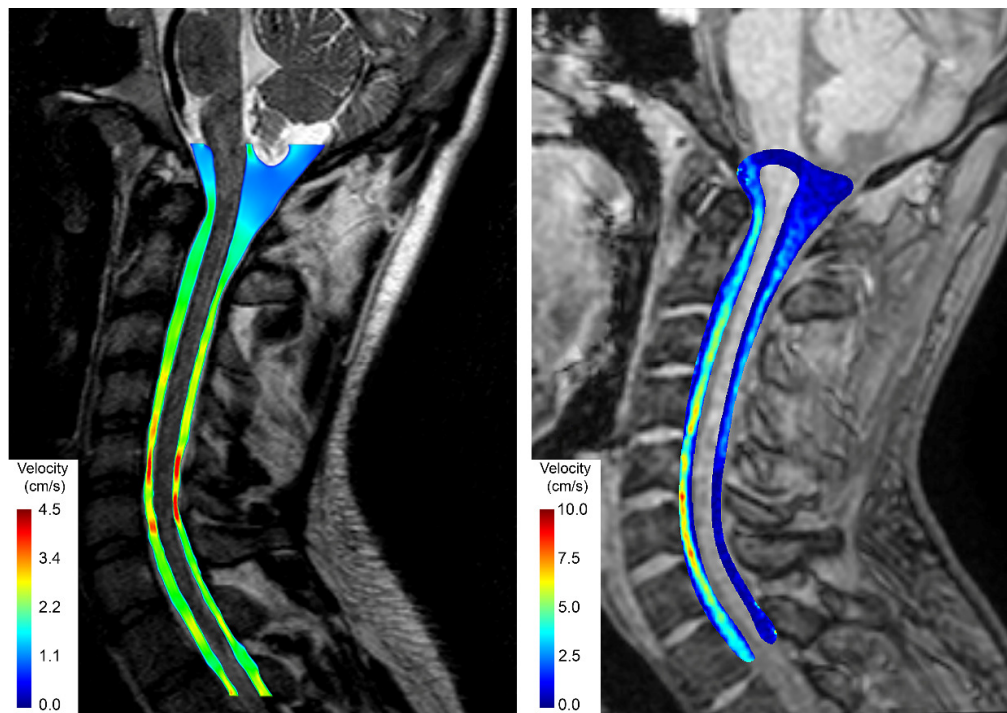


Figure 6.2 Distribution of mid-sagittal peak systolic velocity magnitude for a control obtained from CFD (left) and 4D PCMRI (right).(work currently under review in American Journal of Neuroradiology).

Finally, 4D PC MRI measurements in an *in vitro* model where these small anatomical structures are included could help better explain the differences in the CSF flow fields between the 4D PC MRI measurements and the CFD modeling. Our group has already successfully constructed a prototype 3D *in vitro* model of the cervical spine. The 3D anatomy of the cervical SSS containing the dura matter layer and spinal cord was reconstructed from T2-weighted MRI images by manual segmentation. The idealized nerve roots were created at each axial level along the spine based on measurements reported in the literature¹⁹⁴. Thus, our group aims at measuring the 3D velocity field within four subject-specific *in vitro* models of SSS, of a healthy volunteer with and without spinal cord nerve roots and a Chiari I malformation patient with and without spinal cord nerve roots with 4D PC MRI protocols in different MRI machines and comparing it with 3D CFD simulations based on the same geometries and boundary conditions.

In Chapter 3, we compared the CFD results between the geometries that were segmented by the 7 independent operators and not with “gold standard” geometry of the SSS. This is an approach that has mainly been used in hemodynamic studies¹¹. Our group will use in the future the *in vitro* model of the cervical spine that was just described above as a “gold standard model” to compare further results from CFD simulations. Another approach would be to utilize images of higher resolution, obtained with 7T MRI that would help better define the geometric boundaries and the fine anatomical structures that are difficult to be defined with the current imaging techniques¹³⁶. One more constriction of Chapter 3 was that the CFD models and resulting analysis were based on the geometry of a healthy subject. Patients with craniospinal disorders such as CMI, often have restricted CSF spaces with smaller areas which makes difficult the reconstruction of the geometry with manual segmentation. Thus, the resulting variance of the geometric and hydrodynamic parameters could be greater in the patient case. Towards this end, two independent operators from our group have segmented the same geometry of a symptomatic Chiari I patient so as to estimate the inter-operator dependence of the CFD methodology for the patient case. Preliminary comparison of the cross-sectional areas and peak CSF velocities (Figure 6.3) obtained from the CFD simulations based on the two operators shows a maximum CV $\sim 22\%$ for both parameters at the lower cervical spine (e.g axial location C7). However, further analysis is required to assess the operator

dependence of the CFD simulations of the CSF flow in the cervical spine of a Chiari I symptomatic patient with more operators.

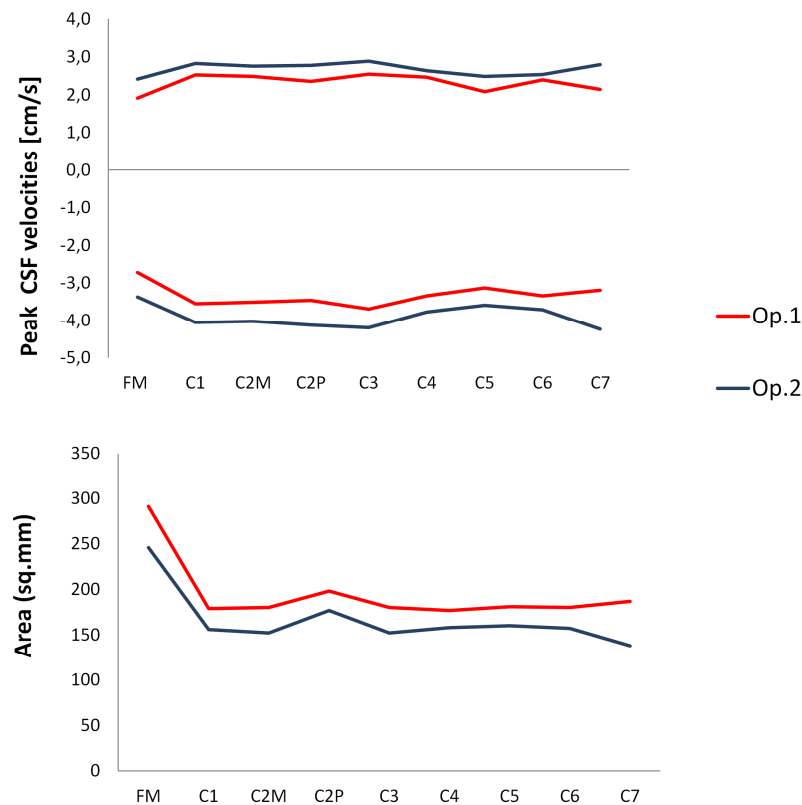


Figure 6.3 Peak systolic and diastolic velocities (**top**) at each axial location obtained from the CFD simulations based on the two operators (Op.1-Op.2). Positive (diastolic) and negative (systolic) velocities reflect head and foot directed flow, respectively. Cross-sectional areas (**bottom**) at each axial plane of the cervical SSS for the two operators.

In Chapter 4, we were not able to conclude if CPAP pressure had a direct impact on total CBF. The decrease in CBF that was observed was mediated predominately through the hypocapnic vasoconstriction, while in Chapter 5 CPAP was found to have a direct effect on intrathoracic pressure, CSF and venous hemodynamics. As CPAP use is becoming more widespread, we believe that a better understanding of its physiological impact is important to help improve the technology and also understand the full impact of its use in different patient groups such as traumatic brain injury, stroke and sleep apnea. Decrease in total CBF due to CPAP usage could have important clinical implications as CPAP is a commonly used device for those patient groups. In these patients, careful consideration of cerebral perfusion is needed. Thus, one potential future step could be to examine the impact of CPAP pressure on CBF in stroke patients to validate these conjectures. In addition, since the published data concerning the impact CPAP on CBF and CSF flow dynamics are conflicting, a study would need to be conducted with the PtcCO₂ level held constant while CPAP pressure is altered incrementally.

In Chapter 5, we observed CPAP to alter the CSF and jugular venous flow dynamics in healthy awake volunteers with the use of 2D PC MRI. However, venous flow was approximated by measuring the flow through the left and right JV. The reason for this assumption was that there are only few studies in the literature that have measured overall cerebral venous flow because of the difficulty to image the complex venous structure with the current imaging techniques¹⁹¹. Furthermore, the venous system has been mainly studied in pathologic conditions such as cerebral venous thrombosis or multiple sclerosis and not

in physiological states. Thus, in the future the overall cerebral venous flow system should be taken into consideration. Another limitation of Chapter 5 that should be taken into account in the future was that only 80–90% of the entire cardiac cycle was covered and was available for data due to the prospective gating of the images. However, it is documented that prospective gating results in underestimation of the diastolic phase of the cardiac cycle¹⁹⁰. Since, the gating method in MR imaging has an impact on the objectivity of the measurements, in the future retrospective gating should be preferred during the MR data acquisition.

Finally, in both Chapters 4 and 5 we chose to use CPAP as method to non-invasively establish the impact of the breathing machine on CSF and CBF system dynamics. Another way to non-invasively alter intrathoracic pressure is with Queckenstedt's test and pressure in the abdomen. Communication between intrathoracic pressure and ICP has been documented during those experiments^{40, 41, 77}. Thus, one possibility in the future could be to conduct an MRI study in healthy subjects and patients with unstable cerebral dynamics and/or craniospinal disorders where we examine the impact of Queckenstedt's test and/or pressure in the abdomen on arterial, venous and CSF flow dynamics.

References

1. Stoodley MA, Brown SA, Brown CJ, Jones NR. Arterial pulsation-dependent perivascular cerebrospinal fluid flow into the central canal in the sheep spinal cord. *J Neurosurg.* 1997;86:686-693
2. Bilston LE, Fletcher DF, Brodbelt AR, Stoodley MA. Arterial pulsation-driven cerebrospinal fluid flow in the perivascular space: A computational model. *Comp Methods Biomec.* 2003;6:235 - 241
3. Bilston LE, Stoodley MA, Fletcher DF. The influence of the relative timing of arterial and subarachnoid space pulse waves on spinal perivascular cerebrospinal fluid flow as a possible factor in syrinx development. *J Neurosurg.* 2009
4. Luciano M, Dombrowski S. Hydrocephalus and the heart: Interactions of the first and third circulations. *Cleve Clin J Med.* 2007;74 Suppl 1:S128-131
5. Madsen JR, Egnor M, Zou R. Cerebrospinal fluid pulsatility and hydrocephalus: The fourth circulation. *Clin Neurosurg.* 2006;53:48-52
6. Wiswell TE, Tuttle DJ, Northam RS, Simonds GR. Major congenital neurologic malformations. A 17-year survey. *Am J Dis Child.* 1990;144:61-67
7. Tubbs RS, Bailey M, Barrow WC, Loukas M, Shoja MM, Oakes WJ. Morphometric analysis of the craniocervical juncture in children with chiari i malformation and concomitant syringobulbia. *Child Nerv Syst.* 2009;25:689-692
8. Bunck AC, Kroeger JR, Juettner A, Brentrup A, Fiedler B, Crelier GR, Martin BA, Heindel W, Maintz D, Schwindt W, Niederstadt T. Magnetic resonance 4d flow analysis of cerebrospinal fluid dynamics in chiari i malformation with and without syringomyelia. *Eur Radiol.* 2012;22:1860-1870
9. Houghton VM, Korosec FR, Medow JE, Dolar MT, Iskandar BJ. Peak systolic and diastolic csf velocity in the foramen magnum in adult patients with chiari i malformations and in normal control participants. *AJNR Am J Neuroradiol.* 2003;24:169-176
10. Quigley MF, Iskandar B, Quigley ME, Nicosia M, Houghton V. Cerebrospinal fluid flow in foramen magnum: Temporal and spatial patterns at mr imaging in volunteers and in patients with chiari i malformation. *Radiology.* 2004;232:229-236
11. Moore JA, Steinman DA, Holdsworth DW, Ethier CR. Accuracy of computational hemodynamics in complex arterial geometries reconstructed from magnetic resonance imaging. *Ann Biomed Eng.* 1999;27:32-41
12. Greitz D, Wirestam R, Franck A, Nordell B, Thomsen C, Stahlberg F. Pulsatile brain movement and associated hydrodynamics studied by magnetic-resonance phase imaging - the monro-kellie doctrine revisited. *Neuroradiology.* 1992;34:370-380
13. Feinberg DA, Mark AS. Human-brain motion and cerebrospinal-fluid circulation demonstrated with mr velocity imaging. *Radiology.* 1987;163:793-799
14. Enzmann DR, Pelc NJ. Cerebrospinal-fluid flow measured by phase-contrast cine mr. *Am J Neuroradiol.* 1993;14:1301-1307
15. Alperin N, Vikingstad EM, GomezAnson B, Levin DN. Hemodynamically independent analysis of cerebrospinal fluid and brain motion observed with dynamic phase contrast mri. *Magnetic Resonance in Medicine.* 1996;35:741-754
16. Iskandar BJ, Quigley M, Houghton VM. Foramen magnum cerebrospinal fluid flow characteristics in children with chiari i malformation before and after craniocervical decompression. *J Neurosurg.* 2004;101:169-178
17. Stadlbauer A, Salomonowitz E, van der Riet W, Buchfelder M, Ganslandt O. Insight into the patterns of cerebrospinal fluid flow in the human ventricular system using mr velocity mapping. *Neuroimage.* 2010;51:42-52
18. Bunck AC, Kroger JR, Juttner A, Brentrup A, Fiedler B, Schaarschmidt F, Crelier GR, Schwindt W, Heindel W, Niederstadt T, Maintz D. Magnetic resonance 4d flow characteristics of cerebrospinal fluid at the craniocervical junction and the cervical spinal canal. *Eur Radiol.* 2011;21:1788-1796
19. McGirt MJ, Atiba A, Attenello FJ, Wasserman BA, Datto G, Gathinji M, Carson B, Weingart JD, Jallo GI. Correlation of hindbrain csf flow and outcome after surgical decompression for chiari i malformation. *Childs Nerv Syst.* 2008;24:833-840

20. McGirt MJ, Nimjee SM, Fuchs HE, George TM. Relationship of cine phase-contrast magnetic resonance imaging with outcome after decompression for chiari i malformations. *Neurosurgery*. 2006;59:140-146; discussion 140-146
21. Belkora JK, Teng A, Volz S, Loth MK, Esserman LJ. Expanding the reach of decision and communication aids in a breast care center: A quality improvement study. *Patient Educ Couns*. 2011;83:234-239
22. Kurtcuoglu V, Poulikakos D, Ventikos Y. Computational modeling of the mechanical behavior of the cerebrospinal fluid system. *J Biomech Eng-T Asme*. 2005;127:264-269
23. Kurtcuoglu V, Soellinger M, Summers P, Boomsma K, Poulikakos D, Boesiger P, Ventikos Y. Computational investigation of subject-specific cerebrospinal fluid flow in the third ventricle and aqueduct of sylvius. *J Biomech*. 2007;40:1235-1245
24. Cirignotta F, Coccagna G, Zucconi M, Gerardi R, Lugaresi A, Cortelli P, Tralli G, Lugaresi E. Sleep apneas, convulsive syncopes and autonomic impairment in type i arnold-chiari malformation. *Eur Neurol*. 1991;31:36-40
25. Shiihara T, Shimizu Y, Mitsui T, Saitoh E, Sato S. Isolated sleep apnea due to chiari type i malformation and syringomyelia. *Pediatr Neurol*. 1995;13:266-267
26. Haring HP, Hormann C, Schalow S, Benzer A. Continuous positive airway pressure breathing increases cerebral blood flow velocity in humans. *Anesth Analg*. 1994;79:883-885
27. Bowie RA, O'Connor PJ, Hardman JG, Mahajan RP. The effect of continuous positive airway pressure on cerebral blood flow velocity in awake volunteers. *Anesth Analg*. 2001;92:415-417
28. Yiallourou T, Odier C, Heinzer R, Hirt L, Martin B, Stergiopoulos N, Haba-Rubio J. The effect of continuous positive airway pressure on total cerebral blood flow in healthy awake volunteers. *Sleep Breath*. 2012;1-8
29. Becker H, Grote L, Ploch T, Schneider H, Stammnitz A, Peter JH, Podszus T. Intrathoracic pressure changes and cardiovascular effects induced by ncpap and nbipap in sleep apnoea patients. *J Sleep Res*. 1995;4:125-129
30. Feldman Z, Robertson CS, Contant CF, Gopinath SP, Grossman RG. Positive end expiratory pressure reduces intracranial compliance in the rabbit. *J Neurosurg Anesthesiol*. 1997;9:175-179
31. Hormann C, Mohsenipour I, Gottardis M, Benzer A. Response of cerebrospinal fluid pressure to continuous positive airway pressure in volunteers. *Anesth Analg*. 1994;78:54-57
32. Kolbitsch C, Schocke M, Lorenz IH, Kremser C, Zschiegner F, Pfeiffer KP, Felber S, Aichner F, Hormann C, Benzer A. Phase-contrast mri measurement of systolic cerebrospinal fluid peak velocity (csfv(peak)) in the aqueduct of sylvius: A noninvasive tool for measurement of cerebral capacity. *Anesthesiology*. 1999;90:1546-1550
33. Mokri B. The monro-kellie hypothesis: Applications in csf volume depletion. *Neurology*. 2001;56:1746-1748
34. Bradbury MW. The blood-brain barrier. Transport across the cerebral endothelium. *Circ Res*. 1985;57:213-222
35. Albeck MJ, Borgeesen SE, Gjerris F, Schmidt JF, Sorensen PS. Intracranial pressure and cerebrospinal fluid outflow conductance in healthy subjects. *J Neurosurg*. 1991;74:597-600
36. Stockman HW. Effect of anatomical fine structure on the dispersion of solutes in the spinal subarachnoid space. *J Biomech Eng*. 2007;129:666-675
37. Cloyd MW, Low FN. Scanning electron microscopy of the subarachnoid space in the dog. I. Spinal cord levels. *J Comp Neurol*. 1974;153:325-368
38. Condon B, Patterson J, Wyper D, Hadley D, Grant R, Teasdale G, Rowan J. Use of magnetic resonance imaging to measure intracranial cerebrospinal fluid volume. *Lancet*. 1986;1:1355-1357
39. Schumacher GMRSS. *Atlas of anatomy* 2012.
40. Conejero CI, Chopard RP. Tridimensional architecture of the collagen element in the arachnoid granulations in humans: A study on scanning electron microscopy. *Arq Neuropsiquiatr*. 2003;61:561-565
41. Greitz D. Unraveling the riddle of syringomyelia. *Neurosurg Rev*. 2006;29:251-263

42. Monro A. *Observations on the structure and functions of the nervous system*. Edinburgh,: Printed for, and sold by, W. Creech; 1783.
43. Loth F, Yardimci MA, Alperin N. Hydrodynamic modeling of cerebrospinal fluid motion within the spinal cavity. *J Biomech Eng*. 2001;123:71-79
44. Dunbar HS, Guthrie TC, Karpell B. A study of the cerebrospinal fluid pulse wave. *Arch Neurol*. 1966;14:624-630
45. Alastruey J, Parker KH, Peiro J, Byrd SM, Sherwin SJ. Modelling the circle of willis to assess the effects of anatomical variations and occlusions on cerebral flows. *J Biomech*. 2007;40:1794-1805
46. Alperin N, Hushek SG, Lee SH, Sivaramakrishnan A, Lichtor T. Mri study of cerebral blood flow and csf flow dynamics in an upright posture: The effect of posture on the intracranial compliance and pressure. *Acta Neurochir Suppl*. 2005;95:177-181
47. Bhadelia RA, Bogdan AR, Kaplan RF, Wolpert SM. Cerebrospinal fluid pulsation amplitude and its quantitative relationship to cerebral blood flow pulsations: A phase-contrast mr flow imaging study. *Neuroradiology*. 1997;39:258-264
48. Baledent O, Gondry-Jouet C, Meyer ME, De Marco G, Le Gars D, Henry-Feugeas MC, Idy-Peretti I. Relationship between cerebrospinal fluid and blood dynamics in healthy volunteers and patients with communicating hydrocephalus. *Invest Radiol*. 2004;39:45-55
49. Baledent O, Henry-Feugeas MC, Idy-Peretti I. Cerebrospinal fluid dynamics and relation with blood flow: A magnetic resonance study with semiautomated cerebrospinal fluid segmentation. *Invest Radiol*. 2001;36:368-377
50. Alperin NJ, Lee SH, Loth F, Raksin PB, Lichtor T. Mr-intracranial pressure (icp): A method to measure intracranial elastance and pressure noninvasively by means of mr imaging: Baboon and human study. *Radiology*. 2000;217:877-885
51. Alperin N, Sivaramakrishnan A, Lichtor T. Magnetic resonance imaging-based measurements of cerebrospinal fluid and blood flow as indicators of intracranial compliance in patients with chiari malformation. *J Neurosurg*. 2005;103:46-52
52. Zou R, Park EH, Kelly EM, Egnor M, Wagshul ME, Madsen JR. Intracranial pressure waves: Characterization of a pulsation absorber with notch filter properties using systems analysis: Laboratory investigation. *J Neurosurg Pediatr*. 2008;2:83-94
53. Czosnyka M, Pickard JD. Monitoring and interpretation of intracranial pressure. *J Neurol Neurosurg Psychiatry*. 2004;75:813-821
54. Williams B. Simultaneous cerebral and spinal fluid pressure recordings. 2. Cerebrospinal dissociation with lesions at the foramen magnum. *Acta Neurochir (Wien)*. 1981;59:123-142
55. Williams B. Simultaneous cerebral and spinal fluid pressure recordings. I. Technique, physiology, and normal results. *Acta Neurochir (Wien)*. 1981;58:167-185
56. Sansur CA, Heiss JD, DeVroom HL, Eskioğlu E, Ennis R, Oldfield EH. Pathophysiology of headache associated with cough in patients with chiari i malformation. *J Neurosurg*. 2003;98:453-458
57. Buda AJ, Pinsky MR, Ingels NB, Jr., Daughters GT, 2nd, Stinson EB, Alderman EL. Effect of intrathoracic pressure on left ventricular performance. *N Engl J Med*. 1979;301:453-459
58. Scala R, Turkington PM, Wanklyn P, Bamford J, Elliott MW. Effects of incremental levels of continuous positive airway pressure on cerebral blood flow velocity in healthy adult humans. *Clin Sci (Lond)*. 2003;104:633-639
59. Markwalder TM, Grolimund P, Seiler RW, Roth F, Aaslid R. Dependency of blood flow velocity in the middle cerebral artery on end-tidal carbon dioxide partial pressure--a transcranial ultrasound doppler study. *J Cereb Blood Flow Metab*. 1984;4:368-372
60. Valdueza JM, Draganski B, Hoffmann O, Dirnagl U, Einhaupl KM. Analysis of co2 vasomotor reactivity and vessel diameter changes by simultaneous venous and arterial doppler recordings. *Stroke*. 1999;30:81-86
61. Eicke BM, Buss E, Bahr RR, Hajak G, Paulus W. Influence of acetazolamide and co2 on extracranial flow volume and intracranial blood flow velocity. *Stroke*. 1999;30:76-80

62. Milhorat TH, Chou MW, Trinidad EM, Kula RW, Mandell M, Wolpert C, Speer MC. Chiari i malformation redefined: Clinical and radiographic findings for 364 symptomatic patients. *Neurosurgery*. 1999;44:1005-1017
63. Bunck AC, Kroger JR, Juttner A, Brentrup A, Fiedler B, Schaarschmidt F, Crelier GR, Schwindt W, Heindel W, Niederstadt T, Maintz D. Magnetic resonance 4d flow characteristics of cerebrospinal fluid at the craniocervical junction and the cervical spinal canal. *Eur Radiol*. 2011;21:1788-1796
64. Shaffer N, Martin BA, Rocque B, Madura C, Wieben O, Iskandar B, Dombrowski S, Luciano M, Oshinski J, Loth F. Cerebrospinal fluid flow impedance is elevated in type i chiari malformation. *J Biomech Eng*. 2013
65. Krueger KD, Haughton VM, Hetzel S. Peak csf velocities in patients with symptomatic and asymptomatic chiari i malformation. *AJNR. American journal of neuroradiology*. 2010;31:1837-1841
66. Wagshul ME, Chen JJ, Egnor MR, McCormack EJ, Roche PE. Amplitude and phase of cerebrospinal fluid pulsations: Experimental studies and review of the literature. *J Neurosurg*. 2006;104:810-819
67. Kalata W, Martin BA, Oshinski JN, Jerosch-Herold M, Royston TJ, Loth F. Mr measurement of cerebrospinal fluid velocity wave speed in the spinal canal. *IEEE Trans Biomed Eng*. 2009;56:1765-1768
68. Roldan A, Wieben O, Haughton V, Osswald T, Chesler N. Characterization of csf hydrodynamics in the presence and absence of tonsillar ectopia by means of computational flow analysis. *AJNR Am J Neuroradiol*. 2009;30:941-946
69. Sweetman B, Linninger AA. Cerebrospinal fluid flow dynamics in the central nervous system. *Annals of biomedical engineering*. 2011;39:484-496
70. Matsumae M, Hirayama A, Atsumi H, Yatsushiro S, Kuroda K. Velocity and pressure gradients of cerebrospinal fluid assessed with magnetic resonance imaging. *J Neurosurg*. 2013
71. Santini F, Wetzel SG, Bock J, Markl M, Scheffler K. Time-resolved three-dimensional (3d) phase-contrast (pc) balanced steady-state free precession (bssfp). *Magnetic Resonance in Medicine*. 2009;62:966-974
72. Stadlbauer A, Salomonowitz E, Brenneis C, Ungersbock K, van der Riet W, Buchfelder M, Ganslandt O. Magnetic resonance velocity mapping of 3d cerebrospinal fluid flow dynamics in hydrocephalus: Preliminary results. *European radiology*. 2012;22:232-242
73. Harloff A, Strecker C, Reinhard M, Kollum M, Handke M, Olschewski M, Weiller C, Hetzel A. Combined measurement of carotid stiffness and intima-media thickness improves prediction of complex aortic plaques in patients with ischemic stroke. *Stroke*. 2006;37:2708-2712
74. Kurtcuoglu V, Soellinger M, Summers P, Boomsma K, Poulikakos D, Boesiger P, Ventikos Y. Reconstruction of cerebrospinal fluid flow in the third ventricle based on mri data. *Medical Image Computing and Computer-Assisted Intervention - Miccai 2005, Pt 1*. 2005;3749:786-793
75. Gupta S, Soellinger M, Boesiger P, Poulikakos D, Kurtcuoglu V. Three-dimensional computational modeling of subject-specific cerebrospinal fluid flow in the subarachnoid space. *J Biomech Eng*. 2009;131:021010
76. Bertram CD. Evaluation by fluid/structure-interaction spinal-cord simulation of the effects of subarachnoid-space stenosis on an adjacent syrinx. *J Biomech Eng*. 2010;132:-
77. Kurtcuoglu V, Soellinger M, Summers P, Boomsma K, Poulikakos D, Boesiger P, Ventikos Y. Reconstruction of cerebrospinal fluid flow in the third ventricle based on mri data. *Med Image Comput Assist Interv*. 2005;8:786-793
78. Hentschel S, Mardal KA, Lovgren AE, Linge S, Haughton V. Characterization of cyclic csf flow in the foramen magnum and upper cervical spinal canal with mr flow imaging and computational fluid dynamics. *AJNR Am J Neuroradiol*. 2010;31:997-1002
79. Gupta S, Soellinger M, Grzybowski DM, Boesiger P, Biddiscombe J, Poulikakos D, Kurtcuoglu V. Cerebrospinal fluid dynamics in the human cranial subarachnoid space: An overlooked mediator of cerebral disease. I. Computational model. *J R Soc Interface*. 2010;7:1195-1204
80. Rutkowska G, Haughton V, Linge S, Mardal KA. Patient-specific 3d simulation of cyclic csf flow at the craniocervical region. *AJNR Am J Neuroradiol*. 2012;33:1756-1762

81. Carpenter PW, Berkouk K, Lucey AD. Pressure wave propagation in fluid-filled co-axial elastic tubes. Part 2: Mechanisms for the pathogenesis of syringomyelia. *J Biomech Eng.* 2003;125:857-863
82. Bertram CD, Bilston LE, Stoodley MA. Tensile radial stress in the spinal cord related to arachnoiditis or tethering: A numerical model. *Med Biol Eng Comput.* 2008;46:701-707
83. Bertram CD, Brodbelt AR, Stoodley MA. The origins of syringomyelia: Numerical models of fluid/structure interactions in the spinal cord. *J Biomech Eng.* 2005;127:1099-1109
84. Martin BA, Kalata W, Loth F, Royston TJ, Oshinski JN. Syringomyelia hydrodynamics: An in vitro study based on in vivo measurements. *J Biomech Eng.* 2005;127:1110-1120
85. Shaffer N, Martin BA, Loth F. Cerebrospinal fluid hydrodynamics in type I Chiari malformation. *Neurol Res.* 2011;33:247-260
86. Iskandar BJ, Quigley M, Haughton VM. Foramen magnum cerebrospinal fluid flow characteristics in children with Chiari I malformation before and after craniocervical decompression. *J Neurosurg.* 2004;101:169-178
87. Stadlbauer A, Salomonowitz E, Brenneis C, Ungersbock K, van der Riet W, Buchfelder M, Ganslandt O. Magnetic resonance velocity mapping of 3D cerebrospinal fluid flow dynamics in hydrocephalus: Preliminary results. *European Radiology.* 2012;22:232-242
88. Loth F, Yardimci MA, Alperin N. Hydrodynamic modeling of cerebrospinal fluid motion within the spinal cavity. *J Biomech Eng-T Asme.* 2001;123:71-79
89. Gupta S, Soellinger M, Grzybowski DM, Boesiger P, Biddiscombe J, Poulikakos D, Kurtcuoglu V. Cerebrospinal fluid dynamics in the human cranial subarachnoid space: An overlooked mediator of cerebral disease. I. Computational model. *Journal of the Royal Society, Interface / the Royal Society.* 2010;7:1195-1204
90. Rutkowska G, Haughton V, Linge S, Mardal KA. Patient-specific 3D simulation of cyclic CSF flow at the craniocervical region. *AJNR Am J Neuroradiol.* 2012
91. Linge SO, Haughton V, Lovgren AE, Mardal KA, Langtangen HP. CSF flow dynamics at the craniovertebral junction studied with an idealized model of the subarachnoid space and computational flow analysis. *AJNR. American journal of neuroradiology.* 2010;31:185-192
92. Bertram CD. A numerical investigation of waves propagating in the spinal cord and subarachnoid space in the presence of a syrinx. *Journal of Fluids and Structures.* 2009;25:1189-1205
93. Cirovic S. A coaxial tube model of the cerebrospinal fluid pulse propagation in the spinal column. *J Biomech Eng-T Asme.* 2009;131
94. Elliott NS, Lockerby DA, Brodbelt AR. The pathogenesis of syringomyelia: A re-evaluation of the elastic-jump hypothesis. *J Biomech Eng.* 2009;131:044503
95. Cirovic S, Kim M. A one-dimensional model of the spinal cerebrospinal-fluid compartment. *J Biomech Eng.* 2012;134:021005
96. Elliott NS, Lockerby DA, Brodbelt AR. A lumped-parameter model of the cerebrospinal system for investigating arterial-driven flow in posttraumatic syringomyelia. *Med Eng Phys.* 2011;33:874-882
97. Linninger AA, Xenos M, Sweetman B, Ponkshe S, Guo XD, Penn R. A mathematical model of blood, cerebrospinal fluid and brain dynamics. *J Math Biol.* 2009;59:729-759
98. Bilston LE, Fletcher DF, Stoodley MA. Focal spinal arachnoiditis increases subarachnoid space pressure: A computational study. *Clin Biomech (Bristol, Avon).* 2006;21:579-584
99. Carpenter PW, Berkouk K, Lucey AD. Pressure wave propagation in fluid-filled co-axial elastic tubes part 2: Mechanisms for the pathogenesis of syringomyelia. *Journal of Biomechanical Engineering.* 2003;125:857
100. Berkouk K, Carpenter PW, Lucey AD. Pressure wave propagation in fluid-filled co-axial elastic tubes part 1: Basic theory. *Journal of Biomechanical Engineering.* 2003;125:852
101. Cirovic S, Walsh C, Fraser WD. Wave propagation in a system of coaxial tubes filled with incompressible media: A model of pulse transmission in the intracranial arteries. *J Fluid Struct.* 2002;16:1029-1049
102. Martin BA, Loth F. The influence of coughing on cerebrospinal fluid pressure in an in vitro syringomyelia model with spinal subarachnoid space stenosis. *Cerebrospinal fluid research.* 2009;6:17

103. Martin BA, Labuda R, Royston TJ, Oshinski JN, Iskandar B, Loth F. Spinal subarachnoid space pressure measurements in an in vitro spinal stenosis model: Implications on syringomyelia theories. *J Biomech Eng.* 2010;132:111007
104. Botta S, Poulidakos D, Kurtcuoglu V. Phantom model of physiologic intracranial pressure and cerebrospinal fluid dynamics. *IEEE transactions on bio-medical engineering.* 2012
105. Kurtcuoglu V, Soellinger M, Summers P, Boomsma K, Poulidakos D, Boesiger P, Ventikos Y. Computational investigation of subject-specific cerebrospinal fluid flow in the third ventricle and aqueduct of Sylvius. *J Biomech.* 2007;40:1235-1245
106. Kurtcuoglu V, Gupta S, Soellinger M, Grzybowski DM, Boesiger P, Biddiscombe J, Poulidakos D. Cerebrospinal fluid dynamics in the human cranial subarachnoid space: An overlooked mediator of cerebral disease. I. Computational model. *J R Soc Interface.* 2010;7:1195-1204
107. Gupta A, Church D, Barnes D, Hassan AB. Cut to the chase: On the need for genotype-specific soft tissue sarcoma trials. *Ann Oncol.* 2009;20:399-400
108. Johnson KM, Markl M. Improved snr in phase contrast velocimetry with five-point balanced flow encoding. *Magn Reson Med.* 2010;63:349-355
109. Sigmund EE, Suero GA, Hu C, McGorty K, Sodickson DK, Wiggins GC, Helpert JA. High-resolution human cervical spinal cord imaging at 7 t. *NMR Biomed.* 2011
110. Cousins J, Haughton V. Motion of the cerebellar tonsils in the foramen magnum during the cardiac cycle. *Am J Neuroradiol.* 2009;30:1587-1588
111. Schmid Daners M, Knobloch V, Soellinger M, Boesiger P, Seifert B, Guzzella L, Kurtcuoglu V. Age-specific characteristics and coupling of cerebral arterial inflow and cerebrospinal fluid dynamics. *PLoS One.* 2012;7:e37502
112. Brunholzl C, Muller HR. [the effect of head and body position on jugular vein blood flow]. *Vasa.* 1989;18:205-208
113. Rossiti S, Volkmann R. Changes of blood flow velocity indicating mechanical compression of the vertebral arteries during rotation of the head in the normal human measured with transcranial doppler sonography. *Arq Neuropsiquiatr.* 1995;53:26-33
114. Ng I, Lim J, Wong HB. Effects of head posture on cerebral hemodynamics: Its influences on intracranial pressure, cerebral perfusion pressure, and cerebral oxygenation. *Neurosurgery.* 2004;54:593-597; discussion 598
115. Yamada S, Ducker TB, Perot PL. Dynamic changes of cerebrospinal fluid in upright and recumbent shunted experimental animals. *Childs Brain.* 1975;1:187-192
116. Speer MC, Enterline DS, Mehlretter L, Hammock P, Joseph J, Dickerson M, Ellenbogen RG, Milhorat TH, Hauser MA, George TM. Review article: Chiari type I malformation with or without syringomyelia: Prevalence and genetics. *Journal of Genetic Counseling.* 2003;12:297-311
117. Henry-Feugeas MC, Idy-Peretti I, Baledent O, Cornu P, Lejay H, Bittoun J, Schouman-Claeys AE. Cerebrospinal fluid flow waveforms: Mr analysis in chronic adult hydrocephalus. *Investigative radiology.* 2001;36:146-154
118. Cushing H. Studies on the cerebro-spinal fluid : I. Introduction. *The Journal of medical research.* 1914;31:1-19
119. Hall JE, Guyton AC. *Guyton and hall textbook of medical physiology.* Philadelphia, Pa.: Saunders/Elsevier; 2011.
120. Heidari Pahlavian S, Yiallourou T, Tubbs RS, Bunck AC, Loth F, Goodin M, Raisee M, Martin BA. The impact of spinal cord nerve roots and denticulate ligaments on cerebrospinal fluid dynamics in the cervical spine. *PLoS One.* 2014;9:e91888
121. Martin BA, Raymond P, Novy J, Baledent O, Stergiopoulos N. A coupled hydrodynamic model of the cardiovascular and cerebrospinal fluid system. *Am J Physiol Heart Circ Physiol.* 2012;302:H1492-1509
122. Linninger AA, Tsakiris C, Zhu DC, Xenos M, Roycewicz P, Danziger Z, Penn R. Pulsatile cerebrospinal fluid dynamics in the human brain. *IEEE Trans Biomed Eng.* 2005;52:557-565
123. Linninger AA, Xenos M, Zhu DC, Somayaji MR, Kondapalli S, Penn RD. Cerebrospinal fluid flow in the normal and hydrocephalic human brain. *IEEE Trans Biomed Eng.* 2007;54:291-302

124. Helgeland A, Mardal KA, Haughton V, Reif BA. Numerical simulations of the pulsating flow of cerebrospinal fluid flow in the cervical spinal canal of a chiari patient. *Journal of biomechanics*. 2014;47:1082-1090
125. Martin BA, Shaffer N, Lowenkamp M, Loth F, Tew J, Luciano M. Clinical importance of neural tissue deformation in type i chiari malformation. *Proceedings of the American Society of Pediatric Neurosurgeons*. 2013;Abstract
126. Glor FP, Long Q, Hughes AD, Augst AD, Ariff B, Thom SA, Verdonck PR, Xu XY. Reproducibility study of magnetic resonance image-based computational fluid dynamics prediction of carotid bifurcation flow. *Ann Biomed Eng*. 2003;31:142-151
127. Glor FP, Ariff B, Hughes AD, Verdonck PR, Thom SA, Barratt DC, Xu XY. Operator dependence of 3-d ultrasound-based computational fluid dynamics for the carotid bifurcation. *IEEE Trans Med Imaging*. 2005;24:451-456
128. Augst AD, Barratt DC, Hughes AD, Glor FP, Mc GTSA, Xu XY. Accuracy and reproducibility of cfd predicted wall shear stress using 3d ultrasound images. *J Biomech Eng*. 2003;125:218-222
129. Long Q, Ariff B, Zhao SZ, Thom SA, Hughes AD, Xu XY. Reproducibility study of 3d geometrical reconstruction of the human carotid bifurcation from magnetic resonance images. *Magn Reson Med*. 2003;49:665-674
130. Yiallourou TI, Kroger JR, Stergiopulos N, Maintz D, Martin BA, Bunck AC. Comparison of 4d phase-contrast mri flow measurements to computational fluid dynamics simulations of cerebrospinal fluid motion in the cervical spine. *PLoS One*. 2012;7:e52284
131. Martin BA, Kalata W, Shaffer N, Fischer P, Luciano M, Loth F. Hydrodynamic and longitudinal impedance analysis of cerebrospinal fluid dynamics at the craniovertebral junction in type i chiari malformation. *PLoS One*. 2013;8:e75335
132. Urbizu A, Poca MA, Vidal X, Rovira A, Sahuquillo J, Macaya A. Mri-based morphometric analysis of posterior cranial fossa in the diagnosis of chiari malformation type i. *Journal of neuroimaging : official journal of the American Society of Neuroimaging*. 2013
133. Dolar MT, Haughton VM, Iskandar BJ, Quigley M. Effect of craniocervical decompression on peak csf velocities in symptomatic patients with chiari i malformation. *AJNR Am J Neuroradiol*. 2004;25:142-145
134. Williams B. Further thoughts on valvular action of arnold-chiari malformation. *Dev Med Child Neurol*. 1971:105-&
135. Clarke EC, Fletcher DF, Stoodley MA, Bilston LE. Computational fluid dynamics modelling of cerebrospinal fluid pressure in chiari malformation and syringomyelia. *Journal of biomechanics*. 2013;46:1801-1809
136. Sigmund EE, Suero GA, Hu C, McGorty K, Sodickson DK, Wiggins GC, Helpert JA. High-resolution human cervical spinal cord imaging at 7 t. *NMR Biomed*. 2012;25:891-899
137. Hsu Y, Hettiarachchi HD, Zhu DC, Linninger AA. The frequency and magnitude of cerebrospinal fluid pulsations influence intrathecal drug distribution: Key factors for interpatient variability (vol 115, pg 386, 2012). *Anesthesia and Analgesia*. 2012;115:879-879
138. Klingelhofer J, Hajak G, Sander D, Schulz-Varzegi M, Ruther E, Conrad B. Assessment of intracranial hemodynamics in sleep apnea syndrome. *Stroke*. 1992;23:1427-1433
139. Netzer N, Werner P, Jochums I, Lehmann M, Strohl KP. Blood flow of the middle cerebral artery with sleep-disordered breathing: Correlation with obstructive hypopneas. *Stroke*. 1998;29:87-93
140. Schoning M, Walter J, Scheel P. Estimation of cerebral blood flow through color duplex sonography of the carotid and vertebral arteries in healthy adults. *Stroke; a journal of cerebral circulation*. 1994;25:17-22
141. Tominaga S, Strandgaard S, Uemura K, Ito K, Kutsuzawa T. Cerebrovascular co2 reactivity in normotensive and hypertensive man. *Stroke*. 1976;7:507-510
142. Leguy CA, Bosboom EM, Hoeks AP, van de Vosse FN. Model-based assessment of dynamic arterial blood volume flow from ultrasound measurements. *Med Biol Eng Comput*. 2009;47:641-648
143. Kety SS, Schmidt CF. The effects of altered arterial tensions of carbon dioxide and oxygen on cerebral blood flow and cerebral oxygen consumption of normal young men. *J Clin Invest*. 1948;27:484-492

144. Harper AM, Glass HI. Effect of alterations in arterial carbon dioxide tension on blood flow through cerebral cortex at normal and low arterial blood pressures. *J Neurol Neurosurg Ps.* 1965;28:449-&
145. Grubb RL, Jr., Raichle ME, Eichling JO, Ter-Pogossian MM. The effects of changes in paco₂ on cerebral blood volume, blood flow, and vascular mean transit time. *Stroke.* 1974;5:630-639
146. Wang Q, Paulson OB, Lassen NA. Effect of nitric-oxide blockade by n-g-nitro-l-arginine on cerebral blood-flow response to changes in carbon-dioxide tension. *J Cerebr Blood F Met.* 1992;12:947-953
147. Eng C, Lam A, Mayberg T, Mathison T, Lee C. The influence of propofol with and without nitrous-oxide on cerebral blood-flow velocity and co₂ reactivity in man. *Stroke.* 1992;23:456-456
148. Henriksen L. Brain luxury perfusion during cardiopulmonary bypass in humans - a study of the cerebral blood-flow response to changes in co₂, o₂, and blood-pressure. *J Cerebr Blood F Met.* 1986;6:366-378
149. Reivich M. Arterial pco₂ and cerebral hemodynamics. *Am J Physiol.* 1964;206:25-35
150. Wasserman A, Patterson JL. Cerebral vascular response to reduction in arterial carbon dioxide tension. *Journal of Clinical Investigation.* 1961;40:1297-&
151. White JC, Brooks JR, Goldthwait JC, Adams RD. Changes in brain volume and blood content after experimental concussion. *Ann Surg.* 1943;118:619-633
152. Lambertsen CJ, Owen SG, Wendel H, Stroud MW, Lurie AA, Lochner W, Clark GF. Respiratory and cerebral circulatory control during exercise at .21 and 2.0 atmospheres inspired po₂. *Journal of Applied Physiology.* 1959;14:966-982
153. Alexander SC, Cohen PJ, Wollman H, Smith TC, Reivich M, Vandermolen RA. Cerebral carbohydrate metabolism during hypocarbia in man: Studies during nitrous oxide anesthesia. *Anesthesiology.* 1965;26:624-632
154. Pierce EC, Linde HW, Deutsch S, Chase PE, Price HL, Lambertsen CJ, Dripps RD. Cerebral circulation and metabolism during thiopental anesthesia and hyperventilation in man. *Journal of Clinical Investigation.* 1962;41:1664-&
155. James IM, Millar RA, Purves MJ. Observations on extrinsic neural control of cerebral blood flow in baboon. *Circulation Research.* 1969;25:77-&
156. Smith AL, Neufeld GR, Ominsky AJ, Wollman H. Effect of arterial co₂ tension on cerebral blood flow, mean transit time, and vascular volume. *Journal of Applied Physiology.* 1971;31:701-&
157. Raichle ME, Posner JB, Plum F. Cerebral blood flow during and after hyperventilation. *Arch Neurol-Chicago.* 1970;23:394-&
158. Fujishima M, Scheinberg P, Busto R, Reinmuth OM. The relation between cerebral oxygen consumption and cerebral vascular reactivity to carbon dioxide. *Stroke.* 1971;2:251-257
159. Kontos HA. Validity of cerebral arterial blood flow calculations from velocity measurements. *Stroke.* 1989;20:1-3
160. Scala R, Turkington PM, Wanklyn P, Bamford J, Elliott MW. Acceptance, effectiveness and safety of continuous positive airway pressure in acute stroke: A pilot study. *Respir Med.* 2009;103:59-66
161. Schmidt JF, Waldemar G, Vorstrup S, Andersen AR, Gjerris F, Paulson OB. Computerized analysis of cerebral blood flow autoregulation in humans: Validation of a method for pharmacologic studies. *J Cardiovasc Pharmacol.* 1990;15:983-988
162. Guyton AC. *Textbook of medical physiology.* Philadelphia: Saunders; 1991.
163. Stroobant N, Vingerhoets G. Transcranial doppler ultrasonography monitoring of cerebral hemodynamics during performance of cognitive tasks: A review. *Neuropsychol Rev.* 2000;10:213-231
164. Droste DW, Ludemann P, Anders F, Kemeny V, Thomas M, Krauss JK, Ringelstein EB. Middle cerebral artery blood flow velocity, end-tidal pco₂ and blood pressure in patients with obstructive sleep apnea and in healthy subjects during continuous positive airway pressure breathing. *Neurol Res.* 1999;21:737-741
165. Navalesi P, Fanfulla F, Frigerio P, Gregoret G, Nava S. Physiologic evaluation of noninvasive mechanical ventilation delivered with three types of masks in patients with chronic hypercapnic respiratory failure. *Critical Care Medicine.* 2000;28:1785-1790

166. Bakker JP, Neill AM, Campbell AJ. Nasal versus oronasal continuous positive airway pressure masks for obstructive sleep apnea: A pilot investigation of pressure requirement, residual disease, and leak. *Sleep Breath*. 2011
167. Martin BA, Reymond P, Novy J, Baledent O, Stergiopulos N. A coupled hydrodynamic model of the cardiovascular and cerebrospinal fluid system. *American Journal of Physiology - Heart and Circulatory Physiology*. 2012;302:H1492-1509
168. Xie L, Kang H, Xu Q, Chen MJ, Liao Y, Thiyagarajan M, O'Donnell J, Christensen DJ, Nicholson C, Iliff JJ, Takano T, Deane R, Nedergaard M. Sleep drives metabolite clearance from the adult brain. *Science*. 2013;342:373-377
169. Yang L, Kress BT, Weber HJ, Thiyagarajan M, Wang B, Deane R, Benveniste H, Iliff JJ, Nedergaard M. Evaluating glymphatic pathway function utilizing clinically relevant intrathecal infusion of csf tracer. *Journal of translational medicine*. 2013;11:107
170. Elliott NSJ, Bertram CD, Martin BA, Brodbelt AR. Syringomyelia: A review of the biomechanics. *J Fluid Struct*. 2013;40:1-24
171. Miyati T, Mase M, Kasai H, Hara M, Yamada K, Shibamoto Y, Soellinger M, Baltes C, Luechinger R. Noninvasive mri assessment of intracranial compliance in idiopathic normal pressure hydrocephalus. *J Magn Reson Imaging*. 2007;26:274-278
172. Stoquart-ElSankari S, Baledent O, Gondry-Jouet C, Makki M, Godefroy O, Meyer ME. Aging effects on cerebral blood and cerebrospinal fluid flows. *J Cereb Blood Flow Metab*. 2007;27:1563-1572
173. Park EH, Dombrowski S, Luciano M, Zurakowski D, Madsen JR. Alterations of pulsation absorber characteristics in experimental hydrocephalus. *Journal of neurosurgery. Pediatrics*. 2010;6:159-170
174. Greitz D, Wirestam R, Franck A, Nordell B, Thomsen C, Stahlberg F. Pulsatile brain movement and associated hydrodynamics studied by magnetic resonance phase imaging. The monro-kellie doctrine revisited. *Neuroradiology*. 1992;34:370-380
175. Alperin N, Vikingstad EM, Gomez-Anson B, Levin DN. Hemodynamically independent analysis of cerebrospinal fluid and brain motion observed with dynamic phase contrast mri. *Magnetic resonance in medicine : official journal of the Society of Magnetic Resonance in Medicine / Society of Magnetic Resonance in Medicine*. 1996;35:741-754
176. Stoquart-ElSankari S, Lehmann P, Villette A, Czosnyka M, Meyer ME, Deramond H, Baledent O. A phase-contrast mri study of physiologic cerebral venous flow. *J Cereb Blood Flow Metab*. 2009;29:1208-1215
177. ElSankari S, Baledent O, van Pesch V, Sindic C, de Broqueville Q, Duprez T. Concomitant analysis of arterial, venous, and csf flows using phase-contrast mri: A quantitative comparison between ms patients and healthy controls. *J Cereb Blood Flow Metab*. 2013;33:1314-1321
178. Dabrowski W. Changes in intra-abdominal pressure and central venous and brain venous blood pressure in patients during extracorporeal circulation. *Med Sci Monit*. 2007;13:CR548-554
179. Bloomfield GL, Ridings PC, Blocher CR, Marmarou A, Sugerman HJ. A proposed relationship between increased intra-abdominal, intrathoracic, and intracranial pressure. *Crit Care Med*. 1997;25:496-503
180. Lockey P, Poots G, Williams B. Theoretical aspects of the attenuation of pressure pulses within cerebrospinal-fluid pathways. *Med Biol Eng*. 1975;13:861-869
181. Mehta NR, Jones L, Kraut MA, Melhem ER. Physiologic variations in dural venous sinus flow on phase-contrast mr imaging. *AJR Am J Roentgenol*. 2000;175:221-225
182. Gisolf J, van Lieshout JJ, van Heusden K, Pott F, Stok WJ, Karemaker JM. Human cerebral venous outflow pathway depends on posture and central venous pressure. *J Physiol*. 2004;560:317-327
183. Chernobelsky A, Shubayev O, Comeau CR, Wolff SD. Baseline correction of phase contrast images improves quantification of blood flow in the great vessels. *J Cardiovasc Magn Reson*. 2007;9:681-685
184. Schmid Daners M, Knobloch V, Soellinger M, Boesiger P, Seifert B, Guzzella L, Kurtcuoglu V. Age-specific characteristics and coupling of cerebral arterial inflow and cerebrospinal fluid dynamics. *Plos One*. 2012;7
185. Kolbitsch C, Lorenz IH, Hormann C, Schocke M, Kremser C, Zschiegner F, Felber S, Benzer A. The impact of increased mean airway pressure on contrast-enhanced mri measurement of regional cerebral blood flow (rcbf), regional cerebral blood volume (rcbv), regional mean transit time (rmitt), and regional cerebrovascular resistance (rcvr) in human volunteers. *Hum Brain Mapp*. 2000;11:214-222

186. Chen JJ, Pike GB. Mri measurement of the bold-specific flow-volume relationship during hypercapnia and hypocapnia in humans. *Neuroimage*. 2010;53:383-391
187. Hayen A, Herigstad M, Kelly M, Okell TW, Murphy K, Wise RG, Pattinson KT. The effects of altered intrathoracic pressure on resting cerebral blood flow and its response to visual stimulation. *Neuroimage*. 2012;66C:479-488
188. Kolbitsch C, Lorenz IH, Hormann C, Schocke MF, Kremser C, Moser PL, Pfeiffer KP, Benzer A. The impact of hypercapnia on systolic cerebrospinal fluid peak velocity in the aqueduct of sylvius. *Anesth Analg*. 2002;95:1049-1051, table of contents
189. Luce JM, Huseby JS, Kirk W, Butler J. Mechanism by which positive end-expiratory pressure increases cerebrospinal fluid pressure in dogs. *J Appl Physiol Respir Environ Exerc Physiol*. 1982;52:231-235
190. Sievers B, Addo M, Kirchberg S, Bakan A, John-Puthenveetil B, Franken U, Trappe HJ. Impact of the ecg gating method on ventricular volumes and ejection fractions assessed by cardiovascular magnetic resonance imaging. *J Cardiovasc Magn Reson*. 2005;7:441-446
191. Knobloch V, Binter C, Kurtcuoglu V, Kozerke S. Arterial, venous, and cerebrospinal fluid flow: Simultaneous assessment with bayesian multipoint velocity-encoded mr imaging. *Radiology*. 2014;270:566-573
192. Levy LM, Di Chiro G. Mr phase imaging and cerebrospinal fluid flow in the head and spine. *Neuroradiology*. 1990;32:399-406
193. Cousins J, Houghton V. Motion of the cerebellar tonsils in the foramen magnum during the cardiac cycle. *AJNR Am J Neuroradiol*. 2009;30:1587-1588
194. Alleyne CH, Jr., Cawley CM, Barrow DL, Bonner GD. Microsurgical anatomy of the dorsal cervical nerve roots and the cervical dorsal root ganglion/ventral root complexes. *Surg Neurol*. 1998;50:213-218

Curriculum Vitae

THIRESIA I.GIALLOUROU

Date of birth: 1989, February 3rd

theresia.yiallourou@gmail.com

Languages: Greek, fluent English (oral and written), competent French

EDUCATION

- **Doctoral studentship (September 2010-August 2014)**

Ph. D Thesis: " Subject-Specific computational fluid dynamics modelling and measurement of cerebrospinal fluid motion in the cervical spine"

Laboratory of Hemodynamics and Cardiovascular Technology, Swiss Federal Institute of Technology (Advisor: Prof. Nikolaos Stergiopoulos, Co-Advisor: Dr. Bryn A. Martin)

- **Bachelor of Science in Mechanical and Manufacturing Engineering (2006-2010)**

University of Cyprus (UCY), Nicosia, Cyprus (Class Valedictorian, GPA: 8.81/10 Excellent)

RESEARCH POST

Visiting research student (September 2009), Swiss Federal Institute of Technology (ETH Zurich), Laboratory of Thermodynamics in Emerging Technologies, Switzerland

WORK EXPERIENCE

Internship, Department of the Strategic Planning, Motor Oil (Hellas), Athens, Greece (June-August 2008)

PEER REVIEWED PUBLICATIONS

- **Yiallourou (Giallourou) TI**, et al., Quantitative comparison of 4D phase-contrast MRI flow measurements to 3D computational fluid dynamics simulations of the cerebrospinal fluid movement in the cervical spine in healthy subjects and Chiari I malformation patients. *PLoS One*. 2012;7(12):e52284. doi: 10.1371/journal.pone.0052284.
- **Yiallourou (Giallourou) TI**, et al., The effect of continuous positive airway pressure on total cerebral blood flow in healthy volunteers. *Sleep Breathing*. 17(1):289-96. doi: 10.1007/s11325-012-0688.
- **Yiallourou (Giallourou) TI**, et al., Inter-operator dependence of subject specific CFD modeling of cerebrospinal fluid dynamics at the craniocervical junction (*under review*)
- **Yiallourou (Giallourou) TI** et al., Continuous positive airway pressure alters cranial blood flow and cerebrospinal fluid dynamics at the craniovertebral junction (*under review*).
- Pahlavian SH, **Yiallourou (Giallourou) TI** et al., The Impact of spinal cord nerve roots and denticulate ligaments on cerebrospinal fluid dynamics in the cervical spine *PLoS One*, vol. 9, p. e91888, 2014.).
- Pahlavian SH, Bunck AC, Tubbs RS, **Yiallourou (Giallourou) TI** et al., Hydrodynamic characterization of cervical cerebrospinal fluid motion by 4D phase-contrast MRI and comparison to anatomically detailed 3D computational fluid dynamics simulation(*under review*).
- Heinzer R, Petitpierre NJ, **Yiallourou (Giallourou) TI** et al., Oscillating positive airway pressure (O-PAP) compared to CPAP in obstructive sleep apnea patients: a pilot study (*under review*).

CONFERENCES

- World Biomechanics Conference 2014, John B. Hynes Veterans Memorial Convention Center (Boston, USA, 6-11/07, 2014)
- 2nd CSF Hydrodynamics symposium, The Feinstein Institute for Medical Research, (NY, USA, 24-25/06, 2013)
- ASME Summer Bioengineering Conference (Fajardo, Puerto Rico, 20-23/06, 2012)
- 10th International Workshop on Biomedical Engineering ,Co-Chaired session, (Kos, Greece, 5-7/10, 2011)
- 1st CSF Hydrodynamics Symposium, (ETH Zurich, Switzerland, 8-9/07, 2011)
- ASME Summer Bioengineering Conference, (Farmington, PA, 22-25/06, 2011)
- Workshop Nonlinear Elliptic PDEs, Department of Mathematics, (ULB, Brussels, Belgium, 2-4/09, 2009)

HONORS, AWARDS & SCHOLARSHIPS

- International Novartis Biotechnology Leadership Camp (August 2013)
- Highest academic ranking Prize during the four years of B.S. studies (June 2010)
- Cyprus State Scholarship Foundation, Highest grade of admission at Department of Mechanical and Manufacturing Engineering, UCY (maintained 2006-2010)
- CASP Fulbright Scholarship, Johns Hopkins University (Baltimore, MD, USA) (June-August 2009)
- Cyprus Mathematical Society, Honorary Diploma , District Mathematics Competition (June 2006)
- Cyprus Biological Society, Honorary Diploma, Cyprus Biology Olympiad (June 2006)
- Bank of Cyprus Prize, Class Valedictorian among the graduating high school class (June 2006)